Study of the earthquake source process and seismic hazards

Cédric Twardzik

Worcester College

Department of Earth Sciences

University of Oxford

Thesis submitted in support of an application for leave to supplicate
for the degree of

Doctor of Philosophy

Hilary 2014

Supervisor: Prof. Shamita Das

Study of the earthquake source process and seismic hazards

Cedric Twardzik

Department of Earth Sciences and Worcester College

University of Oxford

Hilary 2014

Abstract

To obtain the rupture history of the Parkfield, California, earthquake, we perform 12 kinematic inversions using elliptical sub-faults. The preferred model has a seismic moment of 1.21×10^{18} Nm, distributed on two distinct ellipses. The average rupture speed is $\sim$2.7 km/s. The good spatial agreement with previous large earthquakes and aftershocks in the region, suggests the presence of permanent asperities that break during large earthquakes. We investigate our inversion method with several tests. We demonstrate its capability to retrieve the rupture process. We show that the convergence of the inversion is controlled by the space-time location of the rupture front. Additional inversions show that our procedure is not highly influenced by high-frequency signal, while we observe high sensitivity to the waveforms duration. After considering kinematic inversion, we present a full dynamic inversion for the Parkfield earthquake using elliptical sub-faults. The best fitting model has a seismic moment of 1.18×10^{18} Nm, distributed on one ellipse. The rupture speed is $\sim$2.8 km/s. Inside the parameter-space, the models are distributed according the rupture speed and final seismic moment, defin-

ing a optimal region where models fit correctly the data. Furthermore, to make the preferred kinematic model both dynamically correct while fitting the data, we show it is necessary to connect the two ellipses. This is done by adopting a new approach that uses b-spline curves. Finally, we relocate earthquakes in the vicinity of the Darfield, New-Zealand earthquake. 40 years prior to the earthquake, where there is the possibility of earthquake migration towards its epicentral region. Once it triggers the 2010-2011 earthquake sequence, we observe earthquakes migrating inside regions of stress increase. We also observe a stress increase on a large seismic gap of the Alpine Fault, as well as on some portions of the Canterbury Plains that remain today seismically quiet.

Study of the earthquake source process and seismic hazards

Cedric Twardzik

Department of Earth Sciences and Worcester College

University of Oxford

Hilary 2014

Extended abstract

We study two problems related to seismic source seismology. Firstly, kinematic and dynamic inversion of the 2004 Parkfield earthquake in California and secondly, the migration of seismicity following the 2010 Darfield earthquake in New Zealand.

We explore a recently developed method for carrying out kinematic inversions. It is based on an elliptical sub-fault approximation, where the slip history is modelled using a small set of elliptical patches. We use it to invert near-field strong ground motion to obtain the rupture history of the 2004 September 28, $M_w6.0$, Parkfield, California, earthquake. The dataset consists of 10 digital 3-component displacement seismograms. We carry out 12 kinematic inversions using different *a-priori* conditions in order to assess the variability of plausible models. We then select a preferred model based on external criteria that are independent of the inversion procedure. The preferred rupture model has a final seismic moment of 1.21×10^{18} Nm, distributed on two distinct ellipses. The average rupture speed is $\sim$2.7 km/s. This model shows a good agreement with the location of large earthquakes ($M_w > 3$) that have occurred prior to the 2004 Parkfield earthquake, surrounding the two slip patches. Similar behaviour is also observed for the aftershocks. It therefore

suggests the presence of permanent asperities that break during large earthquakes.

We subjected our kinematic inversion method to a series of tests. Using artificially generated data, the capacity of the inversion procedure to retrieve the input rupture history of an artificially created earthquake was tested. In a simple case, the inversion retrieves the input rupture model almost perfectly, the only variation being due to the non-uniqueness of kinematic inversions. For a more complicated rupture process, the inversion only retrieves a low-frequency filtered version of the input slip distribution. The behaviour of the Neighbourhood Algorithm (NA) in its search for the optimal solution was also examined. We observed that the space-time location of the rupture front is the main criterion that drives the convergence, the amplitude of slip being only a secondary criterion important mostly at the end of the inversion. We have also investigated how the data processing affects the results of the kinematic inversion by performing another set of inversions, which differ from the initial kinematic inversions of Twardzik et al. (2012) only in the way the data is processed. We performed one inversion using a different frequency band (0.16-0.50 Hz instead of 0.16-1.00 Hz). It shows that the inversion is not very sensitive to high-frequency signals, since we obtain a similar rupture process in the two frequency band. A similar conclusion is reached when we perform an inversion in which velocity records are inverted instead of displacement records. Finally, we looked at the influence of the length of the seismograms that are used to calculate the misfit. We see that the progressive addition of signals from P, S and Rayleigh waves greatly affects the result because it relates to the quantity of information about the rupture process that is given to the algorithm.

We present a full dynamic inversion for the rupture process of the September 28, 2004, $M_w6.0$, Parkfield, California, earthquake, using an elliptical sub-fault approximation. By carrying out a full dynamic inversion, we attempt to obtain at the simultaneously the geometry of the rupture area and the stress and frictional properties of the fault. In the elliptical sub-fault approximation, the rupture is restricted

to occur within the elliptical patches. Inside of each patch, the background stress (T_e) is assumed to be uniform and the upper yield stress (T_u) follows an elliptical distribution, with maximum rupture resistance at the centre of the ellipse. The dataset consists of 10 digital 3-component displacement seismograms. The lowest misfit model reached by the inversion is composed of one ellipse elongated along strike and extending from the hypocenter to almost the north-western end of the fault plane. The final seismic moment is 1.18×10^{18} Nm and the rupture occurs at an approximately constant rupture speed of 2.80 km/s, compatible with a value for κ (ratio of the available energy to energy release rate) of 1.40. In addition to the inversion, we explore the dynamic parameter-space using a Monte-Carlo optimisation method. For this purpose, the geometry of the rupture area is fixed at that obtained from the dynamic inversion. We show that the models distribution in the parameter-space is essentially controlled by the average rupture speed and the final seismic moment. We show that the structure of the parameter-space relative to the rupture speed and the seismic moment defines a very narrow region within which the data are well fitted. It is inside this region that we find models that have an average rupture speed and final seismic moment that reproduce the strong ground motion observed. We then use the fixed-geometry approach to investigate the transition between kinematic models and dynamic models. The geometry of the rupture area is defined from the rupture model obtained by kinematic inversion and then the stress and friction conditions are obtained from a dynamic inversion. In particular, we focus on one kinematic inversion which led to a slip distribution with 2 distinct asperities, requiring a jump of the rupture process. We show first that we fail to find a set of dynamic parameters that reproduces this kind of rupture model while fitting the data at the same time, unless there is a connection between the two asperities. To build the connection between the two distinct ellipses, we developed a new approach that uses b-spline curves in order to define the rupture area. Once there is the connection, it becomes possible to construct a dynamic rupture model

that has a rupture geometry similar to the one obtained by kinematic inversion, while fitting the observed near-field ground motion well.

By using P-wave arrival-time data supplied by the International Seismological Centre (ISC), we attempt a relocation of the earthquakes in the vicinity of the September 3, 2010, $M_w7.1$, Darfield, New-Zealand earthquake, using the method of Joint Hypocenter Determination (JHD). Even after relocation, we observe no significant seismic activity inside the Canterbury Plains, a region that surrounds the epicentral area of the Darfield earthquake. However, during the 40 years preceding that earthquake, we observe a hint of migration towards that region. The P- and T-axis of the large earthquakes between January 1976 and September 2010 suggests that the whole region could have experienced a long-term stress transfer from the Alpine Fault to the plate interior, although the signal is very weak. After the September 2010 Darfield earthquake, we observe a clear eastward progression of the seismic activity, essentially inside a region of positive static stress changes (i.e. brought closer to failure). This causes the occurrence of the February 21, 2011, $M_w6.3$, Christchurch earthquake. After that earthquake, the direction of the migration is slightly modified so that, after being trapped nearby the epicentral region of the Christchurch earthquake, the seismic activity moves in the north-east direction, again in agreement with region of positive static stress changes caused by the occurrence of the Christchurch earthquake. The Alpine Fault, as well as some portions of the Canterbury Plains, remain seismically quiet at present, but static stress changes calculations show that this sequence has brought them closer to failure.

Acknowledgements

It is obvious of the essence of these acknowledgements that I start by thanking by Shamita Das. She taught me a lot about earthquakes, which made this thesis an extremely rewarding experience! With her guidance throughout the three and a half years of this thesis, I hope that I became a better scientist than I was when I started. And, despite all of the hard times, I have really enjoyed and benefited greatly from working with her. I also owe much to Raul Madariaga. Although he was not a supervisor on paper, he acted very much like one. Without his help and support, most of the work of this thesis would not have been possible. It was a real pleasure to work with him! I also would like to thank Heiner Igel and Greta Kueppers, leader and project manager of the QUEST project. It has been delightful to be part of this project through which I met a lot of very interesting people, who are unfortunately too numerous to list here. Thanks also to Susana Custodio and Sandy Steacy who have helped me with some of the work that was carried out during this thesis. During my DPhil., I have spent my time between Oxford and Paris and so there are many people I must thank on each side of the Channel. I will start with Oxford. I would like first of all to thank the various members of seismolab, Tom, David, Andrew and Chao, with whom, not only I had engaging scientific discussions, but also had a lot of enjoyable time outside the Department. Thanks also to all of my office mates who made the life in the office way more fun! Thank you to all the people in my year with whom I have shared a lot of good time in and outside the Department. Special thanks for Teresa! Your figure on the front cover of the Proceeding of the Royal Society made me realise that science could also become a masterpiece sometimes! (And I'm

not even talking about your poster that made me cry every time I walked down the RCR). Thanks also to Owen who in addition to having me as an office-mate, also had me as a house-mate. Unfortunately for you, now that I have left, there will be no more gin and tonic at 2 am. Thanks to Dan for the inspirational tea breaks in the afternoon, although I will always be disappointed that you chose to get your haircut in S.F. instead of getting a taste of the culture of the city. Thank also to Jie who pulled a muscle while playing squash just so that I could carry her back to town. I also would like to thank the French Mafia of this Department. All of whom have made sure that there was always a french enclave around here for the times when I felt home-sick. Special mention for Michael who has been a very good friend here and still is, even after the English post lost his wedding invitation. I also spent a lot of time on the tennis courts of the Oxford City Tennis Club, so it would be unfair not to thank all the people I met there, especially after all the hours I spent playing. Thanks to all of you, I'm really convinced that you made me become a better player. Thank you especially to Mike and Daan who in addition of being excellent players are also very good friends. On the other side of the Channel, at ENS, thank you to Aurelien, Emilie and Olga with whom I shared an office during my many visits. I would thank especially Aurelien who introduced me to Max Wheeler! I am really grateful to you! I also thank all the crew at ENS who made my stays each time more enjoyable. I must also thank my ex-TAO fellows but nonetheless friends! Thank you Kristel, Adrien, Pierre, Nicolas, Sebastien and Celestine! This has always been a great pleasure to see you each time I returned to France. "Chaque fois, de vous voir, j'en ressentais le beusoin...". Thank you as well to Nicolas Bes, Christelle Bourjot, Bojan Dimitrijevic, Loic Lanneau and Alexandre Pichot, my longtime friends and, I am sure, my friends for many more years! I would also like to thank my parents and my brother Jeremy and sister Marine. I certainly do not tell you enough, but thank you for your support and love. I am and I would be eternally grateful. Finally, I have one last person to thank, a person who has so many nicknames that they are

too numerous to list here, save for the most recent one: "my wife". Thank you for all Florence, I love you.

http://bit.ly/1gUeBVT

“Je suis plus jeune que toi” dit le petit Julien âgé de cinq ans à son grand-père.

Et le grand-père de répondre:

“Oh, moi aussi je suis jeune, mais depuis plus longtemps que toi”.

Jacques Salomé

Contents

List of Figures

iv

List of Tables

Chapter 1

Introduction

The study of earthquakes aims to address two important problems. One is to understand what processes are occurring during the actual rupture of a fault, such as the nucleation, propagation and arrest of the rupture. This branch of seismology is referred to as the study of source process. Another problem is to further understand where and when earthquakes occur. Although some argue that prediction of earthquakes is an impossible goal, the study of this aspect of seismology should at least lead to some improvement in how prepared one can be for the occurrence of an earthquake. In this thesis, these two different aspects will be discussed, with more emphasise given to the study of the earthquake source processes.

The history of modern seismology goes back to Michell (1759). For the first time, using evidences collected following the 1755 Lisbon, Portugal, earthquake, earthquakes were understood as the result of "the transit of elastic compression, or of a succession of these, in parallel or in intersecting lines, through the solid substance and surface of the disturbed country". The first attempt to estimate the wave speed was also made, and evaluated to be about 20 miles per minute (i.e. 0.5 km/s). The hypotheses about the origin of seismic waves were later refined by Mallet (1848). While Michell (1759) thought that the impulse for earthquake shocks were originating under the bed of the ocean, Mallet (1848) concluded that "earthquake shocks often come from profound depths". With the help of his son, he also later produced one of the first maps of world earthquake occurrence (Mallet & Mallet 1858; Figure 1.1).
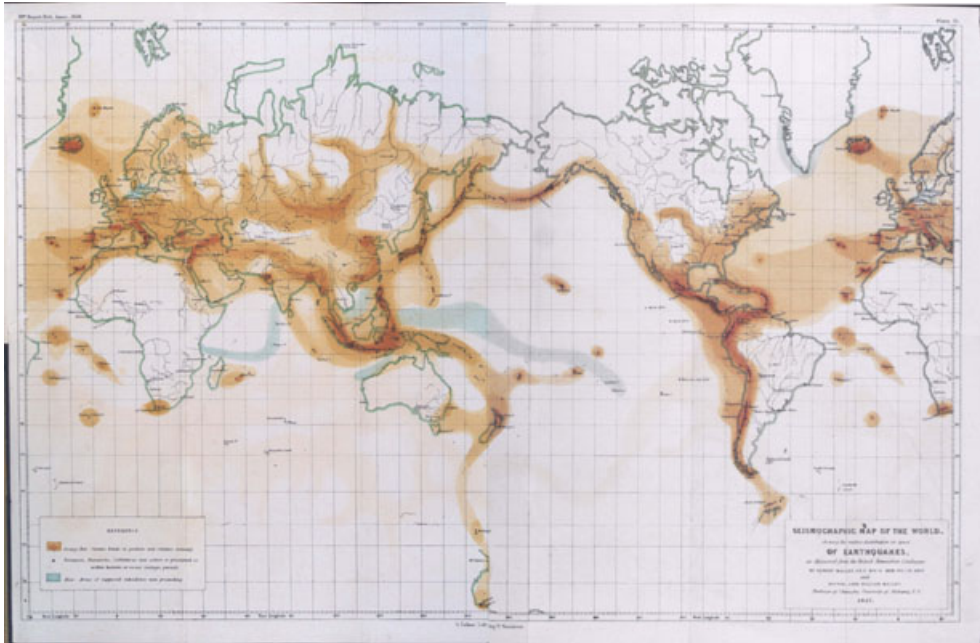
Figure 1.1: Map of world seismicity by Mallet & Mallet (1858). The brown colours show the seriousness of the earthquake with dark brown for frequent and violent earthquakes. Blue colour refers to area of subsidence.

About 50 years later Reid (1910) was able to provide some answers to improve understanding of earthquake source processes with the introduction of the theory of elastic rebound. He described the earthquake source as the result of "external forces [that] must have produced an elastic strain in the region about the fault line, and the stress thus induced were the forces which caused the sudden displacements, or elastic rebounds, when the rupture occurred". He also attempted to make the first estimations of the energy released during earthquakes. At a similar time, in the late 1880s and early 1900s, improvements in seismic instruments recording the ground motion were made, notably with the creation of the horizontal pendulum seismograph by John Milne. This new influx of observations led to the development of models for the seismic source in order to describe observations. One of the first attempts was made by Nakano (1923) who introduced the concept of a conical point-source to describe the first motion pattern observed after an earthquake. In the 1950s, it was finally established that most earthquakes had a double couple source mechanism (i.e. a quadrupole of four sources without resultant force nor moment).

Meanwhile, some progress was also made from a purely observational point of view. For instance, Benioff (1955) estimated the rupture speed from seismic observation. Further advancements on the conceptual models of the earthquake source and the growth of the available waveform dataset, led to the idea that it was possible to get a more complete view of the source processes using seismic waveforms. Thus, Aki (1972) stated that "since the slip motion is a function of time and two space coordinates a complete inversion is extremely difficult. The only practical inversion method is to describe the kinematics of rupture growth in a fault plane using a small number of parameters, and then determine those parameters from the seismograms", opening the way to the development of finite-source inversion.

The Oxford dictionary defines kinematic as "the branch of mechanics concerned with the motion of objects without reference to the forces which cause the motion". In order to study the kinematic source process of an earthquake from ground motion records, it first requires the development of appropriate methods for forward modelling. As mentioned earlier, Nakano (1923) started that process with the introduction of the point-source description of an earthquake. Later, Ben-Menahem (1961, 1962) improved this model and described the radiation of surface and body waves emitted from a moving source. It was also shown that body waves could be used to infer the fault length and the rupture speed. The development of modern kinematic source model then further benefited from the work of Burridge & Knopoff (1964), Haskell (1964) and Kostrov (1964). Burridge & Knopoff (1964) established the relation between a double-couple and slip on a fault. Haskell (1964) introduced the dislocation model that describes the radiation from a rectangular finite-fault that ruptures at a pre-assigned constant rupture speed. Kostrov (1964) introduced the self-similar circular crack that propagates at a pre-assigned constant rupture speed. The relevance of those studies was soon acknowledged by Aki (1968) who, by using near-field records of the 1966 Parkfield, California, earthquake, validated that the seismic source was a propagating dislocation.

Once reliable methods to perform the kinematic forward modelling were available, it became conceivable to invert for the rupture process of an earthquake from seismic waveforms. Trifunac (1974) was the first to perform a finite fault inversion for the rupture process of 1971 San Fernando, California, earthquake using five strong-motion accelerograms. The inversion was based on a trial-and-error methodology and it already acknowledged that the inverse problem solution is non-unique. Thereafter, more elaborate inversion methods started to be used. Thus, Olson & Aspel (1982) performed the first linear inversion (i.e. the rupture speed is fixed and constant) for the rupture process of the 1979 Imperial Valley earthquake. They used both a least-squares method and a constrained least-squares method, recognising that constraints are necessary to stabilise the inverse problem solution. This earthquake was also for the first time studied by different groups using kinematic inversion. Hartzell & Heaton (1983) inferred the rupture history from both strong-motion and teleseismic data using a least-squares inversion and Archuleta (1984) inverted the near-source strong-motion data using a trial-and-error method. All these studies on the same earthquake thus provided a clear illustration of the non-uniqueness associated with kinematic inversions. A few years later, Yoshida (1986) performed the first non-linear inversion (i.e. the rupture speed is treated as an unknown), applying methods to an artificial dataset in order to assess the ability of the inversion procedure to reliably determine a rupture process with variable rupture speed. A similar approach was used by Fukuyama & Irikura (1986) to investigate the rupture process of the 1983 Akita-Oki earthquake. In the meantime, it was recognised by Menke (1985) that "the exact slip rate function cannot be recovered by the data. At best, only a filtered version of it can be reconstructed. This filter is not completely determined by the mathematics of the problem, and can therefore be optimised to yield images of the slip rate that have good resolution". It was also stressed by Jackson & Matsu'ura (1985) that "to solve nonunique inverse problems, we must supply some form of prior information". To better understand the

behaviour of kinematic inversions and assess the reliability of the inverse problem solution, it became necessary to investigate the non-uniqueness of kinematic inversion. This led to the emergence of studies such as Das & Kostrov (1990, 1994), who investigated the non-uniqueness and reliability of the kinematic inversion. They addressed this by examining the effects of physically based constraints on the inverse problem solution, and advocated that they were necessary to ensure a physically reliable solution. Henry et al. (2000), in their study of the 1998 Antarctic Plate earthquake, "make the explicit assumption that physically realistic solutions will be smooth in space and time". Following the same idea, Vallée & Bouchon (2004) introduced the concept of an elliptical sub-fault approximation to invert for the rupture process of an earthquake. One of the advantages of this method is that it uses a intrinsically smooth solution. It fits well with the suggestion of Aki (1972) who said that a "practical inversion method is to describe the kinematics of rupture growth in a fault plane using a small number of parameters". This method was applied to the 1999 Izmit, Turkey, earthquake and the 1995, Jalisco, Mexico, earthquake both using body P- and SH-waves from teleseismic distance. The same approach was then used by Peyrat et al. (2010); Di Carli et al. (2010) and Ruiz & Madariaga (2013) for the study of the 2007 Tocopilla, Chile, earthquake, the 2000 Tottori, Japan, earthquake and the 2008 Iwate, Japan, earthquake.

In this thesis, we also consider the use of elliptical sub-faults for the inversion of the rupture source process. Thus, in Chapter 1, we use the method of elliptical sub-fault to perform a series of inversions for the rupture process of the September 28, 2004, $M_w6.0$, Parkfield, California earthquake from near-field data. The fact that several inversions are carried out allows us to study the variability of the inversion in order to extract the robust features and obtain a reliable picture of the rupture process. Reliability of the results will also be determined using criteria independent of the inversion, especially the seismicity preceding the Parkfield earthquake as well as its aftershocks. In Chapter 2, we carry out a series of synthetic tests to examine

the performance of our method in finding the robust features of an earthquake. We show that the use of the elliptical sub-fault approximation acts as a low-pass filter, integrating all heterogeneities into one or more ellipses. We also explore the behaviour of the inversion algorithm using the neighbourhood algorithm, which is a direct search method in a multidimensional parameter space in order to find optimal solutions of non-linear inverse problems, and show that the search focuses very quickly towards a model that fits the phase of the waveform, the amplitude being a more local convergence criterion. Finally, we consider the influence of the time-window used for the seismograms during the inversion. We see that because it reflects the content of information given to the search algorithm, it has a non-negligible influence.

Having consider kinematic inversions, we also consider in this thesis the problem of dynamic inversion. The Oxford dictionary defines dynamic as "relating to forces producing motion". To understand the dynamic rupture propagation, it requires knowledge of how a propagating crack results from the forces. Early attempts in this field were made by Griffith (1921) who introduced a failure criterion to describe the propagation of a crack. The idea behind it is that a rupture can only occur when the energy is sufficient to create new surfaces within the elastic medium. Based on this physical description of a crack, Kostrov (1966) developed a theoretical framework for the dynamics of a crack propagating with no pre-assigned rupture speed, the latter being determined from the use of a failure criterion. Improved understanding of the friction on the fault was then made by Ida (1972) and Dietriech (1978), their works being still widely used today for earthquake dynamic modelling. Madariaga (1976) and Das & Aki (1977a,b) significantly contributed to the improvement of numerical scheme to investigate the dynamic propagation of a crack using Finite-Difference (FD) and Boundary Integral Method (BIE), respectively. Both were successfully applied to the study of earthquake source (e.g. the study of the 1992 Landers earthquake by Peyrat et al. (2001) using FD and Aochi & Fukuyama (2002) using

BIE). The first appearance of dynamic inversion was in the work by Quin (1990). They used a trial-and-error approach to infer stress conditions on the fault prior to the 1979 Imperial Valley, California, earthquake and used this to produce a dynamic rupture model compatible with the kinematic rupture model of Archuleta (1984). Later, Fukuyama & Mikumo (1993) developed a joint kinematic/dynamic inversion for the rupture process of the 1990 Izu-Oshima, Japan, earthquake. The method consists in of a kinematic inversion where the source-time functions are adjusted at each step by considering a dynamic modelling of the rupture using the prior results from the kinematic inversion. However, the adjustment of the stresses conditions on the fault for the dynamic modelling was still carried out by a trial-and-error approach. Peyrat & Olsen (2004) were the first to develop a non-linear dynamic inversion for the 2000 Tottori earthquake where the dynamic parameters are treated as unknowns. However, the use of a checker-board discretization scheme introduced a large number of unknowns in the inversion as well as some mathematical issues caused by the stress discontinuities across each element of the checker-board. Following the same approach of Vallée & Bouchon (2004) for kinematic inversion, Di Carli et al. (2010) solved those issues by introducing the elliptical sub-fault approximation in dynamic inversion. Recently, Ruiz & Madariaga (2011) and Ruiz & Madariaga (2013) combined the inversion with a Monte-Carlo exploration to investigate the uncertainties and the trade-off existing between the different dynamic parameters.

In Chapter 3, we further develop these concepts. We perform a dynamic inversion for the rupture process of the 2004 Parkfield earthquake. Because the dynamic rupture is intrinsically a non-unique problem, we explore the parameter space using a Monte Carlo method to investigate the uncertainties associated with the inversion. The goal of the exploration is to understand the ways in which the different rupture models fit within the parameter-space. To do that, the different models are analysed by means of two average quantities that describe the rupture process; the average

speed of the rupture and the final seismic moment. We also attempt to convert the preferred model obtained by kinematic inversion into a dynamic rupture model. We do this in order to test that the rupture model obtained by kinematic inversion can be reproduced by a dynamic inversion, thus proving that the kinematic rupture model is dynamically correct. We also introduce a new approach to describe the rupture zone during the inversion using b-spline curves.

As mentioned in the first paragraph, seismology also aims to understand when and where earthquakes occur in order to assess seismic hazards. There are two ways to assess it within a certain region. One is the study of the seismic catalogues. For instance, Fedotov (1965); Mogi (1969) and Sykes (1971) have identified seismic gaps in subduction zones from the study of historical seismicity. Their results enabled them to relate seismic gaps to potential areas for earthquake occurrence. Another is to understand the stress and its relationship with the earthquake occurrence. Smith & Van De Lindt (1969) were one of the first to demonstrate that earthquakes cause strain adjustments and it was later shown that those adjustments have an effect of the location of the seismicity following a major earthquake (e.g. Yamashina (1978) and Das & Scholz (1981)). The review of Harris (1998) on that later topic shows how widely this is used. However, a recent study of Delescluse et al. (2012) have shown that this effect not only occurs at short-term, typically at the scale of the period of aftershocks occurrence, but it also occurs at a very long time scale.

In Chapter 4, a study of the seismicity around the Canterbury Plains, New Zealand is carried out. It is in this area that the $M_w 7.0$ Darfield earthquake of September 3rd, 2010 and the $M_w 6.2$ Christchurch earthquake of February 22nd, 2011 occurred. We also calculate the static stress changes associated with the occurrence of both earthquakes and the influences on the behaviour of the seismicity. We end by investigating the impact of this seismic sequence on the Alpine Fault that exhibits a major seismic gap on a plate boundary.

Chapter 2

Robust features of the source process for the 2004 Parkfield, California, earthquake from strong-motion seismograms

2.1 Introduction

The aim of earthquake source process inversion is to find the slip distribution history that produces the best fit to the recorded ground motion. The usual approach in kinematic inversions is to sub-divide the fault plane into rectangular sub-faults, an approach first taken by Trifunac (1974). In each of these sub-faults, source parameters are then retrieved. However, this approach has the disadvantage of requiring a large number of sub-faults to adequately model the fault plane, introducing non-uniqueness into the problem (Das & Kostrov 1990, 1994). In this Chapter, we investigate a recently developed procedure for kinematic inversion involving elliptical sub-faults, which, in addition to creating an intrinsically smooth slip distribution inside the slipping region, has the advantage of reducing the number of parameters to be inverted for. We use only a small number of ellipses, each of which is described by seven parameters. To test this approach with near-field records, we analyse the strong-ground motion data for the 28 September 2004 $M_w6.0$ Parkfield, California

earthquake in order to obtain its robust source features.
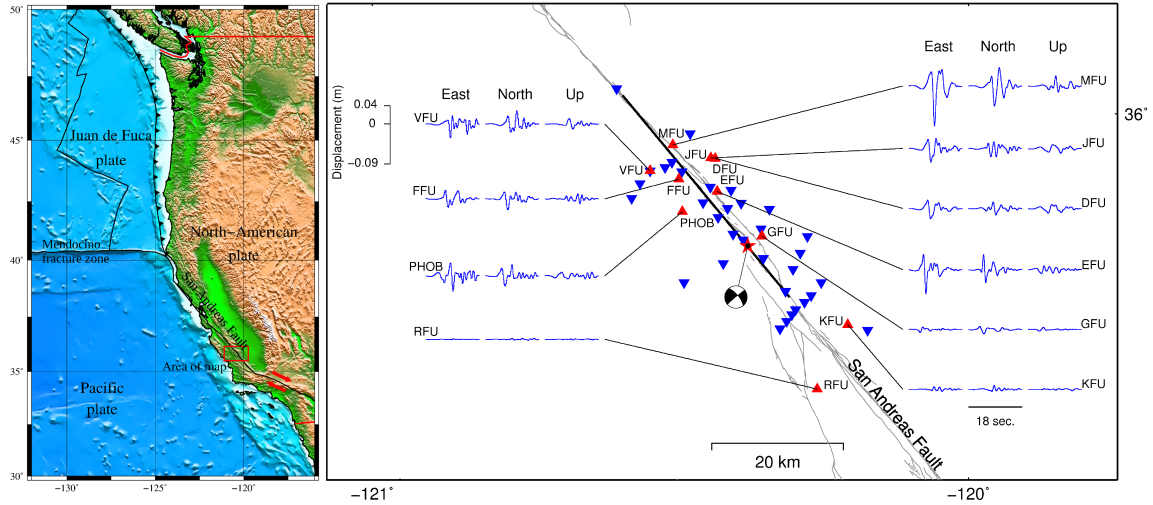
Figure 2.1: Tectonic setting and station distribution for the 28 September 2004 $M_w6.0$ Parkfield, California, earthquake. The digital stations (GEOS network, Borcherdt et al. 1985) are shown as red triangles, while the blue triangles represent available analog stations (CGS network). The fault trace used for the inversions is shown by the thick black line; the grey lines show the surface expression of the San Andreas Fault. The "beach ball" is connected by a thin line to the earthquake epicentre. By convention the compressional quadrants are shown in black while the tensional quadrants are shown in white. Start time of each trace is the origin time of the earthquake.

The Parkfield segment is part of the San Andreas transform fault system which accommodates right-lateral tectonic motion between the Pacific (PAC) and the North-American (NAM) plates (Figure 2.1). Bounded by a creeping section to the north-west and a locked section to the south-east (the Cholame segment), the Parkfield segment has experienced 5 earthquakes of about $M_w6.0$ since 1881 (e.g Bakun & McEvilly 1979; Toppozada et al. 2002; Smith & Sandwell 2006). Knowledge of the occurrence of the 1934 and the 1966 Parkfield earthquakes and the suggestion that the 1966 earthquake was an almost exact repeat of the 1934 earthquake, led to the setting up of the Parkfield Prediction Experiment (Bakun & Lindh 1985). As a consequence, the 2004 earthquake at Parkfield was widely recorded by seismic as well as other types of instruments.

The dataset used here consists of 10 digital three-component strong-motion dis-

placement seismograms with a duration of 18s. Six stations are located on the north-eastern side of the fault and four stations are on the south-western side (Figure 2.1). In addition, there are also 33 analog stations that recorded this earthquake. The use of digital stations has two advantages: firstly, they have absolute timing, and secondly, the first P-wave arrival is recorded. Though we do not use data from analog stations for the inversions, we shall use them later for a cross-check on our model by calculating the displacements at those stations and examining how well the waveforms are matched. All the displacement records were band-pass filtered between 0.16 and 1 Hz. The lower frequency limit is chosen based on the instrument capability of analog stations. Though the lower frequency limit for the digital stations could be taken down to 0.1 Hz, we used 0.16 Hz to keep consistency between different dataset. The higher frequency limit is determined by the accuracy of the velocity structure and Green's functions (Liu et al. 2006).

2.2   Kinematic Inversion Method

We model the fault as a rectangular plane, 40 km long (30 km to the north-west and 10 km to the south-east of the hypocenter) and 16 km deep, its surface projection being shown as a straight black line on Figure 2.1. The size of the fault is based on the location of the aftershocks that occurred within 24 hours of the main shock; strike and dip are taken as N140E and 87°, respectively; hypocentral location is 35.82°N, 120.37°W, at a depth of 8.3 km (Thurber et al. 2006). The velocity model used for the computation of Green's functions is the 1-D structure used by Liu et al. (2006).

The method of elliptical sub-fault approximation has been used for kinematic inversions by Vallée & Bouchon (2004),Peyrat et al. (2010) and Di Carli et al. (2010). In this approach, each elliptical patch is defined by the 7 parameters shown in Figure 2.2.
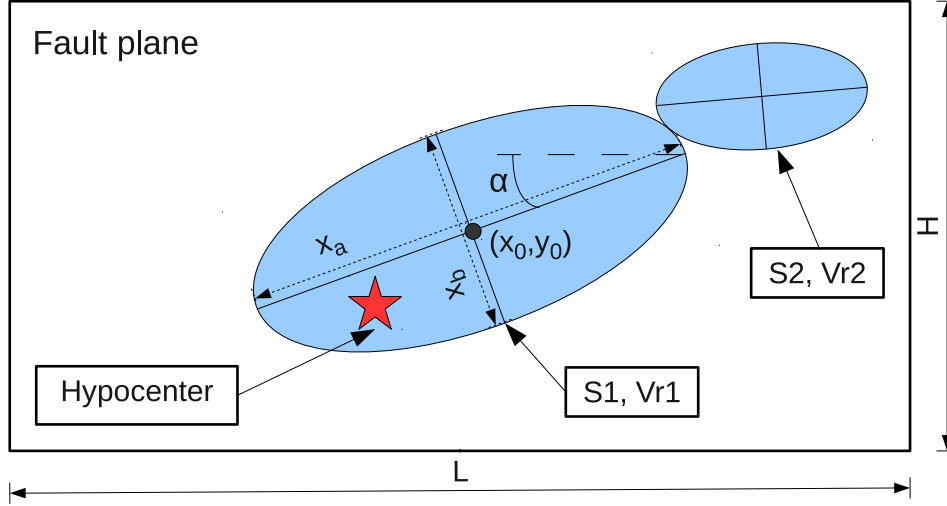
Figure 2.2: Description of the elliptical sub-fault patches (based on Vallée & Bouchon 2004). Each patch can be described by the following parameters: (x_0,y_0): the two coordinates of the ellipse centre. (x_a,x_b): size of semi-major and semi-minor axes, respectively. α: angle between the semi-major axis and the horizontal. s_{max}: maximum slip. The slip distribution (S) inside each ellipse is defined as: $S(x,y) = s_{max}exp\left[-(\frac{x^2}{x_a^2} + \frac{y^2}{x_b^2})\right]$. v_r: the rupture velocity within each ellipse.

In each ellipse, the slip distribution has a smooth Gaussian distribution from the maximum slip amplitude at the centre to zero slip amplitude at boundaries. We require that the first ellipse contains the hypocenter. The centre of the ellipse is calculated using two parameters: h_r and α_h, which control the position of the ellipse relative to the hypocenter. α_h is the azimuth of the centre of the ellipse about the hypocenter. h_r is the distance between the hypocenter and the centre of ellipse (this distance cannot be greater than the length of the semi-major axis). For the first ellipse, the rupture time is calculated assuming a circular rupture front, starting from the hypocenter at $t = 0$, and propagating at the rupture speed associated with the first ellipse (This rupture speed is one of the parameters we invert for). The rupture of the second ellipse is initiated at the point where the circular rupture front, from the hypocenter, makes its first contact with the ellipse. To determine the time when the second ellipse starts rupturing, we calculate the time needed to travel from the hypocenter to the initiation point with the rupture speed of the second ellipse. This rupture speed is also a parameter inverted for. The same process is repeated

for other ellipses, when used.

During an inversion, the aim is to minimise a cost function. This function measures the difference between observed data (u_o) and modelled seismograms (u_s). For our study, we choose the following cost function (Spudich & Miller 1990):

$$\mathcal{E} = \sum_{i=1}^{N_d} W_i \left(\frac{\sum_{tb}^{te}(u_i^o(t) - u_i^s(t))^2}{\sum_{tb}^{te}(u_i^o(t))^2 + \sum_{tb}^{te}(u_i^s(t))^2} \right) \tag{2.1}$$

In Equation 2.1, W_i is the weight given to each station. A higher weight is given to stations with a high signal-to-noise ratio, with values chosen as in Liu et al. (2008). N_d is the number of records and (t_b,t_e) gives the beginning and end times. The search algorithm for the best parameters used in this Chapter is the neighbourhood algorithm (Sambridge 1999a,b), which simultaneously searches for the best values of the parameters. The algorithm follows that procedure: The first step is to uniformly sample n_i models inside the parameter space. The seismograms are then computed for each model, and a misfit value is found for each, using the cost function (ϵ). n_r models with the smallest misfit are then selected from the initial n_i models. According to the distribution of those n_r models, a Voronoi diagram (Voronoi 1908) is built, where each model is associated with a Voronoi cell. A new set of n_i models in the regions defined by the Voronoi cells is then sampled.

Initially, tests were performed using artificially constructed data in order to obtain better insight into the method of inversion, for various cases (see next Chapter). In particular, in *Test 3*, we address the question of the number of ellipses to be used, when no previous study of the earthquake exists.

During each inversion, we choose to fix two source parameters: the rise-time (τ) and the rake, constant over the entire fault. Due to the range of frequencies used in this study, the rise-time may not be resolvable (Liu et al. 2006). Based on a previous kinematic inversion and dynamic modelling, we choose a value of 0.5 seconds for τ (Liu et al. 2006; Ma et al. 2008). Previous studies also show that the rake angle does not have large fluctuations, so it is reasonable to assume the rupture to be

essentially right lateral (Custodio et al. 2009).

2.3 Choice of the Preferred Model

We performed 12 inversions using different parameters to find the source process for the 2004 Parkfield earthquake. Figure 2.3 shows the final slip distributions for the 12 inversions and Table S1 in Appendix A1 gives details of the different inversions, and the resulting source processes.

For the first 11 inversions, two ellipses were used, and in the case of Inversion 12, three ellipses is also considered. The choice of two ellipses was based on the slip distributions inferred from other studies of this earthquake, using different methods (for example, Murray & Langbein 2006; Allmann & Shearer 2007; Ma et al. 2008). For some of the inversions, we also required the second ellipse to be connected to the first one. In that case, (h_r, α_h) relate to the centre of the first ellipse, rather than to the hypocenter. We also carry out some inversions in which we vary the
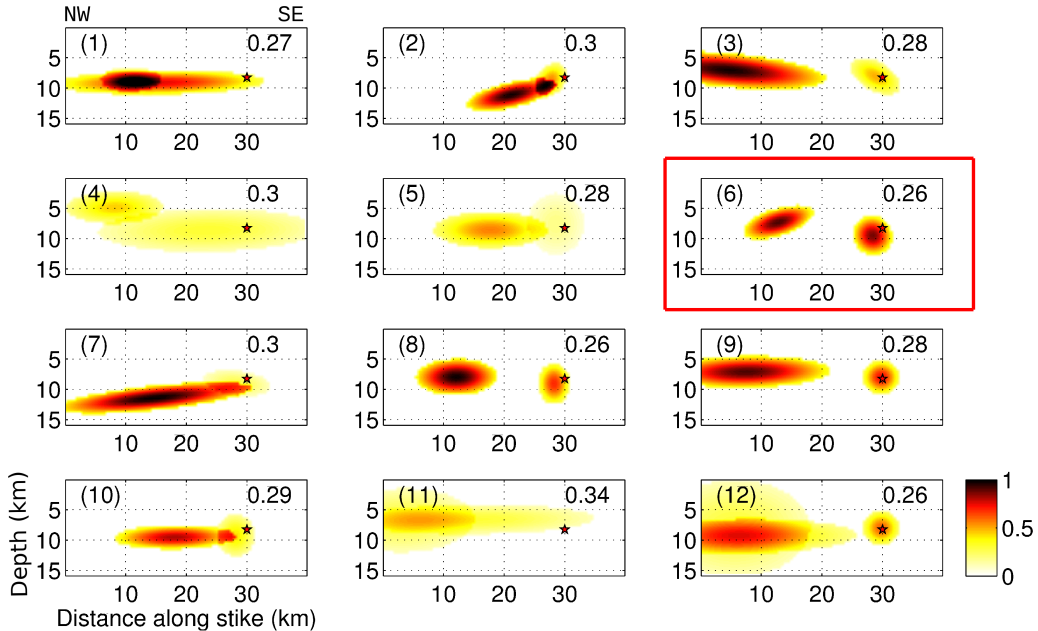
Figure 2.3: Final slip distribution (m) for the 12 inversions (see Table S1 in Appendix A1 for details), using digital stations. The misfit $\mathcal{E}$ is given in the top right of each fault. The red star shows the position of the hypocenter. The preferred model is highlighted by the red rectangle.

14

rise-time (τ) and the rake to examine their influence on the solutions. We discuss next the choice of our preferred model among these inversions.

Figure 2.3 shows that several models have similar misfits, and this leads to the problem of selection of the preferred solution. In spite of the diversity, we find that there is consistency between the models. To highlight the robust features which are independent of the choice of *a-priori* conditions (Table S1 in Appendix A1), a simple average of all the models, inversely weighted by the misfit value, is plotted in Figure 2.4.
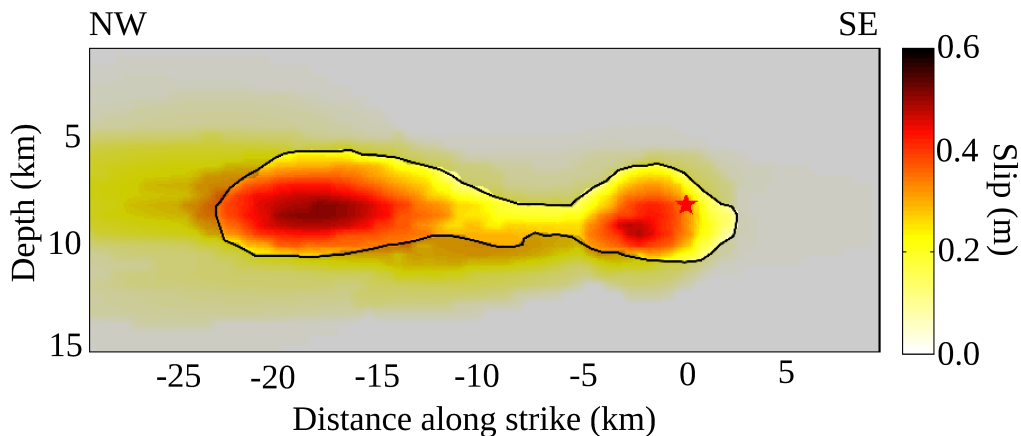
Figure 2.4: Average slip distribution (m) for the 12 slip models. The star shows the position of the hypocenter. The region within the black line shows slip which is higher than the standard deviation. Note that the origin in the strike direction is now at the hypocenter.

In Figure 2.4, we shade regions of slip which are smaller than the standard deviation calculated over the 12 inversions. Therefore, the remaining area focuses on the robust features extracted from the 12 inversions. The misfit of 0.35 for this average model (calculated assuming a constant rupture velocity of 3.0 km/s), falls within the range of values obtained for the 12 inversions, showing that the features highlighted by this averaged slip distribution does not lead to a non-realistic model. On average, two slip patches are necessary to explain the data, one close to the hypocenter and a second one located between 15 and 20 km north-west of the hypocenter, with no slip in the top 5 km. This suggests that the slip distribution

of the preferred model should include these properties. It is also important to note that we find a strong resemblance with previous models of this earthquake, obtained from analysis of strong motion data but using different inversion methods (Ma et al. 2008, Custodio et al. 2009). This indicates that the main features are independent of the approach used to find the slip distribution.

As we also invert for the rise-time and the rake in some of the inversions, it is interesting to discuss their influence on the obtained solutions. The rake varies between 140-180° in all the inversions, with a constant value over the entire fault. This is consistent with the results of Liu et al. (2006) showing that some parts of the fault exhibits a combined right-lateral and up-dip motion. The rise-time shows a higher variability, making it difficult to discuss the reliability of the results. However, it is interesting to see that Inversions 6 and 8 show a similar final slip distribution with different values for the rise time (see Tables of Inversion 6 and 8 in Appendix A1). This implies that this parameter cannot be resolved, and therefore its impact on the final solution may not be significant.

Of the 12 inversions, 8 have significant slip at the hypocenter (Inversions 2, 3, 5, 6, 8, 9, 10, 12 - see Figure 2.3). Among these 8, only Inversion 5 does not have a high-slip patch north-west of the hypocenter. If we also require the preferred model to have a moment value within ±15% of the CMT value (i.e. between 0.96×10^{18} and 1.30×10^{18} N m), then of the remaining 7 models, only Inversions 2, 6, 8 and 10 satisfy this condition. We may reject Inversion 2 from the list of acceptable models, due to the fact that the rupture speed in the first ellipse exceeds the shear-wave speed at the hypocentral depth by ~30%, and no previous study found super-shear rupture speed for this earthquake (e.g. Fletcher et al. 2006, and others referred earlier). Finally, by generating the seismograms at the analog stations for the 3 remaining models, we calculate the values of the misfit for digital stations and analog stations together. Since Inversion 6 has the lowest global misfit (0.82, with 0.26 and 0.56 for digital and analog records, respectively) we take it as our preferred model.

16

2.4 Discussion of the Preferred Model

Figure 2.5 shows the comparison of the waveform data generated by the preferred model with the seismograms recorded at the 10 digital stations. We see that the seismograms show an excellent match in the wave shape and an excellent timing for the main pulses. In general, the amplitude is very well retrieved in the early part of the record, though we note that the later arrivals are not well fitted. It has been known for some time (Li et al. 1990; Ben-Zion 1998) that waves from the fault zone gouge exist and could have a strong effect on the recorded strong-ground motion (Fukushima et al. 2010). The deterioration of the agreement between the data and the solution seismograms in the later portions of the record at some stations may stem from the fact that these fault-zone waves are not modelled in our study. The same reason could also explain the mismatch in amplitude in the early part of some stations (e.g. MFU), situated very close to the fault. There is also a better fit for stations located on the north-east side of the fault compared to those on the south-west side. This is because we use a common 1-D velocity structure for all 10 stations, and we use the one from the north-east side of the fault since more stations (6 out of 10) are located there. The difference in the fit therefore illustrates the impact of the use of an incorrect crustal structure as also shown for synthetic case by Das & Suhadolc (1996).

Figure 2.6 shows the comparison between waveform data and the preferred model solution seismograms at the 33 analog stations. In the forward direction of rupture propagation (i.e. north-west from the hypocenter), a good agreement is observed only for the main pulses. In the backward direction, waveforms at some stations are not well matched. To have a more quantitative view of this mismatch, we plot the misfit values at all the analog stations separately for our preferred model (Figure 2.7a). The red dashed line represents the mean of the individual misfit value, so we can consider that stations above this line exhibit a significant mismatch. We identified 3 locations of higher mismatch (Figure 2.7b), one at the extreme
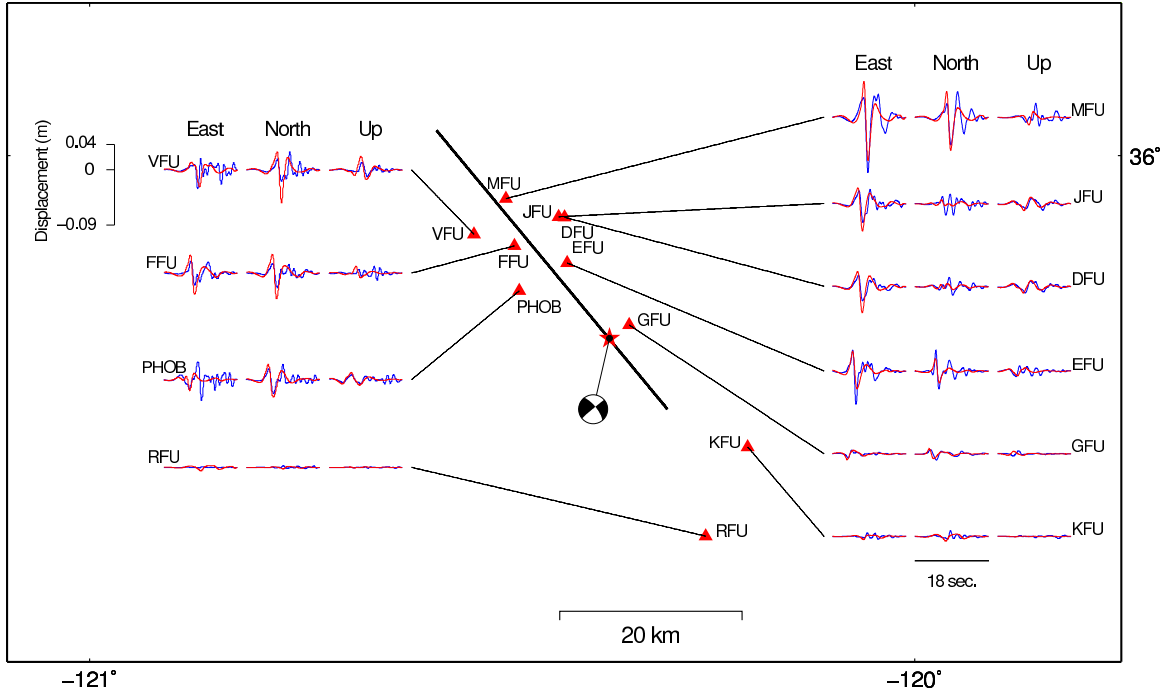
Figure 2.5: Comparison of the solution seismograms from our preferred model (red) with the observed data (blue) at the digital stations. The thick black line shows the modelled fault trace used for the inversion.

north-western end of the fault (Station COAL), one near the region of the high-slip patch (Stations FZ12, FZ15, VC1W, VC2W, VC3W and VC5W) and one in the south-eastern end of the fault (Stations FZ1, C1E, CH2W and CH3W). It is interesting to see that most of these stations are very close to the fault, which is a propitious area to be influenced by fault zone trapped waves (e.g. Li et al. 2004), and could explain the high amplitude and the highest mismatch between observed and calculated seismograms at those stations. For stations close to the high-slip patch, we believe that this area which released a significant amount of the total energy during the earthquake, could have resulted in enhanced site effects, which could explain the higher mismatch for stations at larger distances to the fault.

Previous models using seismic data (e.g. Allmann & Shearer 2007; Custodio et al. 2009) as well as our study have some slip at the hypocenter. A study of the Parkfield earthquake using geodetic data (InSAR and GPS) by Johanson et al. (2006), has argued that slip at hypocenter may be due to rapid after-slip. Hypocentral slip may
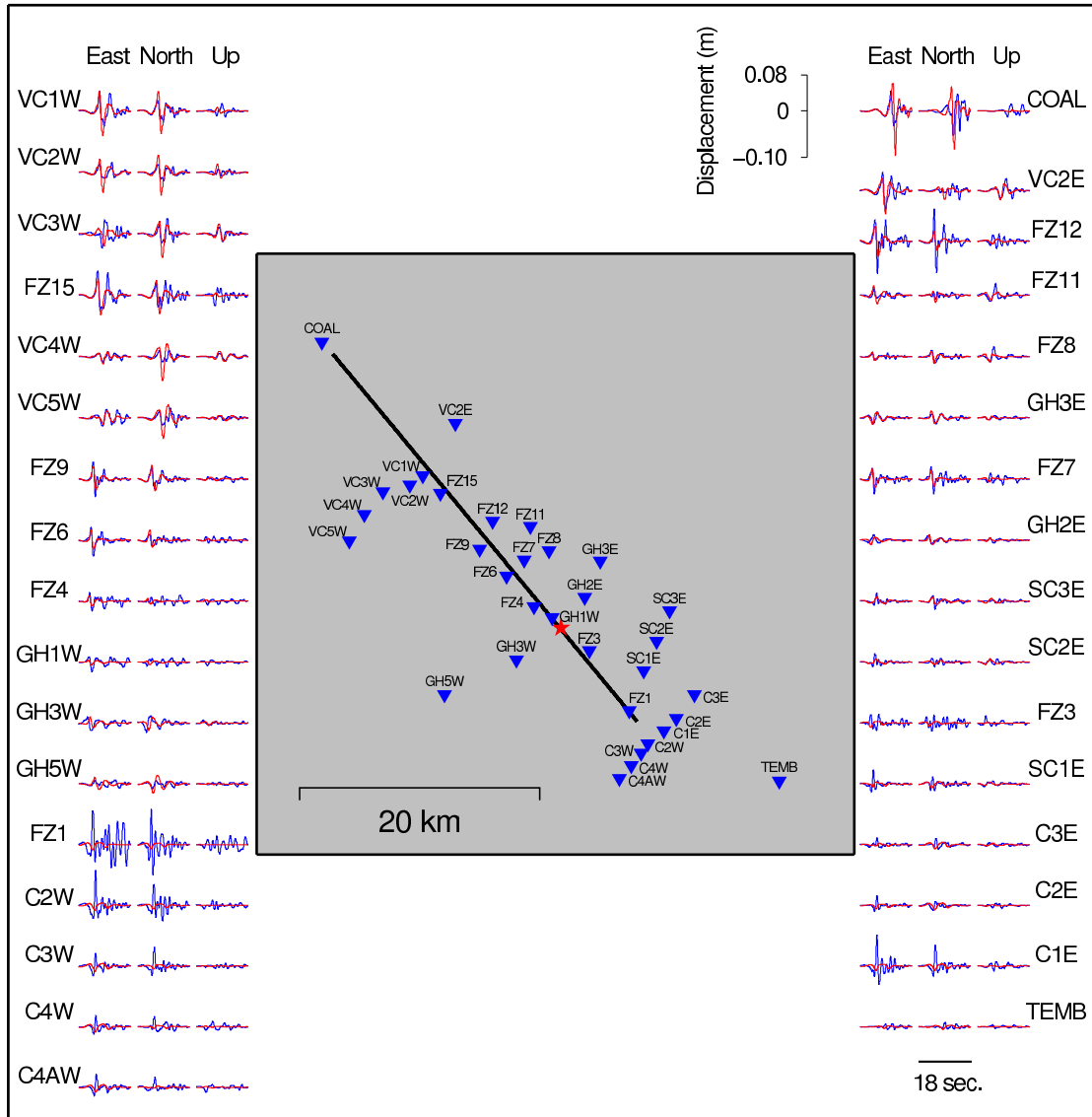
Figure 2.6: Same as Figure 5 but for the analog stations. A comparison of the observed and the solution seismograms for all inversions carried out in this study can be found in Appendix A1.
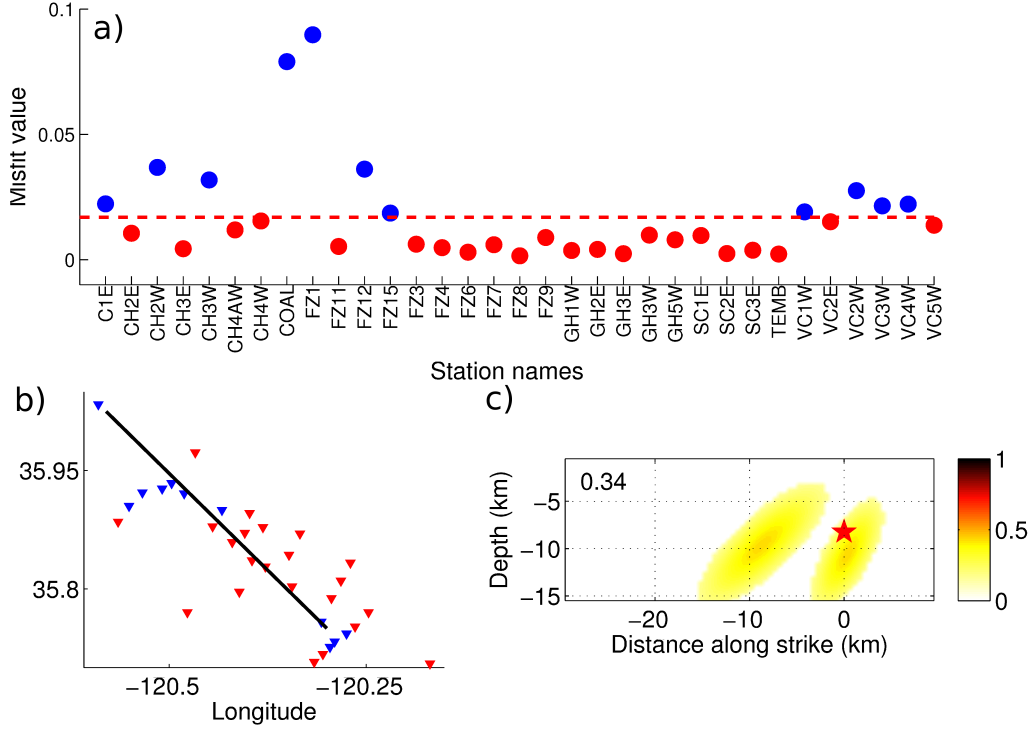
Figure 2.7: Figure 2.7a shows the individual misfit of each analog station, the red dashed line giving their average. Stations with higher misfit than this are shown in blue. Figure 2.7b shows the geographical locations of analog stations. Figure 2.7c shows the slip distribution (m) obtained using all the digital stations and analog stations, except high misfit stations located at the south-eastern end of the fault (i.e. FZ1, C1E, CH2W and CH3W)

only be needed to explain the large amplitude observed at analog stations FZ1, C1E and C2W (see Figure 2.6), as also pointed out earlier (e.g. Shakal et al. 2006).

Also, some of our inversions either have no slip or, no significant slip at hypocenter (Inversions 1, 4, 5, 7 and 11). Among these, Inversions 1, 5 and 9 explain the signal observed at analog stations even better than our preferred model. In order to test if some slip at the hypocenter is a source signal or an artefact induced by fault zone waves affecting stations at the south-eastern extremity of the fault, we run an inversion using all digital and analog stations, except FZ1, C1E, CH2W, and CH3W, which have significantly larger misfit, and the same set-up as in Inversion 6. The resulting slip distribution (Figure 2.7c), shows that even without these high-misfit stations, which also have very high amplitudes, some slip at the hypocenter is needed to explain the data.

2.5 The Source Process

The slip distribution associated with our preferred model (Inversion 6) is shown in Figure 2.8a. The average displacement over the whole fault is of ~ 0.07 m, the maximum displacement within the second ellipse being 0.91 m. This high slip patch is located ~ 17 km from the hypocenter in the north-westerly direction, and explains the high amplitude for stations located in the north-western end of the fault. This is one of the most robust features of the 2004 Parkfield earthquake, and has also been found in other seismic (Allmann & Shearer 2007; Custodio et al. 2009) and geodetic (Johnson et al. 2006; Johanson et al. 2006; Murray & Langbein 2006) studies. It is very important to note that this area of high slip coincides spatially with the hypocenter of the 1966 $M_w 6.0$ Parkfield earthquake (white star in Figure 2.9). Harris & Segall (1987) and Malin et al. (1989) had earlier identified this region of high slip as a locked zone or asperity.
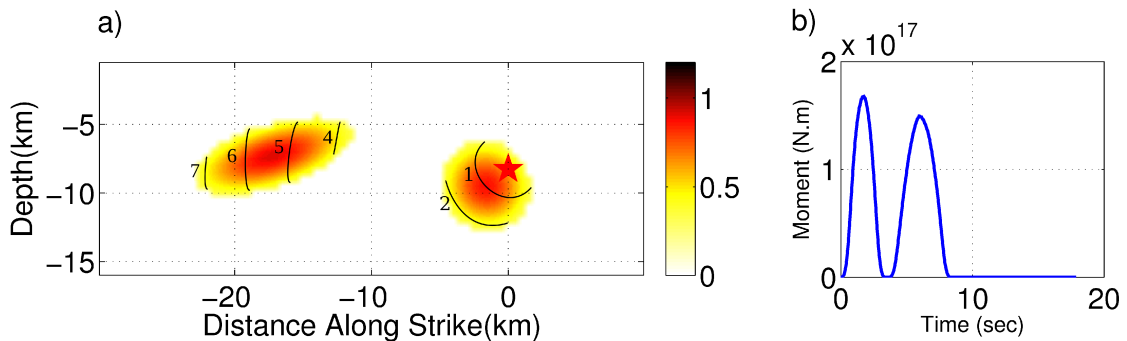
Figure 2.8: (a): Slip distribution (m) for our preferred model (Inversion 6). The red star represents the hypocenter. The black lines show the rupture front at time steps of 1 s. (b): Moment-rate function.

We can therefore interpret this high-slip patch as a permanent asperity, which has been re-activated during the 2004 Parkfield earthquake. Custodio & Archuleta (2007) suggested the presence of persistent asperities in the Parkfield region that can rupture together or individually during earthquakes. The unconstrained inversion of the 1966 earthquake gives a high-slip patch located in the same area as the high-slip patch observed for the 2004 Parkfield earthquake. Though the limited data for

21

the 1966 earthquake is inadequate to resolve details, Custodio & Archuleta (2007)'s study gives an idea of where slip could have occurred, which suggests that some asperities ruptured both in 1966 and 2004, while others broke only in one of the events.

Our preferred model shows that the rupture of the 2004 Parkfield earthquake propagates to the north-west at an average speed of ∼2.7 km/s which is about 80% of the local shear wave speed. Our propagation time agrees well for the first 3 s of the total ∼8 s rupture process, with Fletcher et al. (2006), and with Allmann & Shearer (2007) for the entire process. The hypocentral ellipse has a rupture speed of ∼2.2 km/s. The second ellipse, located between 15 to 25 km north-west of the hypocenter, has a higher rupture speed of ∼3.1 km/s, which is within the range of velocities found in other studies (Liu et al. 2006; Borcherdt et al. 2006; Ma et al. 2008). After the first ellipse completes rupturing in 3 s, a short pause of ∼1 s is observed, before the rupture starts to break the second patch, this taking ∼5 s (Figure 2.8b).

Most inversions of the 2004 Parkfield earthquake find the slip to be continuous over the fault (e.g. Ma et al. 2008; Custodio et al. 2009). However, as emphasised by Vallée & Bouchon 2004, the aim of the method used here is to focus on finding the major slip areas, which explain a large part of the waveform and are also the best resolvable features of the co-seismic slip. This is why we do not observe any transitional slip between patches while other models do. This gap is therefore unlikely to be a real characteristic of the source process of Parkfield earthquake (see Section 4.7 in Chapter 4 for further discussion on this issue).

2.6   Relation between High-Slip Patch and Seismicity prior the 2004 Parkfield Earthquake

We used the catalogue of Thurber et al. (2006) from 3 January 1984 to 28 September 2004, to examine the relationship between previous seismicity and the north-west asperity. Figure 2.9 shows the locations of the main earthquakes ($M_w > 3$). This figure shows that earthquakes, especially larger ones, surround the region of highest slip. This observation is in good agreement with the hypothesis of an asperity in this area, which produces stress accumulation at its edges, that is partly released during smaller earthquakes. This correlation between prior seismicity and asperities has been observed in previous studies (e.g. Hsu et al. 1985).
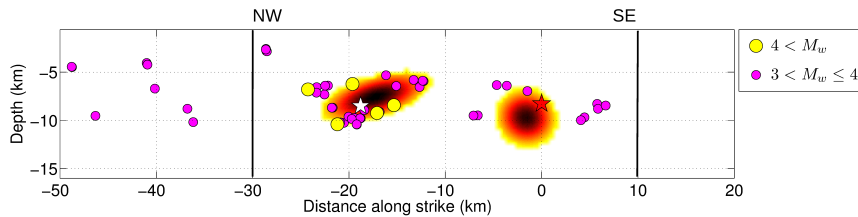
Figure 2.9: Larger background seismicity ($3 < M_w \leq 5$) prior to the 2004 Parkfield earthquake, from January 3 1984 to the day before this earthquake, plotted over our preferred slip distribution. The catalogue used is from Thurber et al. (2006). The black lines show the limits of the fault plane that is used during the inversions.

Ben-Zion & Rice (1993) showed that this "Parkfield asperity" has a major influence on prediction attempts, and must play a role in the slip budget of the Parkfield segment (the part of the San Andreas fault which experienced the 5 last $M_w6.0$ Parkfield earthquakes). Toké & Arrowsmith (2006) show that the north-western part of the Parkfield segment has a slip deficit close to zero, since this is adjacent to the creeping section of the San Andreas Fault. However, the south-eastern part of the Parkfield segment (the Cholame segment) has a slip deficit of ~ 5 m since 1857. The Parkfield segment also has a slip deficit but slightly lower than the Cholame segment (~ 3.5 m), due to the release of energy by the recurrent Parkfield earth-

23

quakes. So, a hypothetical earthquake, which breaks the Cholame segment would have a higher magnitude if it also breaks the Parkfield segment at the same time.

2.7   Relation between Main Shock Slip and Aftershocks

We used the relocated aftershock sequence of the 2004 Parkfield earthquake of Thurber et al. (2006) from 28th September 2004 to 30 June 2005, to compare their locations with our slip distribution. One salient feature is the horizontal level delineated by small aftershocks around 5-6 km depth (Figure 2.10a). Waldhauser et al. (2004) suggest that this level may represent a change from creeping (above), to locked (below) in the inter-seismic period. Though the depth of the ellipses in our inversion was not fixed to be below this level, the seismic data requires the ellipses to lie below it, thereby supporting Waldhauser et al. (2004). The larger aftershocks ($M_w > 3$, Figure 2.10b) mainly lie where no slip has been observed, though there is a cluster $\sim$19 km north-west of the hypocenter, located at the edge of the northwestern high slip patch, where there is a sharp change from high to low slip. This behaviour of aftershocks has been observed previously (see Das & Henry 2003 for other examples) and provides independent support for the reliability of the position of this high slip patch.

The co-seismic slip distribution of the preferred model shows also a good agreement with post-seismic deformation observed after the earthquake. Studies using geodetic data (e.g. Johanson et al. 2006; Murray & Langbein 2006; Bruhat et al. 2011 and Houlié et al. (2013)) show that most of the deformation (after-slip and post-seismic slip) surrounds the region of co-seismic slip obtained by our inversion. We note that no post-seismic slip is observed in the region in between the ellipses, suggesting that this area might have slipped during the rupture. However, as mentioned previously, our inversion procedure focuses only on the major regions
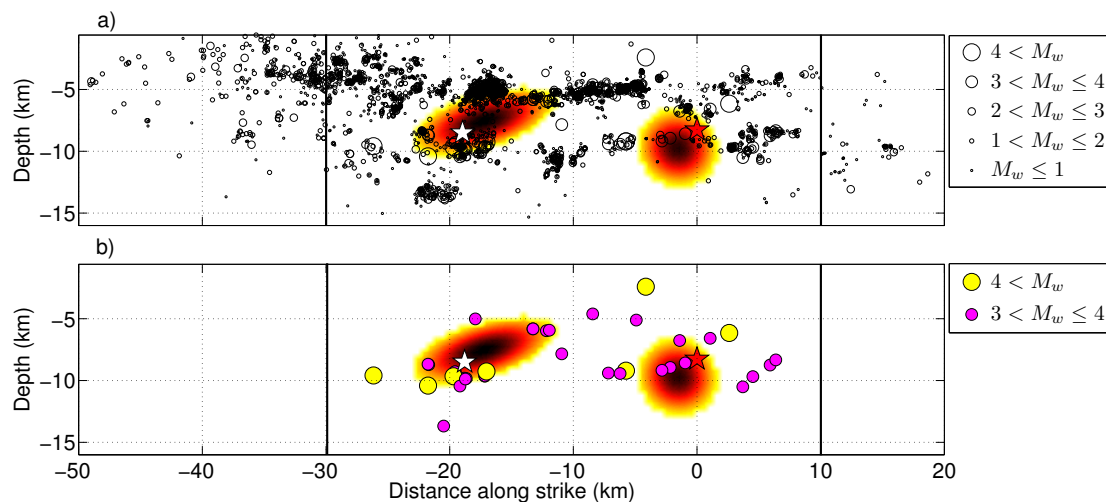
Figure 2.10: The aftershocks from 28 September 2004-30 June 2005 (Thurber et al. 2006), shown as black circles, plotted on our preferred the slip distribution. (a): All aftershocks (see key). (b): The larger aftershocks ($3 < M_w \leq 5$).

of slip, which could explain why no slip is observed in this area. These studies also show that post-seismic slip has occurred on the shallow portion of the fault (<5 km deep), above the horizontal level of aftershocks, where no co-seismic slip is observed. At depth between 16 to 30 km, in the portion below the hypocenter, non-volcanic tremor has been observed by Shelly 2009, with an increase of their activity 3 months prior the 2004 Parkfield earthquake. It is believed to be indicative of an increase of creep beneath the hypocenter, which could have influenced the nucleation of the 2004 Parkfield earthquake, especially with respect to its location compared to the 1966 Parkfield earthquake. These observations provide additional evidences about the reliability of the source process obtained by the inversion.

2.8 Conclusion

We performed a kinematic inversion of the 28 September 2004 $M_w 6.0$ Parkfield, California, earthquake using a recently developed method, which defines the slip distribution as an aggregate of ellipses. The method was tested using artificial data (see next Chapter). We fit well the early portions of most seismograms and suggest

25

that modelling of fault zone waves is required to explain some of the later waveforms. Our preferred slip distribution (Inversion 6) is composed of two distinct ellipses, and shows no slip in the top 5 km. A horizontal lineation of small aftershocks at this depth of 5 km has been suggested as marking a sharp transition in the inter-seismic slip rate. The highest slip occurs in a region located between 15 and 20 km from the hypocenter, in the north-western direction. This patch can be interpreted as a permanent asperity, which is activated during large earthquakes. The presence of this asperity has important implications for seismic hazard assessment since it may be a characteristic feature of the Parkfield earthquakes.

Chapter 3

Stability of the Earthquake Source Process Obtained by Kinematic Inversions

3.1 Introduction

Kinematic inversion is used to obtain the earthquake rupture process from observed seismic waveforms but has various sources of uncertainties.

A kinematic inversion relies in part on data processing, model parameterization and the algorithm that is used to perform the inversion. The uncertainties associated with each of these come from "subjective choices", i.e. choices that depend on the group who attempt the inversion. Several studies have investigated the impact of such choices. Using strong ground motion seismograms, Olson & Anderson (1988) have tested the accuracy of the inversion scheme that was used during their kinematic inversion. Hartzell (1989) carried out further investigation on that same topic by testing the influence of the choice of the algorithm on the final results. The studies of Das & Kostrov (1990, 1994) and Das & Suhadolc (1996) examined the impact of adding constraints on the inversion procedure (e.g. positivity constraints and constraints on the moment). Das & Suhadolc (1996) have also studied what the effects are of constraints on the rupture speed, in the case of the inversion of a Haskell-type rupture model, with prescribed rupture speed. Saraò et al. (1998)

have meanwhile investigated how the spatial grid-size affects the results of an inversion. Hartzell et al. (2007) examined the stability of a finite-fault inversion when the inversion is performed under different *a-priori* assumptions.

Kinematic inversion also depends on constraints that are associated with the state of knowledge at the time of the inversion. Those imposed constraints are for instance geometrical constraints (e.g. what is the dip, rake and strike of the fault, its size, etc.) or constraints due to a lack of knowledge of the geology of the studied area. Using strong-motion seismograms, Beroza & Spudich (1988) have investigated the impact of noise on the data, also studied later by Saraò et al. (1998). Das & Suhadolc (1996) looked at the effect of incorrect crustal structure, a topic which was studied by several other authors (e.g. Saraò et al. 1998; Graves & Wald 2001). Saraò et al. (1998) also examined the influence of station coverage on the inference of the rupture history. Zhou et al. (2004), meanwhile, assessed the effect of the fault geometry on the final results.

In the present study, we focus on the first aspect, which are the uncertainties associated with the "subjective choices" that we made prior our study of the kinematic rupture process of the September 2004, Parkfield, earthquake (hereinafter abbreviated as Chapter 2). In particular, we investigate the performance of the elliptical sub-fault approximation used along with Neighbourhood Algorithm (NA) to find the rupture process of an earthquake. We also look at the behaviour of the NA in the search of the optimal solution. In addition, we examine how our data processing have influenced the obtaining of the preferred solution of Chapter 2. We therefore perform another inversion in which we change the frequency content in our seismograms. We also invert velocity records instead of displacement records. And finally, we vary the duration of the seismograms used to perform an inversion and see how it affects the final results.

3.2 Method for Kinematic Inversion

The method for the kinematic inversion consists of using n patches of elliptical shape to model the rupture history of the earthquake (see also Vallée & Bouchon 2004; Di Carli et al. 2010 and Ruiz & Madariaga 2011). We invert for each elliptical patch, the position of the centre of the elliptical (x_o, y_o), the size of the semi-major and semi-minor axes $(x_a, y_a$, respectively) and α (angle between the semi-major axis and the horizontal). Those 5 parameters thus describe the geometry of the elliptical patch. To describe the slip history within each ellipse, we also invert for the slip distribution $(S(x, y))$ and the rupture velocity v_r, assumed to be constant inside each ellipse (see Fig. 3.1). We define the distribution of slip inside the ellipse as $S(x, y) = s_{max} exp \left[-(\frac{x^2}{x_a^2} + \frac{y^2}{x_b^2}) \right]$; s_{max} is the maximum slip amplitude and is the parameter that we invert for. Inside each ellipse, the rupture time is calculated assuming a circular rupture front, originating from the hypocenter, starting at $t = 0$ and propagating at a speed v_r. For the ellipses that do not touch the hypocenter, the rupture is initiated at the point and at the time where a virtual circular rupture front, coming from the hypocenter and propagating at a speed v_r, makes its first contact with the ellipse.

To search for the optimal solution, the inversion algorithm aims to minimise a cost function that measures the difference between the observed data (u_o) and the modelled seismograms (u_s). We adopt the same criterion as that in Chapter 2 in order to make direct comparisons of the fit between the two studies:

$$\mathcal{E} = \sum_{i=1}^{N_d} W_i \left(\frac{\sum_{tb}^{te}(u_i^o(t) - u_i^s(t))^2}{\sum_{tb}^{te}(u_i^o(t))^2 + \sum_{tb}^{te}(u_i^s(t))^2} \right). \tag{3.1}$$

In Equation 3.1, W_i is the weight given to each record with values chosen as in Liu et al. (2008). N_d is the number of records and (t_b, t_e) are the beginning and end times of each record.
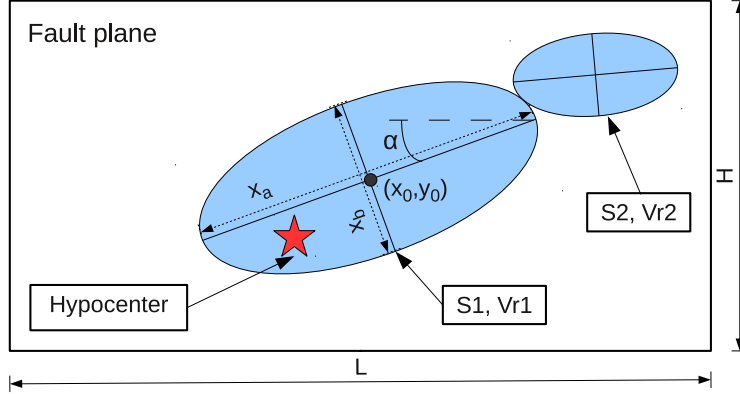
Figure 3.1: Description of the elliptical sub-fault patches (same as Fig. 2.2 in Chapter 2). Each patch can be described by the following parameters: (x_0,y_0): the two coordinates of the ellipse centre. (x_a,x_b): size of semi-major and semi-minor axes, respectively. α: angle between the semi-major axis and the horizontal. s_{max}: maximum slip. The slip distribution (S) inside each ellipse is defined as: $S(x, y) = s_{max}exp\left[-(\frac{x^2}{x_a^2} + \frac{y^2}{x_b^2})\right]$. v_r: the rupture velocity within each ellipse.

The search algorithm for the best parameters used here is the Neighbourhood Algorithm (NA) developed by Sambridge (1999a,b). First, it samples n_i rupture models inside the entire parameter space. For each rupture model, the seismograms are calculated and the misfit between calculated and observed seismograms is computed using the cost function. From the n_i rupture models, n_r with the smallest misfit value are selected. From the distribution of the n_r models inside the parameter-space, a Voronoi diagram (Voronoi 1908) is created, where each model is enclosed within a Voronoi cell. Geometrically, one Voronoi cell is a polyhedron that encloses a region of the parameter space containing models that produces waveforms fitting similarly the data. A new set of n_i models is then sampled inside the different Voronoi cells. This process is then repeated for a certain number of iterations. In Chapter 2, the search of the optimal solution is carried out for 2000 iterations, n_i is set to 30 and n_r is set to 10. The same set-up for the NA is used in this study.

3.3 Kinematic inversions of synthetic earthquakes

In order to analyse the performance of our kinematic inversion method, we first carry out three inversions using three artificial datasets, generated from three different rupture process. The artificial 3-component displacement waveforms are calculated at 10 stations distributed around the fault plane and thus for each of the three rupture models (see Figure 2.1 for the general configuration used during the synthetic tests). The artificially created displacement records are "noise-free" and band-pass filtered between 0.16 and 1.00 Hz using a 4th order Butterworth filter.

In each case, we assume a perfect knowledge of the fault plane geometry: 40 km long and 16 km wide, with a strike of 140°N and a dip of 87°.The fault geometry is chosen so that it reproduces that used for the inversions of the source process of the Parkfield earthquake presented in Chapter 2. The Green's functions on the fault plane are computed for 2560 discrete points, separated by 500 m along strike and 500 m along dip. We calculated them using the code AXITRA of Cotton & Coutant (1997), which is based on the discrete wavenumber decomposition of Bouchon (1981) and the reflectivity method of Kennett & Kerry (1979).

The velocity structure used during the synthetic tests is a 1-D structure composed of 4 layers (see Table 3.1). This is the same structure as the one used to generate the k^{-2}-type slip distribution used in *Test 2* and *Test 3* (Ruiz 2012, personal communication). During the inversions, we also assume a perfect knowledge of the velocity structure.

Depth of the top of the layer (m)	V_p (m/s)	V_s (m/s)	ρ (g/m^3)	Q_p	Q_s
0.0	5500.0	3180.0	2400.0	600.0	300.0
5500.0	6300.0	3640.0	2670.0	800.0	400.0
16000.0	6700.0	3870.0	2800.0	1000.0	500.0
35000.0	7800.0	4500.0	3000.0	1000.0	500.0

Table 3.1: Velocity structure used to generate the artificial displacement records for the three tests. V_p refers to the P-wave velocity, V_s to the S-wave velocity, ρ to the bulk density, Q_p to the quality factor of the P-wave and Q_s to the quality factor of the S-wave.

We also fix the rake to a value of 180° and rise-time to a value of 0.5 s to create the artificial data as well as during the inversion.

Test 1:

The first rupture history that we attempt to retrieve is that of the preferred model found in Chapter 2. It is composed of two distinct ellipses of about equal slip amplitude. The rupture initiates 30 km south-east of the north-western end of the fault plane and is located 8.26 km deep. The first ellipse is located at the hypocenter and the second one is located about 20 km away from the first one. The rupture speed of the hypocentral ellipse is 2.14 km/s while the second ellipse breaks at 3.08 km/s. This rupture model has the advantage that it is created from the same methodology as that used during the inversion and it is also interesting because it shows variable rupture speed.

Figure 3.2 compares the input rupture process (i.e. the rupture process used to generate the artificial dataset, hereafter called IRP1) and the output rupture process (i.e. the outcome from the inversion of the artificial dataset, hereafter ORP1). The inversion reaches a misfit value that is very small ($\sim$0.003), which indicates that no differences are visible between the artificial waveforms and the calculated waveforms. IRP1 and ORP1 therefore produce the same displacement waveforms and cannot be distinguished from one another (see Figure A2.1 in Appendices A2 for the comparison between calculated and artificial waveforms). However, we observe that the two rupture processes are not identical. Overall, they show the same pattern with two distinct ellipses: one near the hypocenter and one about 15 km away of the hypocenter. However, the final seismic moment of ORP1 is 1.64×10^{18} Nm, while IRP1 has a seismic moment of 1.20×10^{18} Nm, showing a slight difference in the amount of energy released in the input and the output model. The rupture speed obtained from the inversion is 2.21 and 3.07 km/s for the hypocentral ellipse and the second ellipse, respectively instead of 2.14 and 3.08 km/s for IRP1. The differences
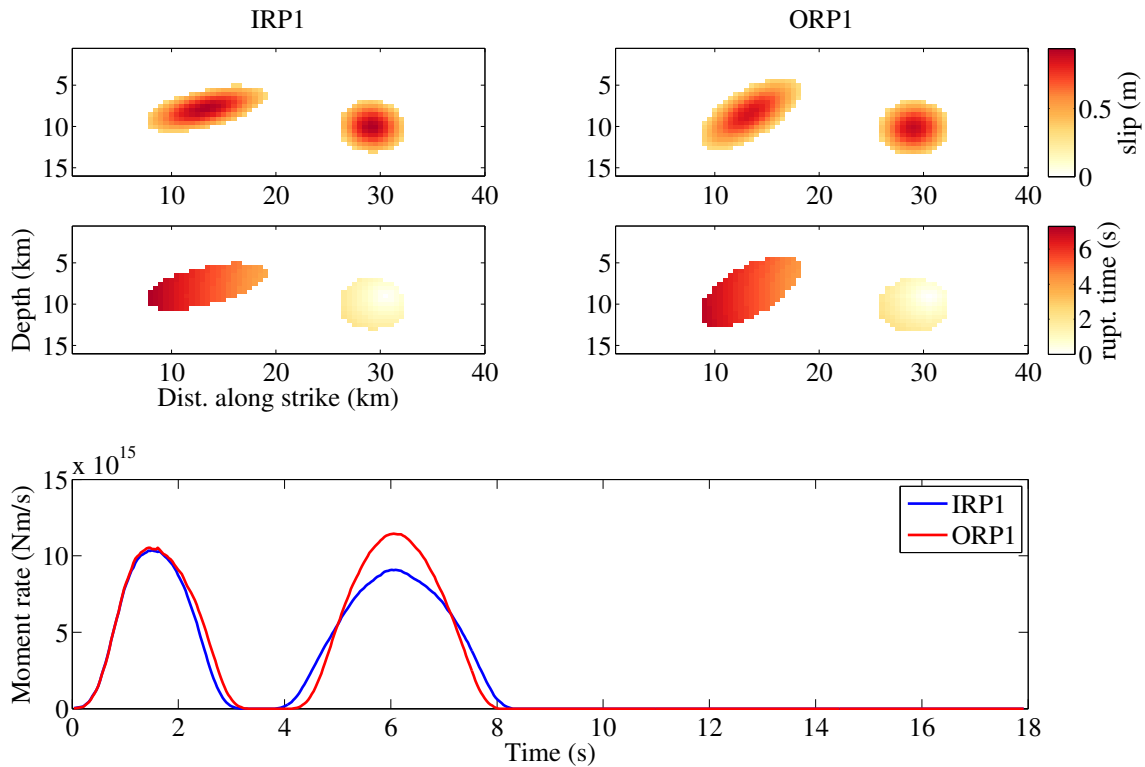
Figure 3.2: Comparison between the final slip distribution and isochrone distribution of the rupture process used to generate the artificial dataset (IRP1) and the final slip distribution of the outcome from the inversion of the artificial dataset (ORP1). We also show a comparison of the time evolution of the moment-rate of IRP1 and ORP1.

in seismic moment and rupture speed can be observed in Figure 3.2. The fact that the two rupture models fit equally well the synthetic data is one illustration of the non-uniqueness associated to kinematic inversion.

Test 2:

The second rupture history that we attempt to retrieve (hereafter called IRP2) has a k^{-2}-type slip distribution created following the method described in Ruiz et al. (2007) (see IRP2 in Figure 3.3). To generate the synthetic displacement waveforms, we use a circular front propagating at constant rupture speed of 3.0 km/s over the entire fault. During the inversion we allow the rupture to occur only on a single ellipse that is forced to be connected to the hypocenter.
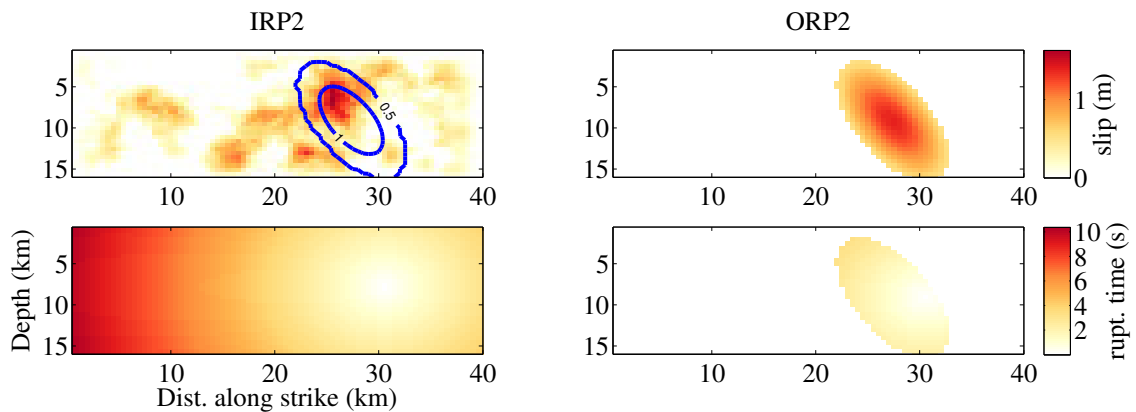
Figure 3.3: *Test 2* - The top and bottom figures of IRP2 show the artificial k^{-2}-type slip distribution and the isochrones of a circular rupture front propagating at 3 km/s. On the slip distribution we also show iso-contour of slip from the slip distribution of ORP2. The top and bottom figures of ORP2 show the final slip distribution obtained by the inversion and the isochrones of the rupture process.

The rupture model obtained by the inversion (hereafter called ORP2) is shown in Figure 3.3. The rupture in ORP2 occurs at a speed of 3.0 km/s that is exactly the same speed as that used for IRP2. If we look at the final slip distribution, we observe that the main asperity of IRP2 and the ellipse of the ORP2 are spatially close, although the ellipse is two times larger than the main asperity. The final seismic moment of ORP2 (2.90×10^{18}) is about half of the final seismic moment of IRP2 (5.40×10^{18}). The inversion is therefore blind to slip of small amplitudes that are outside of the region where most of the energy is released. The ellipse therefore incorporates the slip from the main asperity and from its close surrounding region within a single patch.

We also compare the final slip distribution of the inverted model with a low-frequency filtered version of the slip distribution of IRP2 (Figure 3.4). We used a filter in the form of an ideal 2-D low-pass filter, which suppress spectral amplitudes associated with wavenumbers higher than a cut-off value (D_0). After several tests, we found that if we use a D_0 of 0.08 m^{-1}, we obtain a filtered slip distribution that is similar to the one of ORP2. The filter thus removes the structures that have a size less than 12.5 km. This shows that the elliptical sub-fault approximation

34
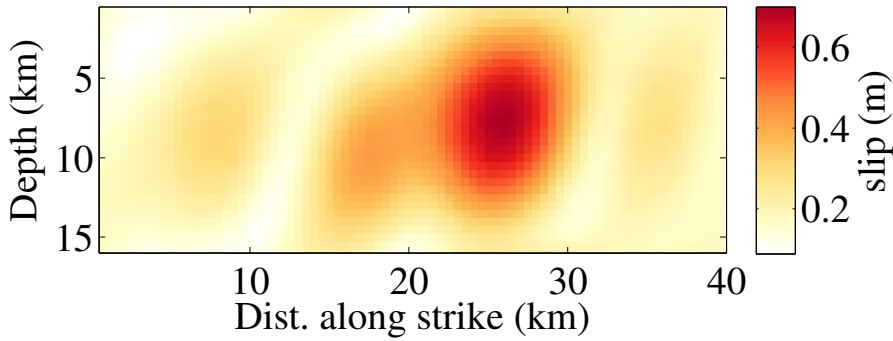
Figure 3.4: *Test 2* - Slip distribution obtained when a low-pass spatial filter is applied to the artificial slip distribution of IRP2.

retrieves a smoothed image of the heterogeneous slip distribution. The fact that it recovers very well a low-frequency filtered version of the slip distribution of IRP2 suggests that the spatial resolution of the kinematic inversion blurs the details of the source process. It focuses only on the large scale robust features of the earthquake, creating an image of the rupture source process that reflects the resolution that one has on the rupture process. The seismograms exhibit a good fit ($\mathcal{E} = 0.10$), with small mismatch at some stations (see Figure A2.2 in Appendices A2). This can be explained by the asperities of small amplitude, which we do not try to extract as the goal of this method is to obtain the main area of large slip.

Test 3:

The third rupture history that we attempt to retrieve (hereafter called IRP3) also has a k^{-2}-type slip distribution and shows two distinct large amplitude asperities: one near the hypocenter and one ∼15 km away from the hypocenter. Once again, to generate the synthetic displacement records, we use a circular rupture front propagating at 3.0 km/s over the entire fault.

One goal here is to gain insight into how to choose the number of ellipses to be used in the inversion, when no other studies of an earthquake exists. It was suggested by Vallée & Bouchon (2004) that the number of ellipses should be increased when part of the signal, believed to be caused by source, is not fitted, a procedure that

35

they applied to the 1995 Jalisco (Mexico) earthquake. The same procedure was also used for the study of the Tocopilla earthquake by Peyrat et al. (2010). In order to explicitly illustrate this, we perform two inversions. In the first one, we use only one ellipse to invert for the rupture history (hereafter called ORP3a) while in the second one, we use two ellipses to invert for the rupture history (hereafter called ORP3b). A comparison between IRP3 with ORP3a and ORP3b are shown in Figure 3.5 and Figure 3.6, respectively. For both cases, we do not discuss the rupture speed because the two inversions retrieved perfectly the 3.0 km/s used in IRP3.
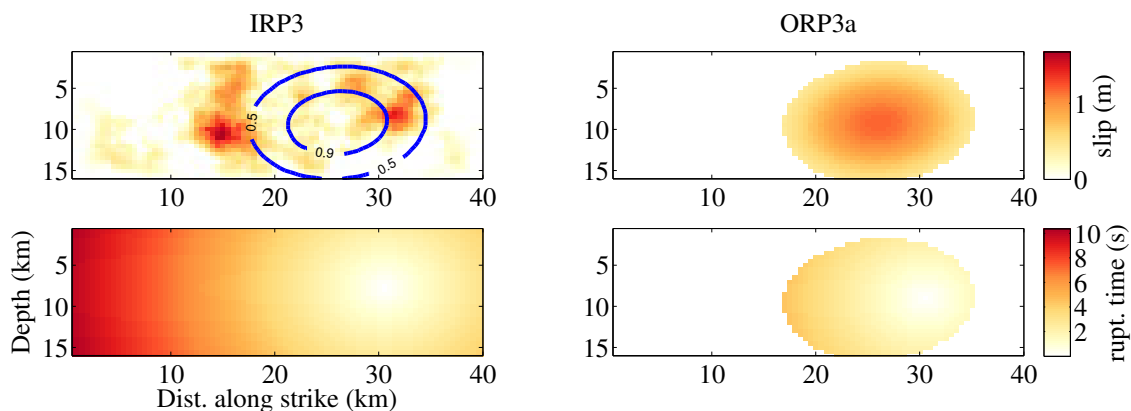
Figure 3.5: *Test 3* - The top and bottom figures of IRP3 show the artificial k^{-2}-type slip distribution and the isochrones of a circular rupture front propagating at 3 km/s. On the slip distribution we also show iso-contour of slip from the slip distribution of ORP3a. The top and bottom figures of ORP3a (i.e. the rupture model obtained from an inversion using only one ellipse) show the final slip distribution obtained by the inversion and the isochrones of the rupture process.

In ORP3a, we see the inversion has produced a final slip distribution with an ellipse located at the centroid of the slip distribution. However, examination of the displacement waveforms (see Figure A2.3 in Appendices A2) shows a non-negligible mismatch between the solution seismograms and the artificial ones ($\mathcal{E} = 0.17$). In a real problem, this would have alerted us to the fact that a higher number of ellipses are needed.

We next used two ellipses to see if the fit is improved. The final slip distribution of ORP3b shows that the two-ellipses inversion correctly retrieves the two major asperities. It also shows a small patch with high amplitude between the two ellipses.
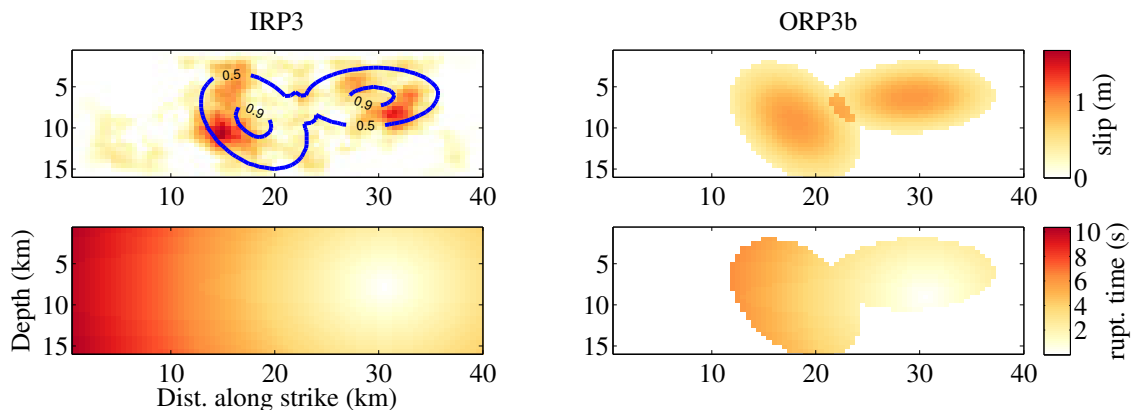
Figure 3.6: *Test 3* - The top and bottom figures of IRP3 show the artificial k^{-2}-type slip distribution and the isochrones of a circular rupture front propagating at 3 km/s. On the slip distribution we also show iso-contour of slip from the slip distribution of ORP3b. The top and bottom figures of ORP3b (i.e. the rupture model obtained from an inversion using two ellipses) show the final slip distribution obtained by the inversion and the isochrones of the rupture process.
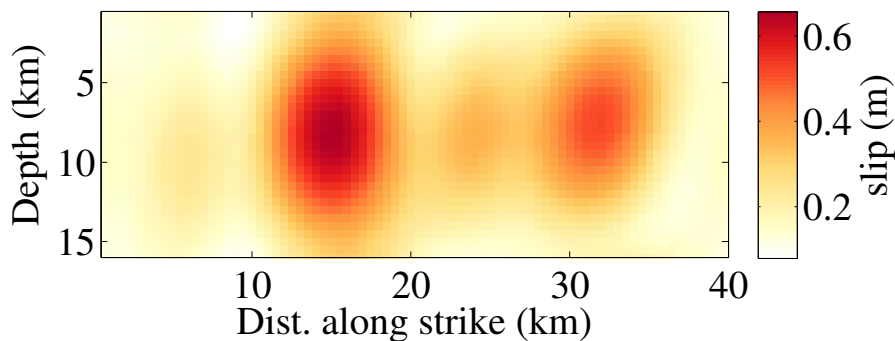
Figure 3.7: *Test 3* - Slip distribution obtained when a low-pass spatial filter is applied to the artificial slip distribution of IRP3.

This does coincide with a small peak in amplitude in the slip distribution in IRP3, but is more likely an artefact of the inversion due to the proximity of the two ellipses. When we compare slip distribution of ORP3b with the filtered version of the slip distribution of IRP3, using the same 2D low-pass filter as described previously (Figure 3.7), we observe again a very good agreement between the final slip distribution of ORP3b and a smoothed version of the slip distribution of IRP3.

It shows that, like in the previous test, our inversion method focuses on the main features of the earthquake. The fit to the waveforms has also significantly improved ($\mathcal{E} = 0.09$). A comparison of the synthetic data and the calculated waveforms from

ORP3b are shown in Figure A2.4 in Appendices A2.

3.4   The Neighbourhood Algorithm to Search for the Optimal Solutions

As mentioned earlier, each kinematic inversion in Chapter 2 involved 2000 iterations. Each parallel iteration computes the waveforms at each station for 30 different models and one extra iteration is needed at the beginning of the procedure in order to initiate the inversion. The additional iteration computes the waveforms for 40 different models. Therefore, one inversion computes the waveforms for 60040 models. The use of 2000 iterations was chosen in Chapter I so that the NA has converged for 11 out of the 12 inversions (see Figure A2.5 in Appendices A2). If we specifically look at Inversion 6 (the preferred model in Chapter 2), the convergence is complete. So, we can assume that there is no model that fits the data better than the last computed model. However, it would be interesting to know if the process could have been stopped earlier without affecting the main conclusions of Chapter 2. To explore this issue, we investigate the behaviour of the NA during this specific kinematic inversion.

We examine all the models sampled by the NA and look at the convergence of each of the 14 parameters (Figure 3.8). We can see that some parameters converge very rapidly, and some show more variations, even at the end of the inversion. We do not focus on the parameters α and h_r, controlling the position of the ellipse around the hypocenter, because the allowed range does not translate into significant change in the position of hypocentral ellipse.

It is interesting to note that the maximum slip amplitude inside each ellipse can vary significantly without affecting the value of the misfit by much. It is therefore the spatial position of the ellipses and the rupture speed that control the convergence. Those two characteristics control the space-time position of the rupture front,
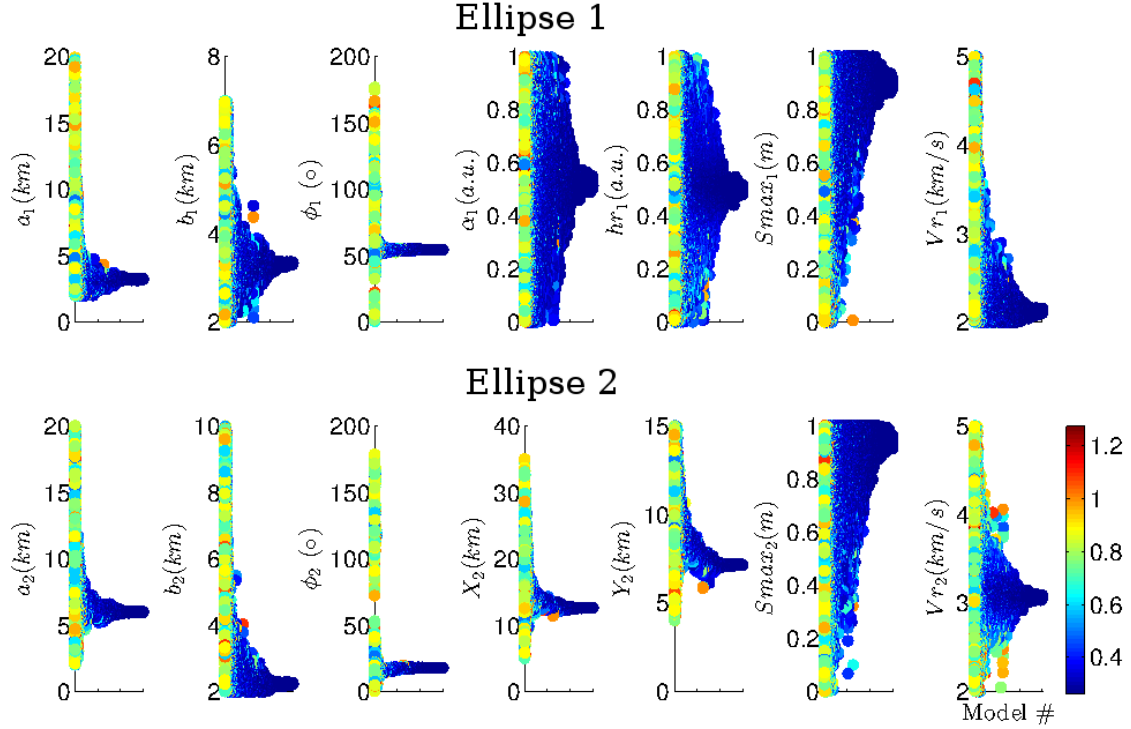
Figure 3.8: Convergence curve for each parameter. The top row is related to the hypocentral ellipse and the second row is related to the second ellipse located to the left of the hypocenter (see Figure IRP1 in Figure 3.2, which represents the slip history obtained for Inversion 6). Each dot is colour-coded according the misfit value with black for low and light grey for large values.

governing the position in time of the pulses on the seismograms. The significant variations of the misfit value observed when the position of the rupture front is adjusted during the course of the inversion, is because the inversion depends very non-linearly on the position of the rupture front. Once fixed, the seismograms become linearly dependent on the other parameters.

As a result, the NA divides automatically the inversion procedure into three steps. First, it stabilises the position of the ellipses as well as the rupture speed of each of them. Once the spatial location of the ellipses is stabilised, the rupture speed is adjusted more finely to decrease the misfit. Finally, once the rupture speed approaches its final value and that the rupture front is more or less stable, the slip amplitude of each ellipse starts to converge toward one specific value.

To illustrate this behaviour, we show normalised stacks obtained using the 30
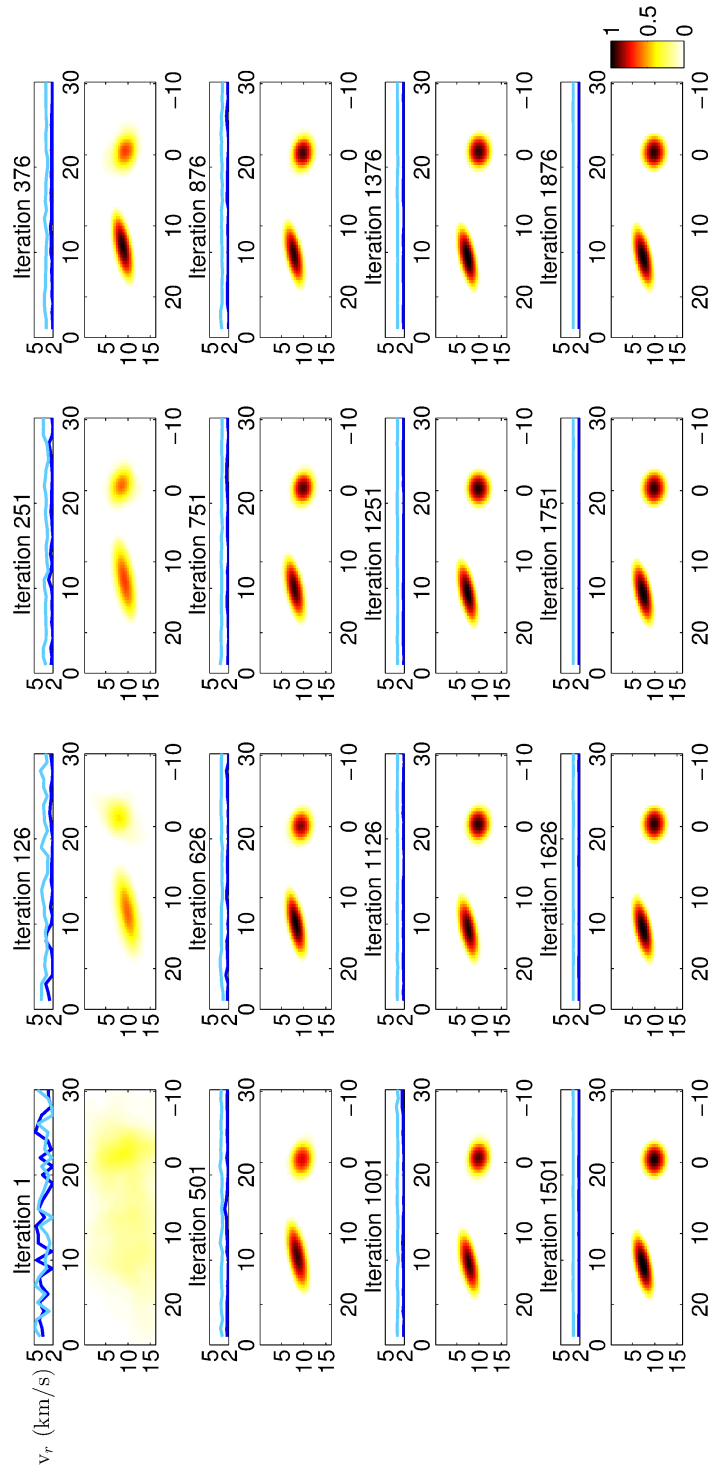
Figure 3.9: Normalised stack of the 30 slip distribution computed during one parallel iteration. At the top of each slip distribution, we show the variation of the rupture speed (km/s). The light curve shows the rupture speed of the first ellipse and the dark curve shows the rupture speed of the second ellipse.

slip distribution computed during one parallel iteration of the NA, and this for several iterations (Figure 3.9). On the top of each sub-plot, we show the rupture speed of each ellipse for each of the 30 rupture models. We clearly see that during the early stages of the inversion, the NA tests a wide range of models so the stack of slip distribution for Iteration 1 does not show any pattern. We also observe large variations of the rupture speed. At Iteration 126, the spatial position of the ellipses is clearly stabilised. However, we still observe variations in the rupture speed, although significantly less than before. From Iteration 126 to iteration 626, the range of rupture speed progressively narrows down toward the final value. At this stage (Iteration 626), the slip amplitude of each ellipse has not reached yet its final value. Around Iteration 751, the inversion has come close enough to the final model that we do not see much variation for the following iterations. At this point, the inversion could have been stopped without affecting the final conclusions of Chapter 2. However, we observe on the misfit curve (see Figure A2.5 in Appendices A2) that there is still significant variation on the value of the misfit at Iteration 751. Therefore, small variations on the inverted parameters can cause significant changes on the computed waveforms, illustrating the non-uniqueness associated to the kinematic inversions.

This investigation of the inversion procedure confirms that the NA, in combination with the elliptical sub-fault approximation, looks indeed for the most robust features of the source process. The position of the asperity and the rupture speed control the convergence of the inversion in order to get the right position in time for the different pulses. Once the space and time position of the different asperities are identified, the NA adjusts the slip amplitude. Consequently, the number of iterations has to be chosen according the aim of the study. If one studies the long term processes (e.g. discriminating between characteristic and complementary earthquakes), only a low number of iterations are necessary as the main aim is to get the size and the position of the main asperities. If one focuses on the conse-

quences of an earthquake, such as the intensity of the shaking, then more iterations are needed to constrain the slip amplitude and the rupture speed. Indeed, we have shown that small changes in the parameters could cause significant changes on the calculated waveforms, illustrating the non-uniqueness of kinematic inversions. For the latter reason, and because the inversion can be carried out rapidly due to the low number of parameters necessary to describe the slip history, the inversions presented in Chapter 2 were carried out using a large number of iterations.

3.5 Use of digital velocity versus digital displacement records

The use of ground displacement instead of ground velocity records can affect the inversion for the slip history of an earthquake. It is therefore important to assess the differences that may arise when one is used instead of the other. Few studies have compared the impact of this choice on the inferred rupture process. Shiba & Irikura (2005), using strong motion data of the 1997 Izu-Hanto Toho-Oki earthquake ($M_{jma}5.9$), show that the slip distribution inverted using velocity records is similar to that inverted using displacement records. The moment released in the rupture process obtained from velocity records however, is $\sim40\%$ smaller than that obtained from the inversion of displacement records. Hartzell et al. (2007), using the strong-motion data of the 2004 Parkfield earthquake ($M_w6.0$) reached a similar conclusion, however, in this study, the moment released is smaller in the rupture model obtained from displacement records than that obtained from velocity records. In Chapter 2, we recall that the original accelerograms were integrated twice into displacement records. We have decided therefore to investigate the response of our inversion scheme to the use of velocity records versus displacement records.

First, we take the 12 kinematic rupture models of Chapter 2 and calculate for each of them the 3-component velocity waveforms at each of the 10 stations. The

misfit associated to each rupture model is calculated (χ, calculated using Equation 3.1) and compared to the values obtained in Chapter 2 (ε). The results are summarised in Table 3.2 and show that the rupture model that has the lowest misfit value when velocity records are used is Inversion 8.

Inversion #	$\mathcal{E}$	χ
Inversion 1:	0.27	0.42
Inversion 2:	0.30	0.44
Inversion 3:	0.28	0.39
Inversion 4:	0.30	0.47
Inversion 5:	0.28	0.40
Inversion 6:	0.26	0.39
Inversion 7:	0.30	0.43
Inversion 8:	0.26	0.38
Inversion 9:	0.28	0.40
Inversion 10:	0.29	0.41
Inversion 11:	0.34	0.45
Inversion 12:	0.26	0.39

Table 3.2: Comparison between the misfit when we used displacement records or velocity records. $\mathcal{E}$ is the misfit value calculated using displacement records obtained in Chapter 2. χ is the misfit value calculated using velocity records.

The rupture model of Inversion 8 is very similar to the rupture model of Inversion 6, which is the preferred model of Chapter 2 (see Figure 2.3 in Chapter 2). The major difference between the two is that the values of the rise-time and the rake were fixed as a constant over the whole fault in Inversion 6 (0.5 s. and 180°, respectively), while in Inversion 8, those parameters were allowed to vary within each elliptical patch. In Inversion 8, 0.32 s. and 145.96° were obtained for the rise-time and the rake, respectively, while in the second ellipse, the rise-time and rake are 1.00 s. and 151.13°.

As for inversions using displacement records, the fit at each station shows that we fit very well the first pulse in time and amplitude. However, we still have a poor fit for the last part of the signal. This segment contains even more high frequency energy in the velocity records than in the displacement records, which explains why a systematic increase of the misfit value is observed when we use ground velocity

(see Figure A2.6 in Appendices A2 for the fit obtained at each station).

Next, we perform a inversion using velocity records. For each parameter, the NA searches within a range that is the same as the one used for Inversion 6 in Chapter 2. The inversion reaches a misfit value of 0.37, which is smaller than the values obtained for each of the 12 kinematic rupture models (Table 3.2). Figure 3.10 shows the rupture process associated with the lowest misfit value.
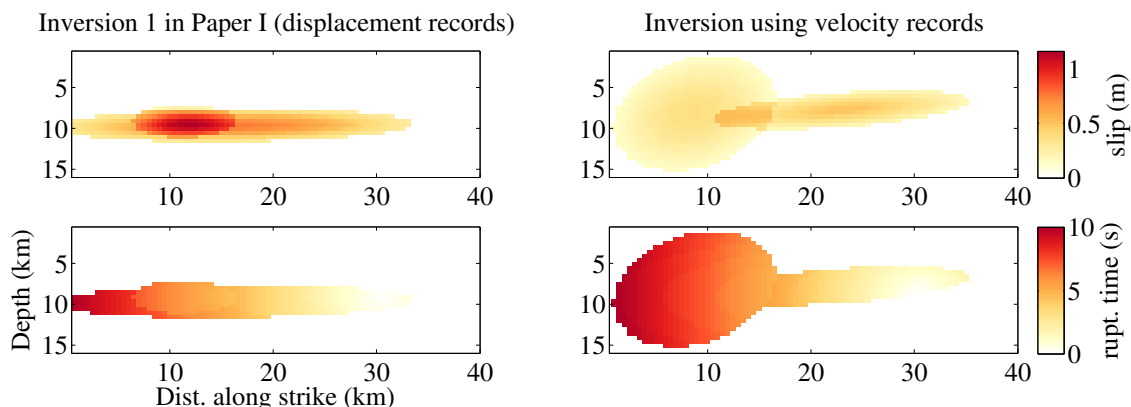
Figure 3.10: Top and bottom left figures show the final slip distribution and the isochrone for the rupture model obtained from Inversion 1 in Chapter 2, from using displacement records. Top and bottom right figures show the final slip distribution and isochrones for the rupture model obtained by inversion of velocity records.

The best fitting inversion using velocity records is very similar to the model obtained by Inversion 1 in Chapter 2. Unlike Inversion 1, however, we observe a significant spreading of the slip distribution at the end of the rupture process, but, this was also observed in Chapter 2 in some inversions (Inversion 11, 12). Thus, whether we use velocity waveforms or displacement waveforms, we reach similar conclusions, at least for the robust features of the rupture process. If we compare the fit to the waveforms obtained from the inversion (Figure 3.11) with the fit to the waveforms when we use one of the kinematic rupture model (Figure A2.6 in Appendices A2), we have a clear improvement of the fit on the vertical component while other components show a similar fit.

The results of this experiment show that our inversion scheme leads to similar rupture process, whether we use velocity or displacement records. The main dif-
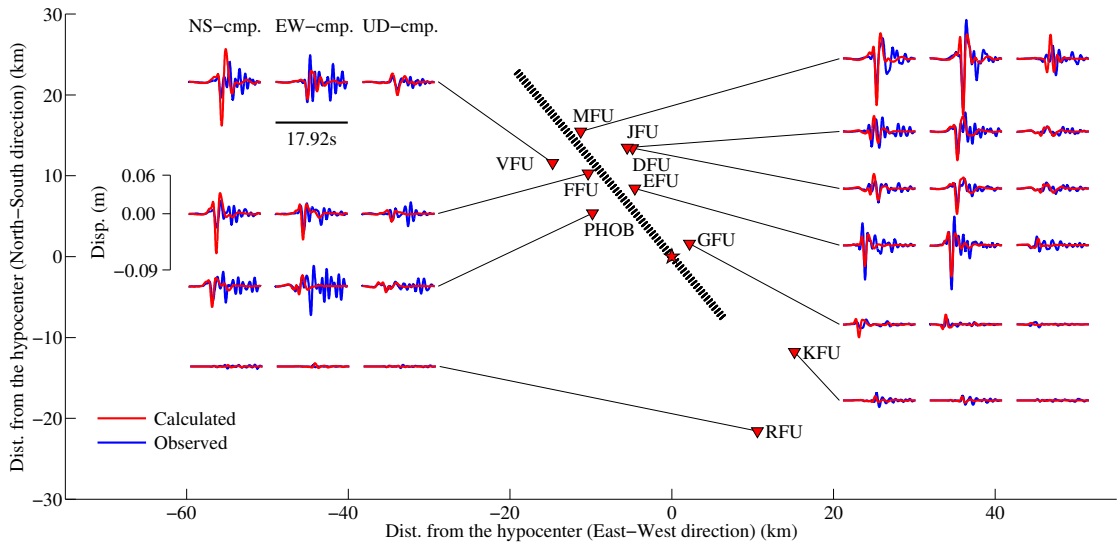
Figure 3.11: Comparison between the calculated waveforms (red line) and the observed waveforms (blue line) for the 10 digital stations.

ference between the two is the frequency content, which shows that the inversion is constrained predominantly by the low frequency energy and that the addition of higher frequency energy does not affect the results. This conclusion is similar to those of Shiba & Irikura 2005 and Hartzell et al. (2007). Like Hartzell et al. (2007), we obtain a final seismic moment in the rupture process obtained from velocity records that is higher than that obtained using displacement records (1.8×10^{18} Nm instead of 1.2×10^{18} Nm). However, Shiba & Irikura (2005) reach an opposite conclusion and, because only few examples are available, it is not possible to tell if this is a systematic behaviour and further investigation is necessary to assess this issue.

3.6 Influence of the Frequency Band used during the Inversion

An important aspect of the data processing is the choice of the frequency band that is used to process the observed records we attempt to invert. Indeed, the frequency content of the seismograms affects directly the waveforms and therefore the content

of information that is available during the inversion. Mendoza & Hartzell (1988) investigated this issue by performing two inversions for each of the three earthquakes that they have studied using teleseismic P waveforms. One inversion uses long period P-waves and one inversion uses long and short period P-waves. Their results show a more detailed rupture process for inversion at high frequency than for inversion at low frequency. They also encountered difficulty to invert wavelengths between 1 and 2 s. Three hypothesis were suggested to explain this issue. First, it may relate to the parameterization used during the inversion. It may also reflect some complexities in the rupture process that cannot be resolved by the inversion. Finally, as suggested in Chapter 2, it could be due to propagation effects that are not accounted. The impact of this aspect of the data processing has also been considered by Ide (1999). Inversions for the earthquake source process of the 1997 Yamaguchi, Japan, earthquake were carried out in two separate frequency bands, one low-frequency band (0.1 - 0.5 Hz) and one high frequency band (0.5 - 2.0 Hz). The results show that the rupture models obtained using high-frequency records release the moment at the edges of the slip patches obtained using low-frequency records.

In Chapter 2, we recall that the original accelerograms are integrated twice into displacement records and are then filtered using a 4th order Butterworth band-pass filter in the frequency band (0.16 - 1.00 Hz). If we look at the comparison between the observed and the calculated spectra for the preferred model of Chapter 2 (Figure 3.12), we observe that for the low frequency part (<0.5 Hz), the fit between the observed and calculated spectra is good, but above 0.5 Hz, we clearly observe a deterioration of the fit. To measure the quality of the fit, we use a simple $\mathcal{L}^2$ criteria on the absolute value of the spectral amplitudes:

$$\mathcal{L}^2 = \frac{\sum (obs - synth)^2}{\sum (obs)^2} \qquad (3.2)$$

In the frequency band 0.16-1.00 Hz, we obtain a misfit value of 0.25. Calculated
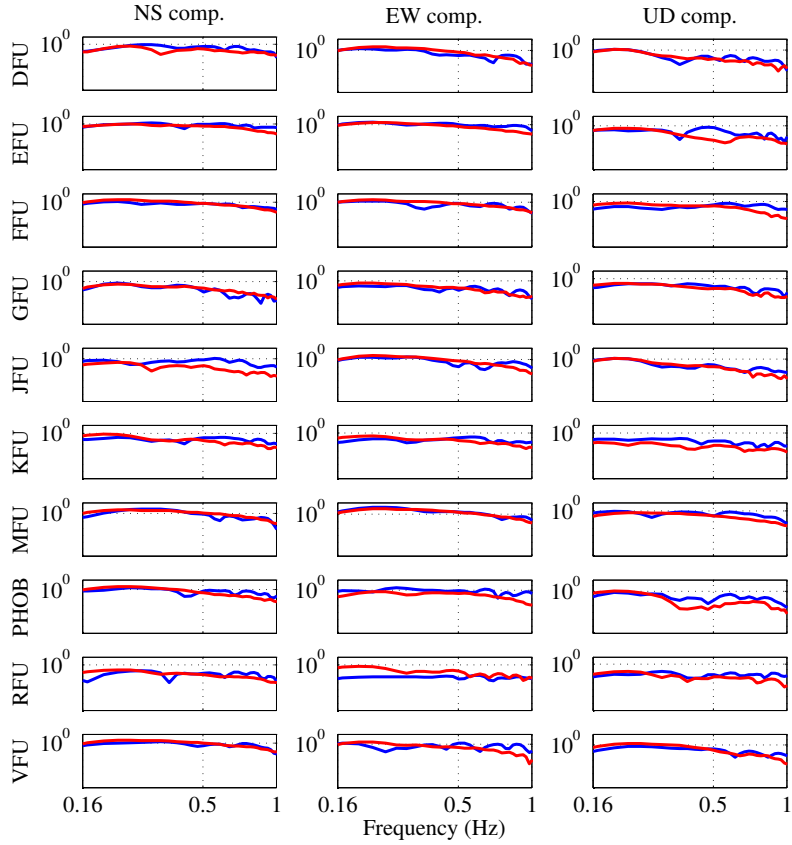
Figure 3.12: Comparison between the spectral displacement (m) for the calculated waveforms (red line) and the observed waveforms (blue line) for the 10 digital stations, named on the left side of the figure, in the frequency range (0.16-1.00 Hz)

in the band 0.16-0.50 Hz, we have a value of 0.20 and in the band 0.50-1.00 Hz we obtain a value of 0.35. It clearly shows, as expected, that we have a better fit in the low frequency range than at high frequencies.

To investigate the impact of the addition of high frequencies in the displacement waveforms on the results of an inversion, we performed one inversion in which the data were filtered between 0.16 and 0.50 Hz. The search of the optimal solution by the NA is carried out within the same ranges for each parameter as those used for Inversion 6 in Chapter 2.

Figure 3.13 shows the rupture process of the inverted model compared with the rupture process obtained by Inversion 6 in Chapter 2. We observe that we the two rupture models are very similar. The size of the ellipses in the low frequency inversion have increased but the slip amplitude of each ellipse has decreased, so that

the moment of this model (1.4×10^{18} Nm) is similar to the moment of the high frequency model (1.2×10^{18} Nm). The similarity between the two, suggest that the elliptical sub-fault approximation tends to fit preferentially the lower frequency part of the signal and is therefore well suited when the aim objective to resolve the most robust features of an earthquake.
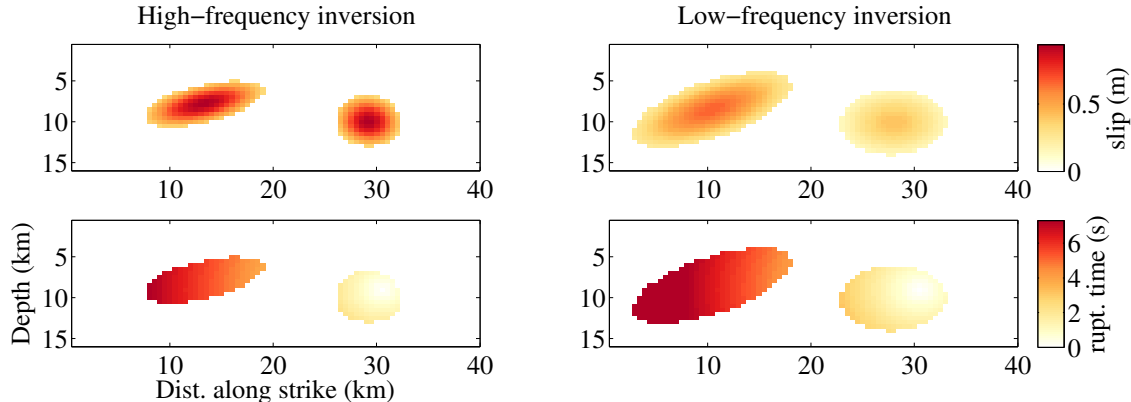
Figure 3.13: The top and bottom left figures show the final slip distribution and the isochrones of the rupture model obtained by Inversion 6 (i.e. the preferred rupture model of Chapter 2), which is obtained using displacement records filtered between 0.16 and 1.00 Hz. The top and bottom right figures show the final slip distribution and the isochrones of the rupture model obtained by inversion of displacement records filtered between 0.16 and 0.50 Hz.

Figure A2.7 in Appendices A2 shows the fit to the waveforms. The value of the misfit ($\mathcal{E} = 0.21$; calculated using Equation 3.1), is significantly lower than the misfit obtained when waveforms containing higher frequencies are inverted. We also compare the observed and the calculated spectra in the frequency band of interest (Figure A2.8 in Appendices A2). The misfit value calculated using Equation 3.2 is 0.18 which is slightly lower than the initial value of 0.20. The rupture process in Figure A2.7 shows that in the low frequency band, we fit the last part of the signal at most stations. As argued in Chapter 2, this last part may not represent source processes from the earthquake because when we remove the high frequency signal, we still obtain the same slip distribution and rupture process. As argued by Mendoza & Hartzell (1988), this could be caused by our parameterization used during the inversion. As shown with the synthetics tests, the elliptical sub-fault approximation

acts as a low-frequency filter, which explains the low sensitivity to high-frequency signals. Both explanations still support the conclusions that our inversion scheme is well suited to extract the robust features of earthquake source processes.

3.7   Information Content

In order to perform an inversion of the rupture process, we have to define the seismograms duration that is used during the inversion (i.e. what is the duration of the seismograms for which the misfit value is calculated). This choice is very important because it controls the amount of information on the source process that is given to the algorithm. We investigate this issue by performing a series of inversions in which the cost function uses a portion of the seismograms of a certain duration that is progressively increased up to the duration that was used in Chapter 2 (i.e. 17.92 s). In Equation 3.1, t_b is 0 and t_e varies for each inversion. The results are summarised by Figure 3.14.
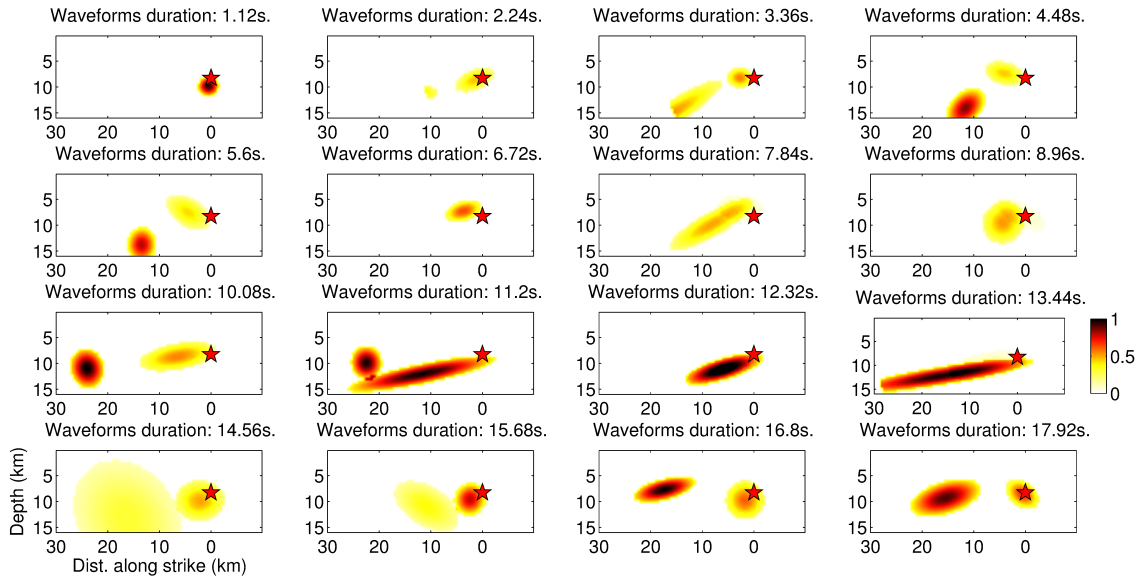
Figure 3.14: Final slip distribution (m.) obtained for the inversion of seismograms of different duration (shown on top of each slip distribution). The duration of 17.92 s was used to obtain the 12 kinematic inversions presented in Chapter 2. The star shows the position of the hypocenter.

We can see that changes in the duration of the seismograms have significant

49

impacts on the final rupture history, even though all models are still within the range of plausible models shown in Chapter 2. In most of the inversions, the hypocentral ellipse is retrieved, which support the conclusion that this is a robust feature of the source process. The slip patch away from the hypocenter starts to be a recurrent feature only when we invert seismograms longer than 9 s. It is interesting to note that this second patch gets progressively shallower when the duration of seismograms gets longer. Zhou et al. (2004) have observed a similar behaviour in their synthetic tests, using the September 1999, $M_w7.3$ Chi-Chi, Taiwan, earthquake. They suggested that with shorter waveforms, the data has less information on deeper sub-faults and therefore the slip on those sub-faults are less well constrained and consequently less reliable.

Figure 3.15 shows the evolution of the misfit values against the duration of the seismograms used in each inversion. We observe that the misfit values defines two different groups. Comprising the first 7 inversions, we observe a group where the misfit value is around 0.10. For inversions using longer seismograms, the misfit value starts to increase to its final value around 0.26. Between these groups, 3 models occupy the transition from the low misfit stage to the high misfit stage. It is interesting to note that the first tipping point is observed when seismograms longer than ~ 9 s are inverted, which is also the minimum duration needed for the significant slip away from the hypocenter to become recurrent.

In order to compare the relative content of information about the rupture process that has reached each station for each inversion, we calculate the theoretical arrival-time of the first and last P-wave, as well as the last Rayleigh wave, using the velocity structure used in Chapter 2. The calculations are made using the rupture history of the inversion that used the 17.92 s long seismograms. These results are summarised in Figure 3.16.

First, we observe that the first P-wave emitted from the hypocenter reaches the closest station (GFU) after ~ 2 s. Thus, the model obtained when we use waveforms
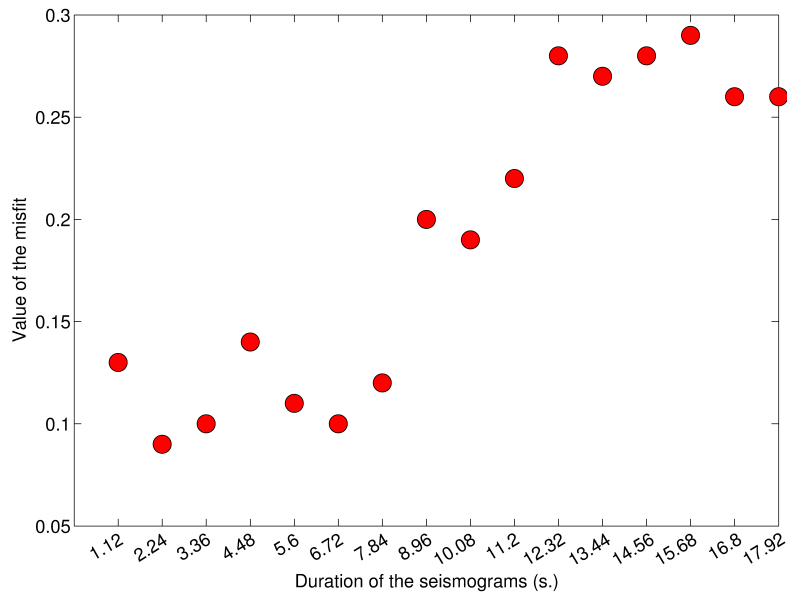
Figure 3.15: Evolution of the misfit value with the duration of the seismograms used for the inversion.
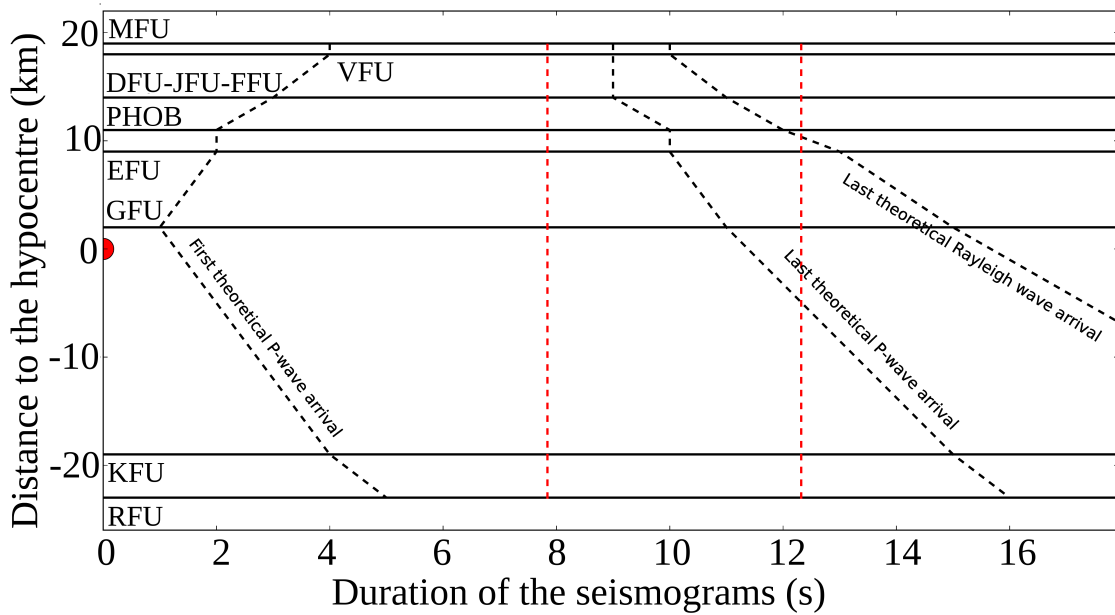
Figure 3.16: Theoretical arrival time for the first and last P-waves generated from the rupture history of the preferred model in Chapter 2 (black dashed lines). Each station is shown according its distance from the epicentre. The vertical dashed lines correspond to the two tipping points seen in Figure 3.15.

of 1.12 s long (see Figure 3.14) is a complete artefact because nothing about the rupture process has reached any of the stations. The first tipping point observed in Figure 3.15 (vertical dashed line at 7.84 s in Figure 3.16) occurs when the duration

of the waveforms are long enough that P-waves emitting from the last part of the rupture process begin to reach each station. The second tipping point observed in Figure 3.15 (vertical dashed line at 12.32 s in Figure 3.16) roughly occurs when the Rayleigh waves coming from the end of the rupture process have reached most of the stations. For waveforms longer than ~ 16 s, the inversion produced a similar rupture model (see Figure 3.14), and it corresponds to a duration when all stations, excepted the two further stations located at the south-east end (KFU and RFU), have received Rayleigh waves coming from the end of the rupture process.

The duration of the seismograms is therefore an *a-priori* choice that can significantly affect the inferred rupture process. We note however that the models obtained for each inversion are still within the range of plausible models when compared to the results shown in Chapter 2. The response of our inversion procedure to the constraint on waveforms duration occurs in three stages. First, a stage with rupture models that have low misfit value, when the duration of the seismograms is significantly shorter than the expected rupture process. Then, a final stage with rupture models that have a misfit value close to the misfit value obtained for the preferred model of Chapter 2, when the duration of the seismograms is long enough that most stations have received signal from the end of the rupture process. In between, there is a transition of the misfit value from the low misfit value stage to the high misfit value stage that corresponds to the progressive arrival of information from the last part of the rupture process at each station. These results suggest that it is important to ensure that waves coming from the end of the rupture process are present in the seismograms in order to get a more reliable rupture process from the inversion. This was also pointed out by Mendoza & Hartzell (1988) in their study of the North Palm Springs, Borah Peak and Michoacan earthquakes.

3.8   Conclusions

We have performed here a series of tests in order to assess the stability of our kinematic inversion procedure.

We first subjected our kinematic inversion to synthetic tests with the aim to obtain the rupture source process from synthetic data generated by artificially created earthquakes. For a k^{-2}-type slip distribution, used simulate earthquakes, the results from our inversions show that the elliptical sub-fault approximation tends to focus on the robust features of the artificial slip distribution. The inversions resolved a low-frequency filtered version of the input rupture models. The number of ellipses can be determined by progressively increasing the number of them until one obtains a good fit to the data.

We have also analysed the behaviour of the NA in its search of the optimal solution. We have shown that the space-time position of the rupture front controls the convergence of the NA and that only later in the process is the slip amplitude adjusted. The number of iterations used in an inversion should be dictated by the aims of the study. The final positions of the ellipses is found by the algorithm after a small number of iterations, however, a large number of iterations is needed to constrain the slip amplitude and the rupture velocity.

Tests on using velocity records instead of displacement records shows that both dataset lead to compatible results. However, we observe that the final moment found when we invert velocity records is higher than the final moment found when we invert displacement records. Therefore, the use of one instead of the other should not affect significantly the inferred rupture history. The same is also observed when the frequency range of the seismograms was modified. It shows therefore that the inversion is not very sensitive to high-frequency signals, which is why the inversion scheme is better suited to obtain the large scale robust features of an earthquake rupture history.

Finally, we have tested the influence of the duration of the seismograms on the

final results. We found that the inversion is very sensitive to the duration of the seismograms. This is because it relates to how much information on the source process is given to the algorithm.

Chapter 4

Dynamic Inversion for the Rupture Process of the 2004, Parkfield, California, Earthquake.

4.1 Introduction

In order to study the physics of the earthquake rupture process, the key is to unravel the space-time behaviour of the rupture from records at the surface. One way to carry this out is to create a slip model from which the radiated seismic waves produce ground motions that are similar to surface observations. A slip model is simply a space-time description of the rupture (i.e. the amplitude of slip and the time of the rupture at different points along the fault). These kinematic models, however, do not explicitly describe the rupture based on its physics. Instead the physics is only there from *a-priori* assumptions on the behaviour of the slip models. On the other hand, dynamic modelling provides a dynamically correct description of the rupture, based on fracture mechanics, although it relies upon a description of the stress condition on the fault plane prior to the earthquake rupture.

The normal approach to create a dynamic model is to perform first a kinematic inversion. The stress conditions and frictional parameters are then calculated on the fault from the kinematic slip model. Then, the propagation of the rupture is modelled and is essentially controlled by the inferred stress and friction (e.g. Quin

1990 with the 1979 Imperial Valley earthquake; Fukuyama & Mikumo 1993 with the 1990 Izu-Oshima earthquake; Olsen et al. 1997 for the 1992 Landers earthquake; Oglesby et al. 2004 for the 2002 Denali earthquake). However, recent studies have shown that it is possible to invert directly for the stress and strength distribution on the fault plane (Peyrat & Olsen 2004, Di Carli et al. 2010 and Ruiz & Madariaga 2011, 2013).

Also, the recent study of Konca et al. (2013) has emphasised again that kinematic inversion is capable of providing a realistic image of the dynamic rupture process, despite the fact that it is not based on a physical formulation of the problem of rupture propagation. To assess the uncertainties and reduce the non-uniqueness associated with this method, it is important to obtain a kinematic rupture model that is dynamically correct. One way to obtain such a rupture model is to combine the kinematic and the dynamic approaches as proposed by Fukuyama & Mikumo (1993). Indeed, because the kinematic inversion is suited to infer the robust features of the rupture process, we can use it to constrain the geometry of the rupture area prior to a dynamic inversion. The latter can thus be fixed from the results of the kinematic inversion, and the dynamic inversion is performed only in order to obtain the stress conditions along the fault. This approach has the advantages of reducing the degree-of-freedom for the dynamic inversion as well as ensuring a dynamically realistic rupture model.

In this study, we first perform a full dynamic inversion for the rupture process of the 2004, $M_w6.0$, Parkfield, California, earthquake. To assess the issue of non-uniqueness associated with dynamic inversions (e.g. discussion by Peyrat et al. 2001), we explore the parameter-space using a Monte-Carlo method, fixing the geometry of the rupture area from the results of the dynamic inversion. The same approach was used to investigate one of the kinematic rupture model of Twardzik et al. (2012). The aim is to see if we can find stress conditions on the fault that can make this model dynamically correct. This is combined with a new way to describe

the rupture area that use the advantageous flexibility of the b-spline curve.

4.2   Dataset

In order to determine the dynamic rupture process of the September 2004 Parkfield, California, earthquake, we use 3-component waveforms of 17.92 s long, sampled at 3.5×10^{-2}s, recorded by 10 digital stations from the GEOS network (Borcherdt et al. 1985). The acceleration records are integrated twice into displacement. They are band-pass filtered between 0.16 and 1.00 Hz using a 4th-order Butter-worth filter (see Figure 4.1). The filter is applied both forward and backwards to obtain zero phase shift for all frequencies.
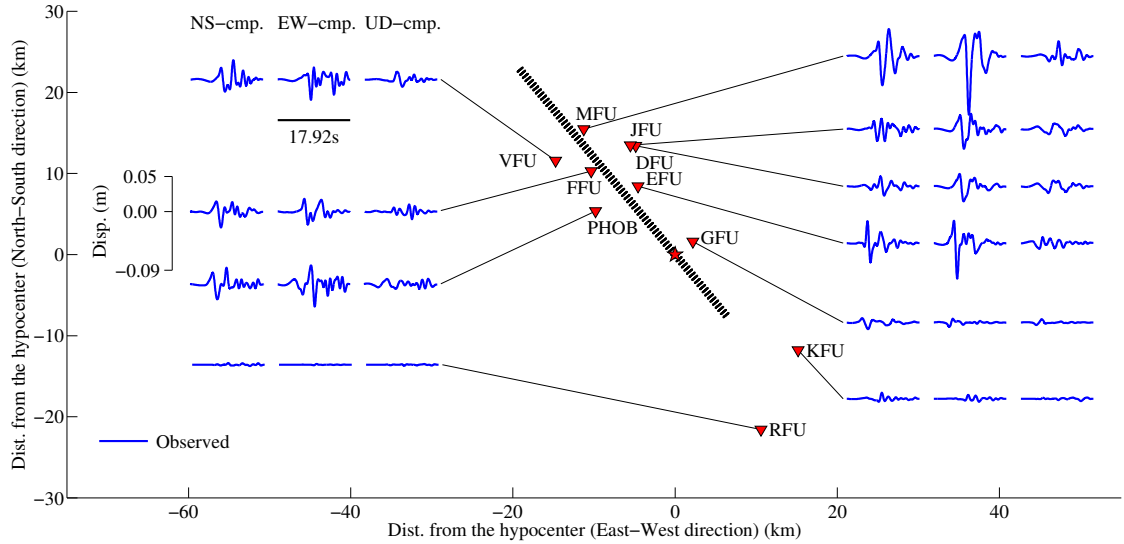
Figure 4.1: Map of the station distribution. The 3-component displacement records from the 10 digital stations of the GEOS network used to perform the dynamic inversion are shown by the blue trace. The red star shows the location of the epicentre and the black dashes show a surface projection of the fault plane.

Despite the fact that 33 analog stations from the CGS network have also recorded this earthquake (Shakal et al. 2006), we only use the 10 digital stations to ensure the systematic presence of P-waves on each trace. The dataset is consequently identical to that used by Twardzik et al. (2012) for kinematic inversions, which allows

a straightforward comparison between the results from dynamic and kinematic inversions.

4.3　Inversion Procedure

The inversion is carried out using the Neighbourhood Algorithm (NA) developed by Sambridge (1999a,b). It performs a direct search of the optimal solution of the parameter space using Voronoi cells. For each iteration, the algorithm divides the parameter space into a set of n_s Voronoi cells, one for each model of which we calculate the waveforms. Geometrically, one Voronoi cell is a polyhedron that encloses a region of the parameter space containing models that produces waveforms that similarly fit the data. The fit is measured through the following cost function proposed by Spudich & Miller (1990):

$$\mathcal{E} = \sum_{i=1}^{N_d} W_i \left(\left(\frac{\sum_{tb}^{te}(u_i^o(t) - u_i^s(t))^2}{\sum_{tb}^{te}(u_i^o(t))^2 + \sum_{tb}^{te}(u_i^s(t))^2} \right) \right). \tag{4.1}$$

The cost function is the same as what we have used in the previous chapters to allow a direct comparison between the results obtained by kinematic inversions and those obtained by the dynamic inversions. In this equation, $u_i^o(t)$ are the observed waveforms and $u_i^s(t)$ are the calculated waveforms. W_i refers to the weight given to each component, with values chosen as in Liu et al. (2008). N_d is the number of records and (t_b, t_e) gives the beginning and end times of the displacement records. This cost function is the same as the one used in Twardzik et al. (2012) to allow a direct comparison between the results from kinematic and dynamic inversion. Once an iteration is done, a new set of n_s models is re-sampled for the next iteration within the Voronoi cells that contain the n_r lowest misfit models. In this study, n_s is set to 32 and n_r to 8.

4.4 Forward Modelling

The forward modelling consists of a full spontaneous rupture propagation in a 3-D medium on a pure right-lateral strike-slip fault that has a strike of 140°N and a dip of 87°. Rupture propagation is solved using a 4th-order staggered-grid finite-difference method (Madariaga et al. 1998).

For the finite-difference, we use a grid size (Δx) of 250 m to discretize the fault plane that is 40 km long and 16 km deep. Each simulation, which uses a time-step (Δt) of 8.75×10^{-3}s, which is 1/4 of the sampling rate of the displacement records, is run for 1280 steps (i.e. equivalent to 11.2 s). The velocity structure used is the 1-D velocity structure of the north-east side of the San Andreas Fault from Liu et al. (2006), itself determined by interpolation of the 3-D velocity model of Thurber et al. (2003). This process resolves all variables to measure the stability of the finite-difference scheme by means of the Courant-Friedrichs-Lewy criterion (C.F.L. criterion):

$$C.F.L. = V p_{max} \frac{\Delta t}{\Delta x} \tag{4.2}$$

In our case, its value is 0.217, which ensures the stability of the numerical scheme (Madariaga et al. 1998).

The fault plane is treated as an internal boundary, on which we postulate that the rupture propagation is controlled by the slip-weakening friction law of Ida (1972):

$$
\begin{aligned}
T_f(D) &= (T_u - T_r)(1 - \tfrac{D}{D_c}) + T_r &&\text{for } 0 < D < D_c \ , \\
T_f(D) &= T_r &&\text{for } D \geq D_c \ .
\end{aligned}
\tag{4.3}
$$

T_f is the friction as a function of slip (D), T_u is the upper yield stress and T_r is the residual stress. Because T_r cannot be determined from seismic observations alone (Madariaga 1979), we set it to 0. D_c is the slip-weakening distance, and is the amount of slip at the crack tip that is necessary to monotonically decrease the shear stress from the static frictional strength (T_u) to the dynamic frictional strength (T_r).

The finite-difference scheme also includes a flat free-surface boundary condition at the top and a Clayton-Engquist absorbing boundary condition at the edges (Clayton & Engquist 1977).

The background stress (T_e), or tectonic stress, is assumed constant over the whole fault plane. The rupture area is then defined using elliptical patches derived from the approach initially suggested by Vallée & Bouchon (2004). The geometry of an elliptical patch is described by the position of its centre on the fault plane (x_o,y_o), the length of its semi-major (a) and semi-minor (b) axes and the dip of the semi-major axis relative to the free-surface (ϕ). During the dynamic inversions carried out in this study, we use two ellipses to define the rupture area, chosen according to the results of Twardzik et al. (2012). We assume that the upper yield stress inside each patch follows an elliptical distribution:

$$T_u(x, y) = T_{umax} \left(1 - (\frac{x^2}{a^2} + \frac{y^2}{b^2}) \right), \tag{4.4}$$

where T_{umax} is the maximum upper yield stress located at the centre of the ellipse. It aims to mimic the concept introduced by Das & Kostrov (1983) in which the edge of a patch is weaker than its centre. Finally, in order to trigger the rupture, we use a small patch of radius (R_{asp}) and stress (T_{asp}), located at the hypocenter.

The description of the geometry of the rupture area requires 10 parameters to be determined (5 for each ellipse). The stress conditions on the fault plane are described using 2 values for the maximum upper yield stress (one for each ellipse), one value for the tectonic stress, the radius and stress of the triggering asperity and the slip-weakening distance of the friction law. This leads to a total of 16 parameters to be inverted for (see Figure 4.2).

To avoid sampling non-realistic models by the NA-algorithm, we invert for the parameter S instead of T_{umax}. S represents the ratio between the strength of the elliptical patch and the tectonic stress and was introduced by Andrews (1976) and
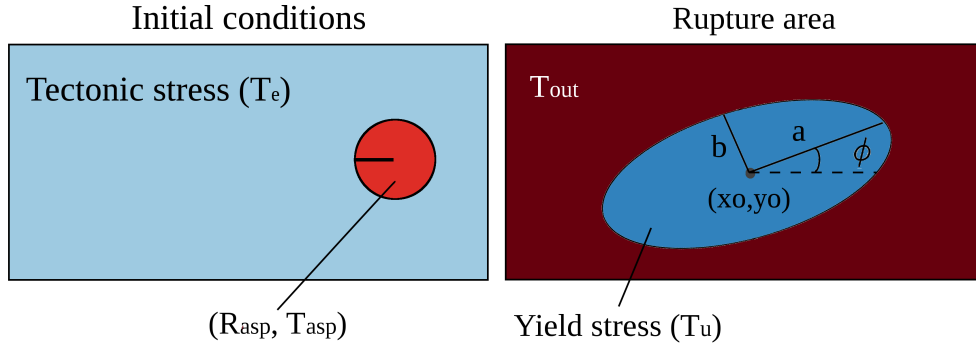
Figure 4.2: (left): Initial conditions before the spontaneous rupture propagation. (right): Rupture area in the case of one ellipse. Each parameter used during the inversion is schematically represented.

Das & Aki (1977a). It is defined by the following expression:

$$
\begin{aligned}
S &= (T_u - T_e)/T_e \quad \text{which can be rewritten as:} \\
T_u &= (1 + S)T_e.
\end{aligned}
\tag{4.5}
$$

Because we force S>0 during the inversion, it guarantees that the distribution of T_u inside one ellipse is always greater than or equal to T_e. For the same reason, to make sure that T_{asp} is always above the upper yield stress and thus ensure that the rupture is ready to propagate in all cases, we invert for a factor α, which is defined as:

$$
T_{asp} = \alpha T_{umax}.
\tag{4.6}
$$

Ruiz & Madariaga (2011), using strong motion data of the 2007, $M_w6.7$, Michilla, Chile, earthquake demonstrated that dynamic inversion of seismic data alone cannot distinguish between the asperity model (Kanamori & Stewart 1978) and the barrier model (Das & Aki 1977b). We have therefore arbitrarily adopted a barrier model during the inversions (i.e. the yield stress outside the rupture area (T_{out}) is assumed to be positive and very large so that the rupture stops propagating because the friction becomes too large to overcome). In our inversion, T_{out} is set to be 10 times the largest value of T_{umax}.

The AXITRA algorithm developed by Cotton & Coutant (1997) is used to cal-

culate the Green's functions. It combines the discrete wavenumber decomposition of Bouchon (1981) and the reflectivity method of Kennett & Kerry (1979).

4.5 Rupture History of the Parkfield Earthquake from Dynamic Inversion

In order to test our dynamic inversion method, we have performed two synthetic tests presented in Appendix A3. They show that it is possible to retrieve a reliable rupture history from artificial "noise-free" displacement records, but they also show that solutions are non-unique. With that in mind, we carry out a full dynamic inversion (i.e. the geometry of the rupture zone and the stress conditions on the fault) for the rupture process of the Parkfield, California, earthquake of September 28, 2004. Using the elliptical sub-fault approximation, we aim to obtain the robust features of the rupture process, whilst ensuring that it is dynamically correct.

The inversion of the 3-component displacement seismograms reaches a misfit value of 0.29, which is within the same range of the misfits obtained by Twardzik et al. (2012) by kinematic inversion. The comparison between the calculated and the observed waveforms (Figure 4.3) shows that the main pulses are fitted in amplitude and phase for almost every trace. However, we do not fit well the later part of the signal. As previously argued, it is likely that this portion of the waveforms is affected by waves from the fault zone. Because we do not attempt to model these kind of waves, this could explain the mismatch with observation for this part of the signal.

We also observe a better fit for stations located on the north-east side of the fault compared to those on the south-west side. This is because there is a strong contrast in the velocity structure between the two sides of the San Andreas Fault at the Parkfield area (Thurber et al. 2006). The current version of the finite-difference scheme only works for a 1-D velocity structure and because more stations (6 out of
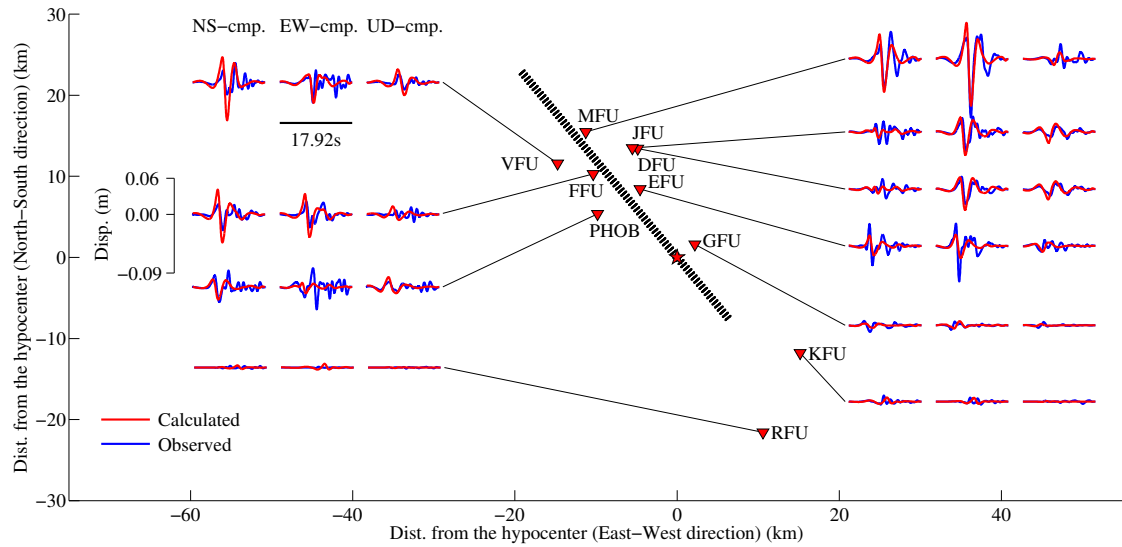
Figure 4.3: Comparison between the observed displacements of the 2004 Parkfield earthquake (blue traces) and the calculated displacements from the lowest misfit model obtained by the non-linear full-dynamic inversion (red traces).

10) are located on the north-east side of the fault, we have chosen to use the velocity structure associated with the north-east side of the fault.

The initial distribution of stresses and the distribution of slip and the rupture isochrones for the lowest misfit model obtained by the dynamic inversion are shown on Figure 4.4. The rupture essentially breaks one major ellipse elongated in the strike direction. There is also a second ellipse with smaller slip amplitude close to the hypocenter. The final seismic moment of the rupture model is 1.18×10^{18} Nm, which is $\sim 4\%$ larger than the CMT value. The average rupture speed, calculated from the time needed for the rupture to reach the north-eastern end of the fault plane, is approximately 2.80 km/s.

From snapshots of the slip-rate (see Figure A3.7 in Appendix A3), we observe that the rupture is finished after 7.75 s, clearly below the 11.2 s that we are using for the simulations. We also observe that the rupture of the hypocentral ellipse is faster than that of the main ellipse (about 3.8 km/s, which is 10% higher than the shear-wave speed at that depth). It is also important to note that the entire process does not exhibit much variation in rupture speed so that the rupture occurs at more

Initial distribution of stresses obtained from inversion:
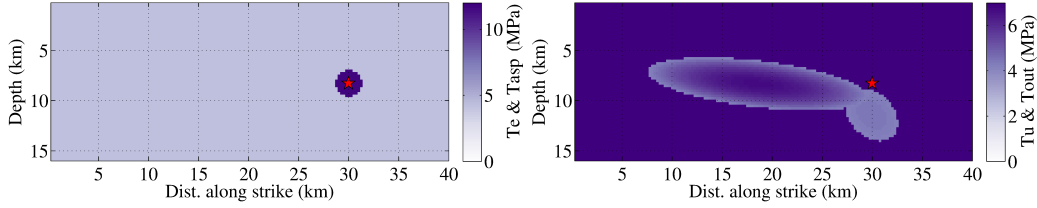
Rupture process obtained from inversion:
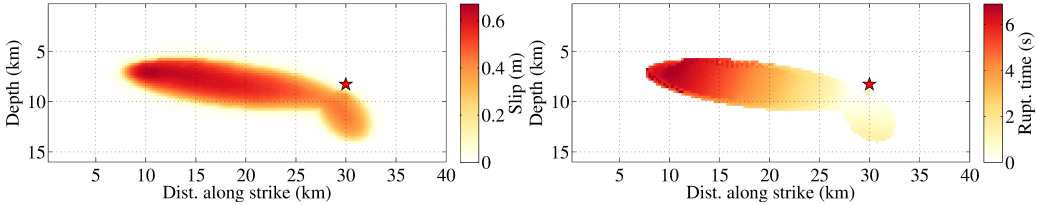
Figure 4.4: (top-left): Initial stress conditions prior to the propagation of the rupture. The whole fault is under tectonic stress and the initial asperity needed to trigger the rupture is located at the hypocenter. (top-right): Rupture area defined by spatial variation of the upper yield stress. (bottom-left): Final slip distribution. (bottom-right): Distribution of the rupture isochrones. In all figures the star represents the location of the hypocenter.

or less constant speed within each ellipse.

It is interesting to note that this rupture history is similar to the rupture model obtained from Kinematic Inversion 1 of Twardzik et al. (2012) and when we compare the calculated waveforms from the kinematic rupture model and those from the dynamic rupture model, there is almost no difference (see Figure A3.8 in Appendix A3). Using the waveforms of the 2004 Parkfield earthquake, we have therefore reached independently two similar rupture processes, one from kinematic inversion, the other from dynamic inversion,with the two producing almost identical ground displacements.

4.6 Investigation of the Dynamic Parameter Space

To assess the conditions under which a model can reasonably fit the observed waveforms, we show the Marginal Probability Density Function (M-PDF) for the 6 dynamic parameters obtained by the inversion (see Figure 4.5).

64
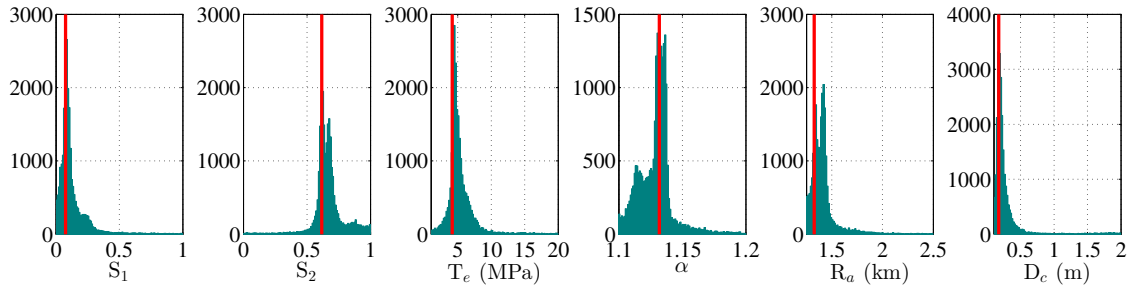
Figure 4.5: M-PDF for the 6 dynamic parameters used during the dynamic inversion. The red line shows the value towards which the NA-algorithm converged.

One of the features of the rupture model is that the two ellipses have different strengths. The small ellipse at the hypocenter is "weak" (S_1 ~0.08 or T_{u1} ~4.5 MPa), while the major ellipse has a larger value of S (S_2 ~0.7 or T_{u2} ~6.8 MPa) and is therefore relatively "strong". The difference between the two is manifested by the different rupture speed observed for each ellipse. As already mentioned, the main asperity has a rupture speed of 2.8 km/s, whereas, the small hypocentral asperity ruptures much faster (at about 3.8 km/s).

In terms of stress-drop (T_e), the NA-algorithm converges towards a value of 4.2 MPa. When compared to the values obtained from forward dynamic modelling of the 2004 Parkfield earthquake performed by Ma et al. (2008), we get an average value of their stress-drop model. Indeed they have the hypocentral area that has a stress drop of ~10 MPa, while the remaining part of the fault plane has a stress-drop of ~2 MPa.

The slip-weakening distance for the lowest misfit model is 0.17 m. This value is in agreement with the one used by Ma et al. (2008) for their dynamic modelling of the Parkfield earthquake (0.15 m). The calculated energy release rate for the hypocentral ellipse is 3.8×10^5 Jm^{-2} and that for the main ellipse is 5.8×10^5 Jm^{-2}. Once again, it is in good agreement with the dynamic modelling of Ma et al. (2008). It is also in agreement with the data from laboratory experiments and the compilation of seismological estimates of Nielsen et al. (2013).

Figure 4.6 shows stress as a function of slip at each time step, taken at different

points on the fault plane, which gives the resolution on the friction law at each of these locations. We can see that it is not uniform. It is very well resolved near the hypocenter (point 1 to 3) but less well resolved as we progress inside the ellipse (point 4 to 9). It then regains resolution near the tip of the ellipse (point 10). However, we see that even in the worst case (point 8), we have 3 points to resolve the friction law. These differences in resolution can be explained by the decrease of the cohesive zone as the crack grows (Andrews 1976). A better resolution of the cohesive zone can be achieved by using a finer spatial and temporal grid size (see for instance the recent study of Bizarri & Das 2012), but the increase of the computational resources necessary to do that, makes this beyond the scope of this study.
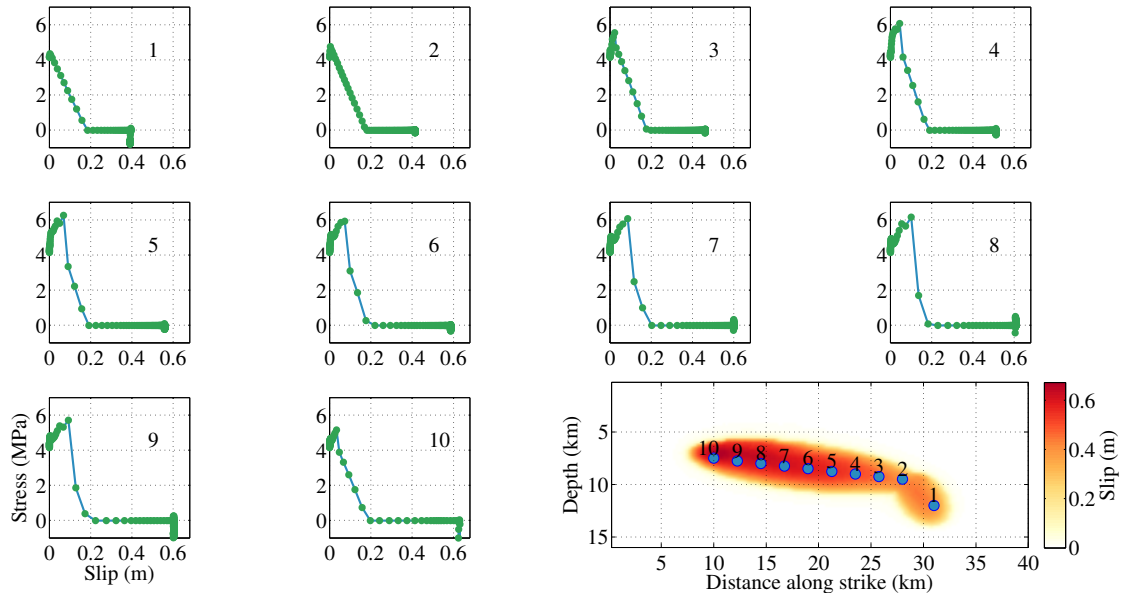
Figure 4.6: Slip-weakening friction law taken at different locations on the fault plane. The location of all the points are shown on the slip distribution on the bottom-right corner of the figure.

We also compute the value of κ for each ellipse. κ is a non-dimensional parameter introduced by Madariaga & Olsen (2000). It expresses the ratio between the available strain energy and the energy release rate:

$$\kappa = (T_e^2 L)/(\mu T_u D_c), \tag{4.7}$$

where μ is the average shear modulus of the medium, L a characteristic length that we take as the length of the semi-minor axis of the ellipse and all others parameters have been described earlier. As explained by Madariaga & Olsen (2000), this parameter controls the characteristics of the rupture process. It defines a bifurcation at a critical value (κ_c). If $\kappa < \kappa_c$, the rupture does not grow outside the initial asperity and if $\kappa > \kappa_c$, the rupture propagates at increasing speed with κ. Madariaga et al. (1998) estimated κ_c to be about 0.6 for a 2D circular crack.

In this study, we obtain $\kappa_1 \sim 1.96$ for the hypocentral ellipse and $\kappa_2 \sim 1.40$ for the major ellipse. The value of κ_2 is very similar to the values obtained by others (e.g. 1.35-1.45 found by Ruiz & Madariaga (2013) in their study of the Iwate earthquake). The value of κ_1, on the other hand, is quite large. Madariaga & Olsen (2000) suggested that large value of κ are associated with super-shear rupture speed. Ruiz & Madariaga (2013) have observed super-shear rupture for $\kappa \sim 2.06$. In our case, $\kappa \sim 1.96$ seems large enough to trigger a super-shear rupture. The link between κ and the rupture speed will be studied in more detail in the following section.

We have also calculated R_c, which is the minimum rupture patch necessary for the rupture to grow. Because we use a circular initial asperity to trigger the rupture, we determine R_c using the expression derived by Day (1982):

$$R_c = \frac{7\pi}{24} \frac{T_u \mu}{T_e^2} D_c, \tag{4.8}$$

where T_u refers this time to the strength of the initial asperity (T_a). The rupture model obtained by the inversion has an R_c of 1.7 km, giving a ratio R_c/R_a of about 1.25. The inversion has therefore converged towards a size for the initial asperity that is appropriate relative to its strength. Andrews (1976) and Das & Aki (1977a) have investigated the relationship existing between the ratio R_c/R_a and the parameter S and how it reflects the rupture speed. In our case, depending on the ellipse, we are in the sub-shear or super-shear domain. Further investigations on this topic will be

done in the following section.

In addition to S, we have defined two other non-dimensional parameters that control the behaviour of the rupture. To investigate the inter-relationship between these parameters, we project all of the models sampled by the NA-algorithm onto a 3-D space defined by the three non-dimensional parameters S, κ and $\mathrm{R}_c/\mathrm{R}_a$. Figure 4.7(a) shows the 3-D view as well as the three cross-sections associated with Ellipse 1 (i.e. the one that will converge as the hypocentral ellipse) and Figure 4.7(b) represents Ellipse 2 (i.e. the one that will converge as the main ellipse). On both figures, we show the lowest misfit models ($\varepsilon \leq 0.35$, hereafter referred to as LMMs) with larger dots.

Figure 4.7(a,b) shows that at the scale of the whole parameter space, we can say that the LMMs are concentrated within a specific region. This region defines therefore an optimum area within which all models fit the data relatively well compared to models outside it. However, the variation of the non-dimensional parameters within that region are significant and the LMMs do not pin point a single particular model. This is a clear illustration of the non-uniqueness of the dynamic inversion. A good fit of the data is associated with a large family of models rather than one model in particular. The Monte-Carlo exploration carried out in the next section will give further insight into the common features of that family of good fitting models.

Examination of these figures also highlights that some trade-off that exists between the different parameters. For instance, we observe a clear trade-off between $\mathrm{R}_c/\mathrm{R}_a$ and κ on both Figure 4.7(a) and Figure 4.7(b). Thus, when κ increases, $\mathrm{R}_c/\mathrm{R}_a$ decreases and conversely.

We also observe that some regions of the plane (κ,S) are practically not sampled by the NA-algorithm (large S and large κ for Ellipse 1 and low S and large κ for Ellipse 2). The NA-algorithm has therefore rapidly identified these zones as non-favourable for a satisfactory fit to the data.

If we take the LMMs with the lowest ratio $\mathrm{R}_c/\mathrm{R}_a$ ($\sim$0.6), we can make a compar-

ison with the results of Das & Aki (1977a). According to Das & Aki (1977a), these LMMs are located in a region where the rupture speed is supposed to between $\frac{3}{4}c_r$ and c_r (c_r being the Rayleigh wave speed). With the rough approximation that $c_r \sim 0.9v_s$ (v_s being the shear-wave speed), we obtain a rupture speed for the main ellipse of about 3.0 km/s, in agreement with what we observe for the model obtained by the inversion. Because Das & Aki (1977a) only applied for R_c/R_a less than 1.0, it is difficult to assess if this can be applied for LMMs with large R_c/R_a. For this reason, we do not attempt this calculation for the first ellipse. Although it is a convincing result, it only relates to specific models (low R_c/R_a). Further investigations on this issue will be conducted in the next section for a larger range of models.

The dynamic inversion of the displacement records has converged toward a model that is compatible with the results obtained from kinematic inversions. It is interesting to note that the independent convergence of the two approaches toward a similar rupture model emphasises the robustness of the determined rupture source process. The investigation of the parameter space shows the non-uniqueness of the dynamic inversion. In order to further investigate this issue, we decided to perform a Monte-Carlo (MC) exploration of the parameter space fixing the geometry of the rupture area to focus only on the dynamic parameters.

4.7   Fixed-Geometry Dynamic Exploration (FGDE)

Performing a fixed-geometry dynamic exploration (henceforth abbreviated as FGDE) allows a broad investigation of the entire parameter space thanks to the lowering of the number of parameter from 16 to 6 parameters: S_1, S_2, T_e, α, R_a and D_c. This exploration helps to assess the uncertainties associated with the dynamic inversion due to the non-uniqueness of the inverse problem solution. This is done by investigating a large range of different rupture models and analysing under which conditions it can and cannot successfully fit the data.

(a) Hypocentral Ellipse or Ellipse 1
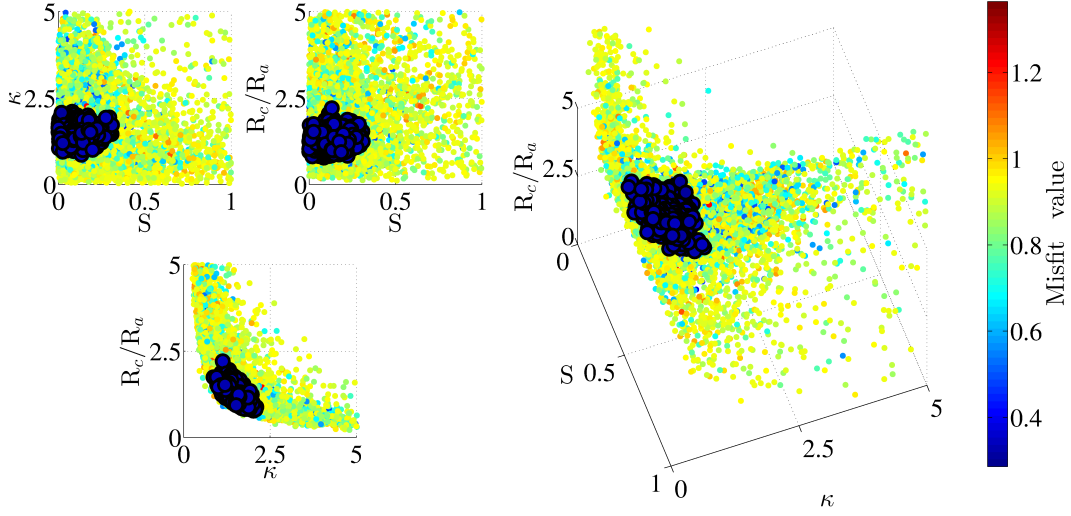
(b) Main Ellipse or Ellipse 2
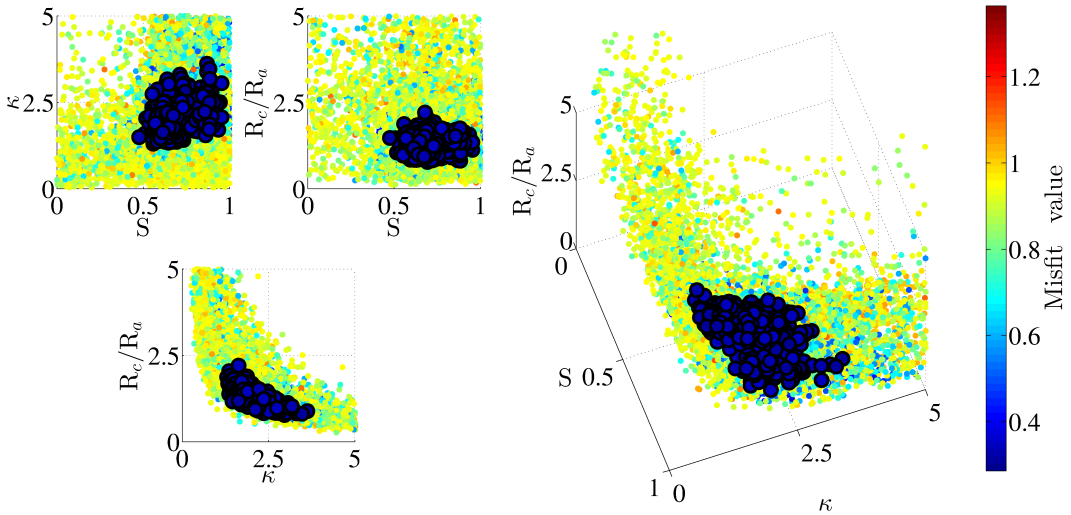
Figure 4.7: (right-side): Projection of all models sampled by the NA-algorithm onto the 3-D space defined by S, κ and R_c/R_a. (left-side): Three cross-section of the 3-D space: the plane (S,κ) (top-left); the plane $(S, R_c/R_a)$ (top-right); the plane $(\kappa, R_c/R_a)$ (bottom-middle). In each figure, the dots are colour-coded according the value of the misfit. Large dots are used to represent the lowest misfit models ($\varepsilon \leq 0.35$). The top four figures (a) are associated to the Hypocentral Ellipse or Ellipse 1. The bottom four figures (b) are associated to the Main Ellipse or Ellipse 2.

In this section, we use two geometries. One is the geometry taken from the dynamic inversion and the other one is taken from the preferred kinematic rupture model of Twardzik et al. (2012).

Geometry obtained from Dynamic Inversion:

In this case, we use the geometry that we have obtained from the dynamic inversion, and we explore the dynamic parameter space within the range of values defined by Table 4.1.

Parameters:	S_1	S_2	T_e (MPa)	α	R_a (km)	D_c (m)
Lower end	0.00	0.00	0.50	1.10	1.25	0.10
Upper end	1.00	1.00	20.00	1.20	2.50	2.00
Optimal values (MC)	0.98	0.49	5.76	1.17	1.57	0.30
Optimal values (Inv)	0.08	0.62	4.16	1.13	1.33	0.17

Table 4.1: Range of values explored by Monte-Carlo method for the 6 dynamic parameters and the optimal value associated to the lowest misfit model sampled during the process.

Table 4.1 shows that the exploration finds a different set of optimal values. The value of the misfit associated with the MC exploration is slightly higher than the one reached by the Inversion (0.30 instead of 0.29), probably because the region around the lowest misfit model is less densely sampled compared to the Inversion. Figure 4.8 shows the comparison between the observed and the calculated displacement records and we observe that the calculated waveforms for that rupture model are almost identical to the calculated waveforms associated with the lowest misfit model obtained by inversion. This rupture model is therefore an equally plausible rupture process for the Parkfield earthquake.

When we look at the details of the rupture process (Figure 4.9), we observe some differences with the rupture process obtained by inversion (see Figure 4.4 for comparison). First, it does not rupture the hypocentral ellipse, due to the drastic change of the strength of the asperity (S_1 ~0.98 instead of S_1 ~0.08). It therefore indicates that this patch might not be reliable since it does not significantly affect the calculated waveforms. The final seismic moment is higher than the rupture model obtained by the inversion (1.42×10^{18} Nm instead of 1.18×10^{18} Nm). Finally, the average rupture speed of the main asperity is higher (3.28 km/s), but still below the shear wave speed of the medium at the depth of the rupture.

71
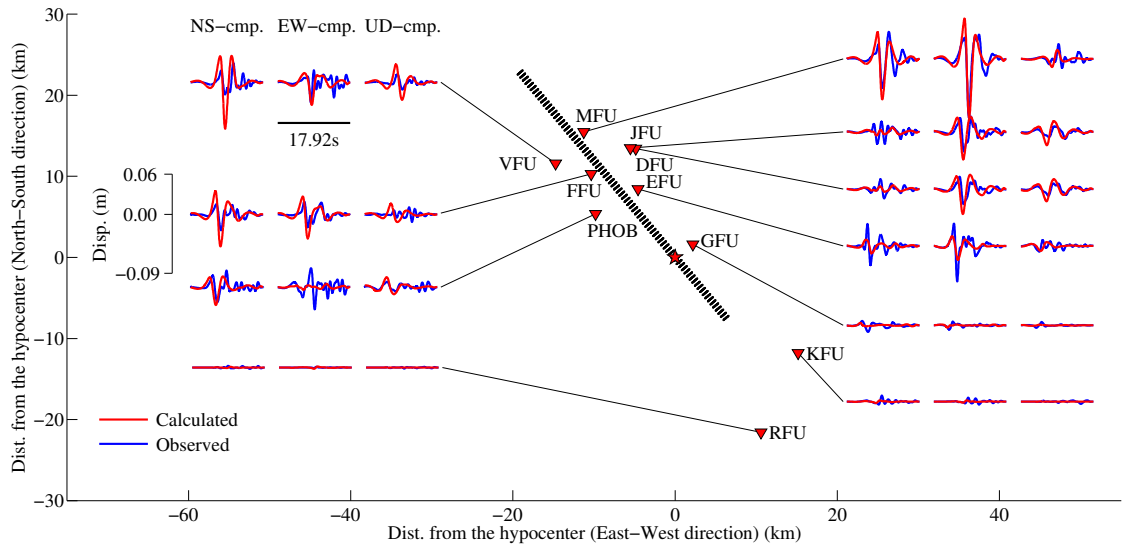
Figure 4.8: Comparison between the observed displacements (blue traces) and the calculated displacements obtained for the best model identified by the Monte-Carlo exploration (red traces). Compared with Figure 4.3, we observe that the fit is almost equal to the one observed for the model obtained by the full dynamic inversion.

Initial distribution of stresses obtained by MC exploration:
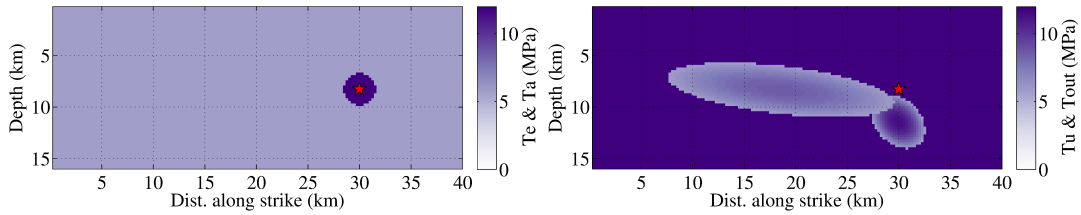
Rupture process obtained by MC exploration:
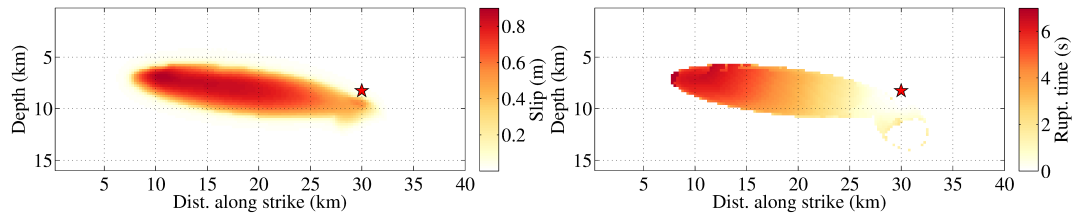
Figure 4.9: (top-left): Initial stress conditions prior the propagation of the rupture. The whole fault is under the tectonic stress and an initial asperity needed to trigger the rupture is located at the hypocenter. (top-right): Rupture area defined by spatial variation of the upper yield stress. (bottom-left): Final slip distribution. (bottom-right): Distribution of the rupture isochrones. In all figures the star represents the location of the hypocenter.

In order to track the behaviour of the rupture process for each model tested during the exploration, we have made a record of the seismic moment and the average rupture speed for each model. To determine the latter, we use a fixed-point located

20.75 km north-west of the hypocenter and 7.26 km deep and we use the time at which this point starts to rupture. We do not do this for the hypocentral ellipse due to its unreliability, as mentioned previously.

Figure 4.10(a) shows the models sampled during the MC exploration projected onto the 3-D parameter space defined by the three non-dimensional parameters described earlier. The dots are colour-coded according to the average rupture speed. In order not to overload the figures, we do not display the models with infinite rupture speed (i.e. the models for which the rupture time of the fixed-point is zero). We observe a highly structured parameter space when we look at it in terms of rupture speed. Amongst other things, we observe that if S $\lesssim$ 0.16, there is no critical value for κ and the rupture always occurs at low rupture speeds ($\lesssim$ 2.0 km/s). If S $\gtrsim$ 0.16, we observe a critical value of κ, below which the rupture does not propagate over the entire asperity, and this value increases with S, going from $\sim$0.5 to $\sim$ 0.9. We also observe that for $R_c/R_a \lesssim$ 0.8, all of the ruptures propagate at super-shear rupture speed regardless of the value of S. Above that, the parameter space exhibits a transition sub-shear/super-shear structured in the same way as Andrews (1976) and Das & Aki (1977a) have observed. The relationship between κ and R_c/R_a is a complex. We see that when κ is about 1.7, we have some kind of a "growth". This occurs almost right after the first transition between sub-shear/super-shear around $\kappa = 0.90$ and $R_c/R_a = 1.50$. Once we cross that limit, we fall again into a zone of sub-shear rupture speed at the level of the "excrescence", before penetrating again into a region of super-shear rupture speed when $R_c/R_a \lesssim$ 0.80.

In Figure 4.10(b), the models are colour-coded according to the seismic moment. This time, we observe almost no structure in the parameter space. We only see that if S $\lesssim$ 0.16, $\kappa \lesssim$ 0.55 and $R_c/R_a \gtrsim$ 2.0, we always have a rupture model that ends up with a low seismic moment ($\lesssim 1 \times 10^{18}$ Nm).

The FGDE using the geometry obtained by dynamic inversion shows that one
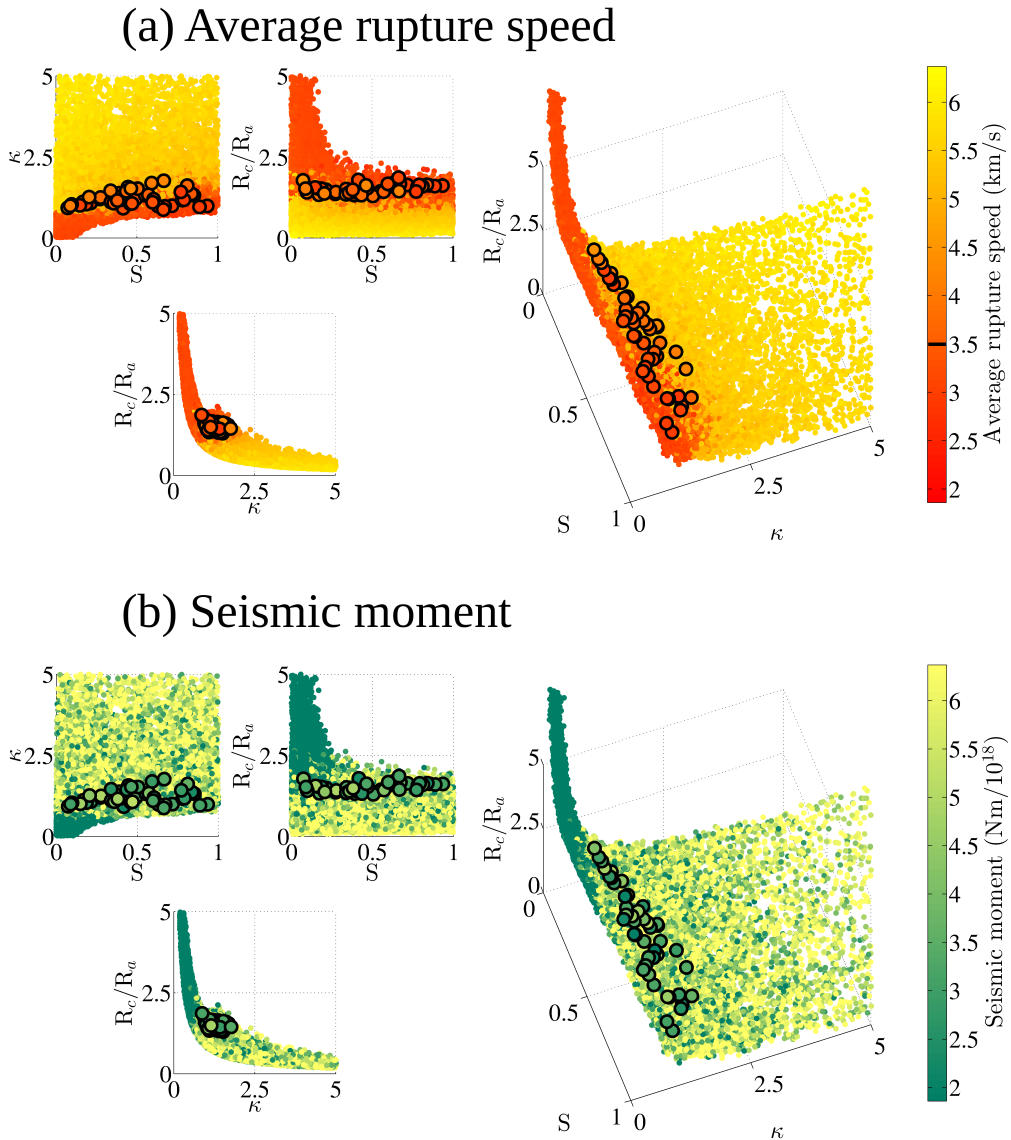
Figure 4.10: (right-side): Projection of all models sampled by the MC exploration onto the 3-D space defined by S, κ and R_c/R_a. (left-side): Three cross-sections of the 3-D space: the plane (S,κ) (top-left); the plane $(S,R_c/R_a)$ (top-right); the plane $(\kappa,R_c/R_a)$ (bottom-middle). In the top four figures (a), the dots are colour-coded according to the value of the average rupture speed, while in the bottom four figures (b), the dots are colour-coded according to the value of the seismic moment. Larger dots are used to represent the lowest misfit models ($\varepsilon \leq 0.35$).

of the important factor that control the fit is the rupture speed. It also shows that this characteristic of the rupture process is strongly controlled by the set of dynamic parameters, while the seismic moment exhibits almost no structure within the parameter space.

Geometry obtained from Kinematic Inversion 6 by Twardzik et al. (2012):

For this case, we use the geometry of the kinematic rupture model obtained from Inversion 6 by Twardzik et al. (2012). This is an important case to study because it evaluates the dynamic feasibility of the kinematic model. The aim is to find stress conditions that can reproduce a similar rupture scenario to the one obtained by kinematic inversion. That a kinematic model is dynamically plausible or not would therefore become a criteria that will help to reduce the non-uniqueness associated with kinematic inversion.

The rupture geometry consists of two separate ellipses. The first one is circular and located a little below the hypocenter of about 3.2 km radius. The second one is located about 20 km north-east of the hypocenter and has a more elliptical shape with a major semi-axis of 6 km and a minor semi-axis 2 km. The particularity of this model is that it contains a jump in the rupture process from the hypocentral ellipse to the second ellipse. With the MC exploration, we explore the stress conditions under which there is a jump in the rupture process and see if it can fit the displacement records of the Parkfield earthquake.

The MC exploration has found a lowest misfit model with a misfit value of 0.67. Although the rupture jumps from one ellipse to the other during its propagation, the value of the misfit is clearly higher than for the kinematic rupture model of Twardzik et al. (2012) (0.26) and than for the dynamic rupture model (0.29). A comparison between the kinematic rupture model and the dynamic rupture model as well as a comparison between the observed and calculated waveforms for the dynamic rupture model can be found in Appendix A3, Figure A3.9 and Figure A3.10 respectively. It seems that in the case of the Parkfield earthquake, a jump in the rupture process is not compatible with the observed ground motion data. The elliptical sub-fault approximation is however well suited to get the robust features of a given rupture source process (i.e. the area(s) where most of the energy is

75

released), it could therefore be that the two ellipses are not entirely disconnected and that some ruptures could have occurred in between.

In order to investigate that possibility we have adopted a new way to describe the rupture area that uses b-spline curves. By connecting together several b-splines, we construct a closed curve that smoothly merge the two ellipses. Let us define n control points (P_n), with coordinates (x_n,y_n). Then, each b-spline (s_i) is determined using four control points (P_i, ..., P_{i+3}), with coordinates (x_i, y_i),...,(x_{i+3}, y_{i+3}). Each s_i has the following equation:

$$x_i(t) = \tfrac{1}{6}\left[Ax_i + Bx_{i+1} + Cx_{i+2} + Dx_{i+3}\right],$$

$$y_i(t) = \tfrac{1}{6}\left[Ay_i + By_{i+1} + Cy_{i+2} + Dy_{i+3}\right];$$

for $0 \leq t \leq 1$ and with :

$$A = (1-t)^3, \tag{4.9}$$

$$B = (3t^3 - 6t^2 + 4),$$

$$C = (-3t^3 + 3t^2 + 3t + 1),$$

$$D = t^3.$$

If we then loop over all the control points, we can close the curve and define the rupture area. Figure 4.11a shows the configuration of the control point that we use during the inversion of the dynamic parameters. Once we have defined the outline of the rupture area, to determine if a point on the fault plane is within the polygon defined by the b-spline curve, we use the winding point algorithm of Alciatore & Miranda (1995). Using this technique, we have contoured the kinematic

slip distribution and link the two ellipses with a narrow strip (Figure 4.11b).
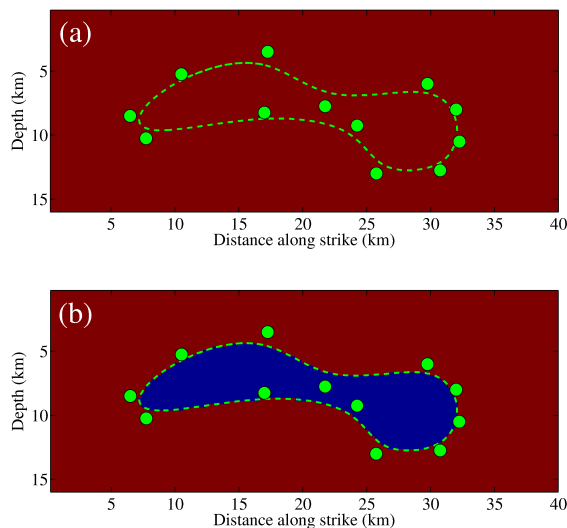
Figure 4.11: (a): A close b-spline curve obtained using 12 control points. (b): Determination of the rupture area using the winding point algorithm of Alciatore & Miranda (1995).

The inversion reaches a misfit value of 0.35, which is more compatible with the previous results obtained from kinematic or dynamic inversions. We can see on Figure 4.12 that despite the difference of misfit between the dynamic rupture model obtained by the full dynamic inversion and the dynamic rupture model obtained from the fixed-geometry dynamic inversion, there are not significant differences in the calculated waveforms. This illustrates once again the high non-uniqueness associated with dynamic inversion. We also note that we have fixed the spatial geometry of the connection between the two ellipses using a trial-and-error approach. There could therefore be a more appropriate geometry of the b-spline curve that might further reduce the value of the misfit. When we look at the obtained dynamic rupture process (Figure 4.13), we observe that it reproduces well the kinematic rupture model. Its average rupture speed is however higher than for the kinematic rupture model (3.3 km/s instead of 2.7 km/s) and its seismic moment is also higher (1.6 $\times$ 10^{18} Nm instead of 1.1 $\times$ 10^{18} Nm) , which could be explained by the addition of the connection between the two ellipses.
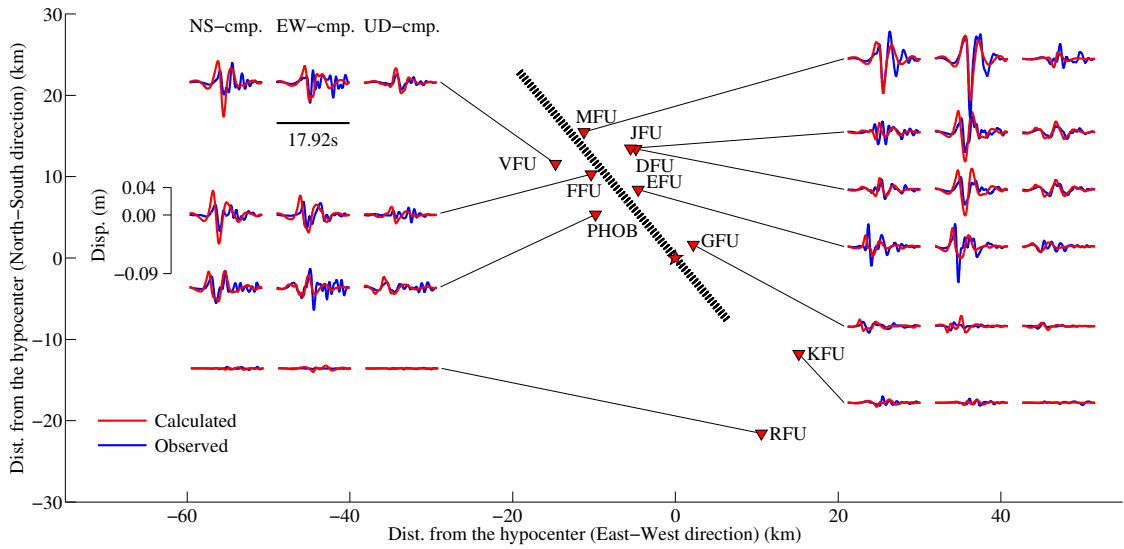
Figure 4.12: Comparison between the observed displacements (blue traces) and the calculated displacements obtained for the lowest misfit model from the dynamic inversion with the geometry of the rupture area defined using b-spline curve (red traces). Compared with Figure 4.3, we observe that the fit is almost equal to the one observed for the model obtained by the full dynamic inversion, although the amplitudes for EW-component records are slightly large in this case.
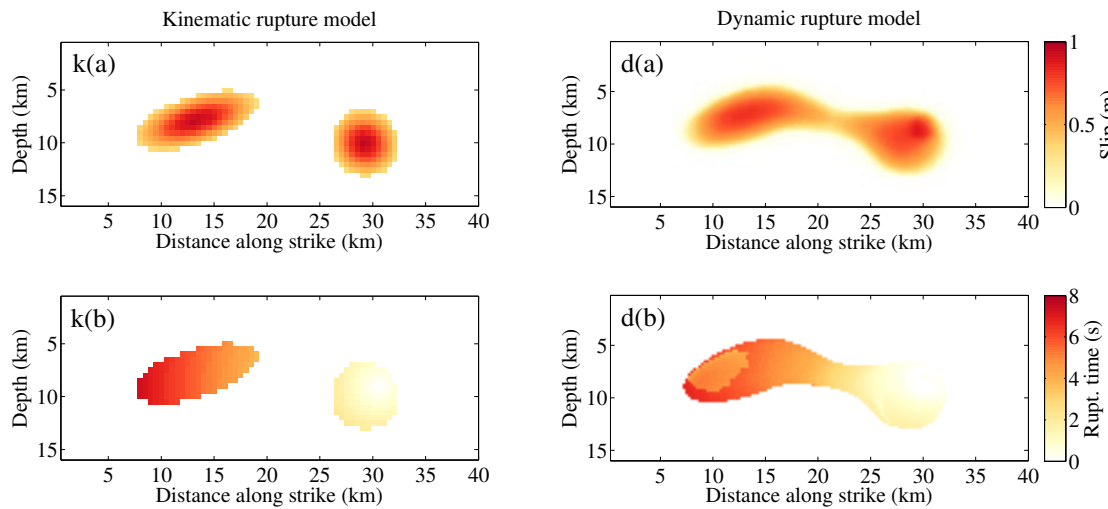
Figure 4.13: Comparison between the kinematic rupture model of Inversion 6 in Twardzik et al. (2012) and the dynamic rupture model obtained from a dynamic inversion with fixed-geometry that is described using b-spline curve. k(a) shows the final slip distribution of the kinematic rupture model and k(b) shows the distribution of the isochrones of the kinematic rupture model. d(a) shows the final slip distribution of the dynamic rupture model and d(b) shows the distribution of the isochrones for the dynamic rupture model.

The final values of the dynamic parameters are similar to what we have obtained in the previous cases (see Table 4.2). We believe that the addition of the connection has allowed the inversion to access the optimal region of the parameter-space, a region in which the rupture models have an average rupture speed and a final seismic moment that is likely to match with the plausible rupture process of the 2004 Parkfield earthquake. Table 4.2 is also interesting because it shows a sample of the variability that we get for each inverted parameters, each set producing a rupture model that fits the data almost equally well compared with the others.

Parameters:	S_1	S_2	T_e (MPa)	α	R_a (km)	D_c (m)
Dyn. Inv.	0.08	0.62	4.16	1.13	1.33	0.17
MC Exp.	0.98	0.49	5.76	1.17	1.57	0.30
FGDI of Kin. Mod.	0.49	0.10	4.60	0.90	1.25	0.32

Table 4.2: Comparison between the optimal values that are obtained from the different dynamic inversion that we have been performed in this study. Dyn. Inv. refers to the full dynamic inversion. MC Exp. refers to the Monte-Carlo exploration done using the geometry of the rupture area from the results of the full dynamic inversion. FGDI of Kin. Mod. refers to the results from the Fixed-Geometry Dynamic Inversion that uses the geometry of the rupture area from the results of Kinematic Inversion 6 of Twardzik et al. (2012) and with a connection between the two ellipses created using a b-spline curve. Note that in this case, the bridge between the two ellipses has its own value of S that is 0.40.

This example shows that the preferred kinematic model of Twardzik et al. (2012) is not dynamically correct in its original geometry. Indeed, the different sets of dynamic parameters that can reproduce a jump of the rupture process cannot fit the data reasonably well at the same time. Once we add a connection between the two ellipses, we are able to find a set of dynamic parameters that can reproduce the kinematic rupture model as well as fit the data. Because of the low slip amplitude in the area in between the two asperities, it is likely that the kinematic inversion avoided it in order to focus only on the main areas of moment release.

4.8 Conclusions

We have performed a full dynamic inversion for the rupture process of the September 28, 2004, Parkfield, California, earthquake using a method in which stress and frictional properties on the fault are described using elliptical patches. The final rupture model is essentially described by one ellipse of 4 km wide and elongated in the strike direction. The rupture occurs at more or less constant speed of 2.8 km/s and the final seismic moment is 1.18×10^{18} Nm. The ratio of strain to fracture energy (κ) for this earthquake is 1.40, in agreement with other studies, which indicates a rupture process occurring at sub-shear rupture speed. The stress drop of this earthquake is about 4 MPa with a ratio between strength and stress drop (S) is about 0.7. We have also calculated the ratio R_c/R_a that is 1.25. To investigate the variability of plausible models, we have explored the dynamic parameter-space, fixing the geometry of the rupture area from the results of the inversion, using a Monte-Carlo method. In order to visualise the entire parameter-space, we reduced it to a 3-D space defined by κ, S and R_c/R_a. We observe that the rupture models are distributed inside this space depending on their rupture speed and final seismic moment. There exists therefore an optimal region in which the specific combination of κ, S and R_c/R_a produces rupture models that match the data relatively well. It shows that there is not a unique solution and that, at fixed-geometry, there is a range of combinations of κ, S and R_c/R_a that can produce a rupture history that seem to be plausible to explain the rupture process of the 2004 Parkfield earthquake. Using the fixed-geometry approach, we concluded that the kinematic rupture model may not be dynamically correct in its original form, i.e. that by keeping the geometry of the ellipses obtained from the kinematic inversion unchanged, we could not find a set of dynamic parameters that reproduced the kinematic rupture model while fitting the data. Using the b-splines method to define the rupture area, we were able to overcome this issue with the addition of a secondary feature that is a connection between the two disconnected ellipses of the kinematic rupture model.

This has made possible the reproduction of the general features of the kinematic rupture model while fitting reasonably well the data at the same time. It is indeed important that the kinematic model can be converted into a dynamically correct rupture model to prove its likelihood.

Chapter 5

Stress Transfer History of the 2010-2011 New-Zealand Earthquake Sequence and its Implication for the Alpine Fault

5.1 Introduction

New-Zealand lies on the Indo-Australia-Pacific plate boundary. North-east of North Island, the Pacific plate subducts under the Australian plate at a rate of ~35 mm/yr (DeMets et al. 2010). South-west of South Island, the polarity of subduction is reversed and the Australian plate subducts beneath the Pacific Plate along the Puysegur trench. Separating these subduction zones and through the South Island, transpressional plate motion is accommodated as right-lateral strike-slip along the Alpine Fault (Figure 5.1). It is well established that at the plate boundaries, there is an equilibrium reached over < 1000 years between the rates at which strain is accumulated and released during earthquakes (Calais & Stein 2009). However, away from the plate boundary, in the plate interior, this steady-state may not be applicable. Assessing the seismic hazards in such area might therefore be challenging. Indeed, Bouchon et al. (2013) have shown that a precursory phase observed prior to large interplate earthquakes is much less frequent for intraplate earthquakes.
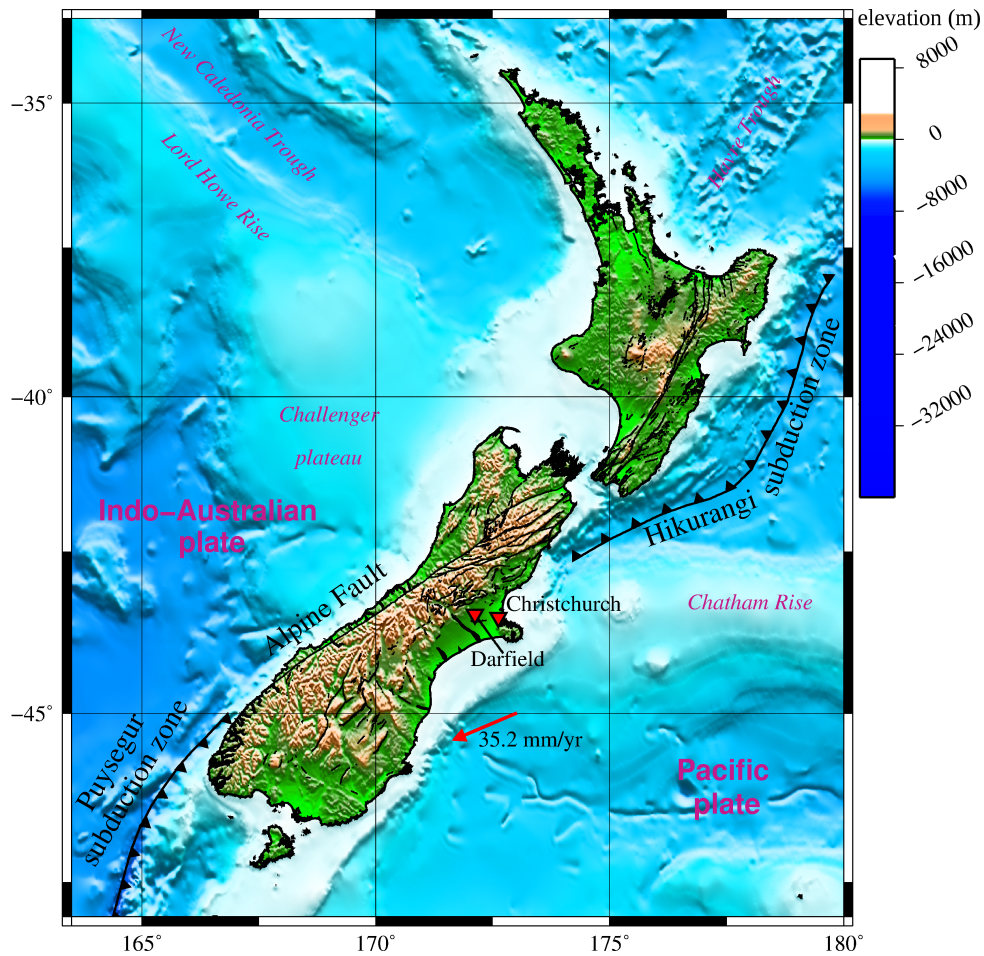
Figure 5.1: Plate configuration of New-Zealand. The red arrow indicates the plate motion vector of the Pacific plate relative to the Indo-Australian plate (DeMets et al. 2010), and the red triangles mark the location of the two cities after which the major earthquakes of the 2010-2011 sequence are named.

England & Jackson (2011) have counted 100 earthquakes that have occurred within the continental interior over the past 120 years, causing 1,400,000 deaths. The threat associated with these earthquakes are thus considerable. In order to improve our knowledge of the seismic hazard associated with those kind of earthquakes, we focus our study on the sequence of earthquakes that occurred in the South Island of New-Zealand from the end of 2010 until early 2012.

On September 3rd, 2010, a M_w7.0 earthquake occurred near the town of Darfield (population ∼1400), located at about ∼150km east of the Alpine Fault, in the Canterbury Plains, South Island, New Zealand. It was followed five and half months

later, on February 21st, 2011, by a M$_w$6.1 near the city of Christchurch (population $\sim$ 370,000), located $\sim$50km east of Darfield. Although smaller in magnitude, it caused considerably more damage and resulted in >180 casualties. A third earthquake of M$_w$6.0 occurred on June 13th, 2011 in close proximity to the February 21st, 2011 earthquake. Approximately 6 months later, on December 23rd, 2012, a swarm of earthquakes started off-shore Christchurch, with several earthquakes above M$_w$5.0, terminating the 2010-2011 New-Zealand earthquakes sequence.

This sequence documents a progressive migration of the seismicity from the region near the Alpine fault toward Darfield, toward Christchurch and finally offshore east of South Island. Many studies have demonstrated how the static stress changes caused by the occurrence of moderate to large earthquakes appear to modulate the location of future earthquakes (e.g. Das & Scholz (1981); Harris (1998); Stein (1999); Toda et al. (2012)). Using seismic activity as a proxy of stress, we investigate the stress release history of the surrounding region of the Darfield and Christchurch earthquakes.

5.2   Earthquake Catalogue

The first catalogue that we use contains earthquake hypocenter reported by the GeoNet project, sponsored by the Earthquake Commission (EQC), GNS Science and Land Information New Zealand (LINZ). In a rectangular region: [171.12-173.12°E; 44.50-42.50°S], GeoNet reports a total of 33,526 earthquakes between 1844 to September 2012. The advantages of this catalogue is that it has a consistent magnitude-type for all earthquakes as well as a low magnitude of completeness (M$_L$2.5). Earthquakes with M$_L$ <2.5 are not considered in this study.

We also use earthquakes from the International Seismological Centre (ISC). This catalogue has a total of 9,821 earthquakes reported in the same area of interest between January 1964 and September 2013, with most of the earthquakes already

reported by the GeoNet catalogue. However, the ISC catalogue has the advantage of including worldwide recorded phase arrival-time, which can be used to attempt earthquakes relocation. In order maintain the consistency in magnitude-type between the two catalogues, we use the magnitude reported by the GeoNet project for earthquakes reported by ISC.

For the relocation, we only use P-waves recorded at stations located at a distance $\leq 100°$. All other phases are excluded. This is motivated by the fact that phases other than P-waves are potentially not reliably reported by the ISC (e.g. Schöffel & Das 1999; Hurukawa et al. 2012).

5.3   Joint Hypocenter Determination (JHD)

The determination of hypocenter locations is based on arrival times of seismic waves (t_i), recorded at N stations ($N \geq 4$) of spatial coordinates (ϕ_i,λ_i). t_i can be expressed as non-linear functions of the stations coordinates, the seismic velocity structure of the Earth, and the focal parameters of the earthquake that are its spatial location (ϕ_0,λ_0), its depth (h) and its origin time (t_0). From an initial solution of the earthquake focal parameters ($\phi_0',\lambda_0',h',t_0'$) and assuming that this solution is near enough to the true solution, the set of N equations can be linearised using a Taylor expansion:

$$t_i = t_i' + \delta t + \frac{\partial t_i}{\partial \phi}\delta\phi + \frac{\partial t_i}{\partial \lambda}\delta\lambda + \frac{\partial t_i}{\partial h}\delta h; \tag{5.1}$$

t_i' being the theoretical arrival-times calculated at each stations i ($= 1,...,N$) from the initial solution. We can express in matrix form the differences between observed and theoretical arrival times ($r_i = t_i$ - t_i') at each station ($i = 1,...,N$):

$$r_i = A_{ij}\delta x_j. \tag{5.2}$$

i refers to the number of stations (i.e. $i = 1, ..., N$) and j refers to the 4 focal parameters. The matrix A_{ij} is therefore composed of the partial derivative of the travel-time at each station i with respect to the j-th focal parameter (see Equation 5.1). r_j can be then minimised by progressively adjusting the focal parameters of the initial solution.

However, the problem is frequently not well conditioned. This is often caused by real travel-time anomalies resulting from structures not present in simplified models of Earth's velocity structure. It is possible to overcome this issue by introducing stations corrections that takes into account the travel-time anomalies. This is achieved using the method of Joint Hypocenter Determination (JHD), initially proposed by Douglas (1967) and developed by Dewey (1971), which consists of the simultaneous determination of the focal parameters for a small set of M earthquakes, using the arrival times observed at N stations, the same N stations for each of the M earthquakes. JHD needs one earthquake as a calibration earthquake for which we assume that the focal parameters are known. In this case, the set of linearised equation becomes:

$$r_{jk} = A_{skj}\delta x_{sk} + \delta g_j. \tag{5.3}$$

The index j is used for the N stations, the index k is used for the M earthquakes and the index s is used for the 4 focal parameters. Compared to Equation 5.2, there is one additional term, δg_j, which corresponds to the station corrections.

Once the stations corrections are calculated for the small set of M earthquakes, they can be used to relocate all other earthquakes found in the vicinity. JHD operates optimally for earthquakes relatively close to each other so that the stations corrections are the same for all earthquakes, making this method suitable for our study. To attempt the relocation of the 9,821 earthquakes reported by the ISC, we use a set of 20 earthquakes to determine the stations corrections and we use the Darfield earthquake hypocenter as the calibration earthquake.

Using that approach, we have relocated 5,750 earthquakes (59 % of the whole

ISC catalogue). From the relocated earthquakes, 5,269 have their semi-major axis of their 90% error ellipse ≤30 km (∼92% of the relocated earthquakes). 4,976 have their semi-major axis of their 90% error ellipse ≤20 km (∼87% of the relocated earthquakes). 2,901 have their semi-major axis of their 90% error ellipse ≤10 km (∼50% of the relocated earthquakes). 81 have their semi-major axis of their 90% error ellipse ≤5 km (∼1% of the relocated earthquakes). We therefore consider an earthquake to be 'reliably relocated' when its semi-major axis of its 90% error ellipse is <20 km.

5.4 Seismicity Prior the Darfield Earthquake

Figure 5.2 shows the reliably relocated earthquakes (open circles). We also show the density of earthquakes (i.e. the number of earthquake per km^2) calculated from the non-relocated earthquakes using the location reported by GeoNet. One striking feature is the almost complete lack of seismic activity in a region that spreads over the whole Canterbury Plains.

Studies on subduction zones have demonstrated that episodes of low seismic activity could be indicative of the imminent occurrence of a large earthquake (Fedotov 1965; Mogi 1969; Kanamori 181; Mogi 1990). For this model to be valid, it would require observations of an intense period of seismic activity prior to the quiet episode. Also, unlike a context of subduction, it is difficult to assess the relevance of a low seismic activity simply because we did not know where the hazards (e.g. faults) were located prior the occurrence of the Darfield earthquake (England & Jackson 2011). Even if we knew, it remains difficult to assess the significance of a quiet episode and its likelihood to lead to a major earthquake (see e.g. Wyss et al. 1996 and Rundle et al. 2011 for a more detailed discussion).

When we look at the space-time distribution of earthquakes prior the September 2010 Darfield earthquake (Figure 5.3), there is no such pattern like the one described
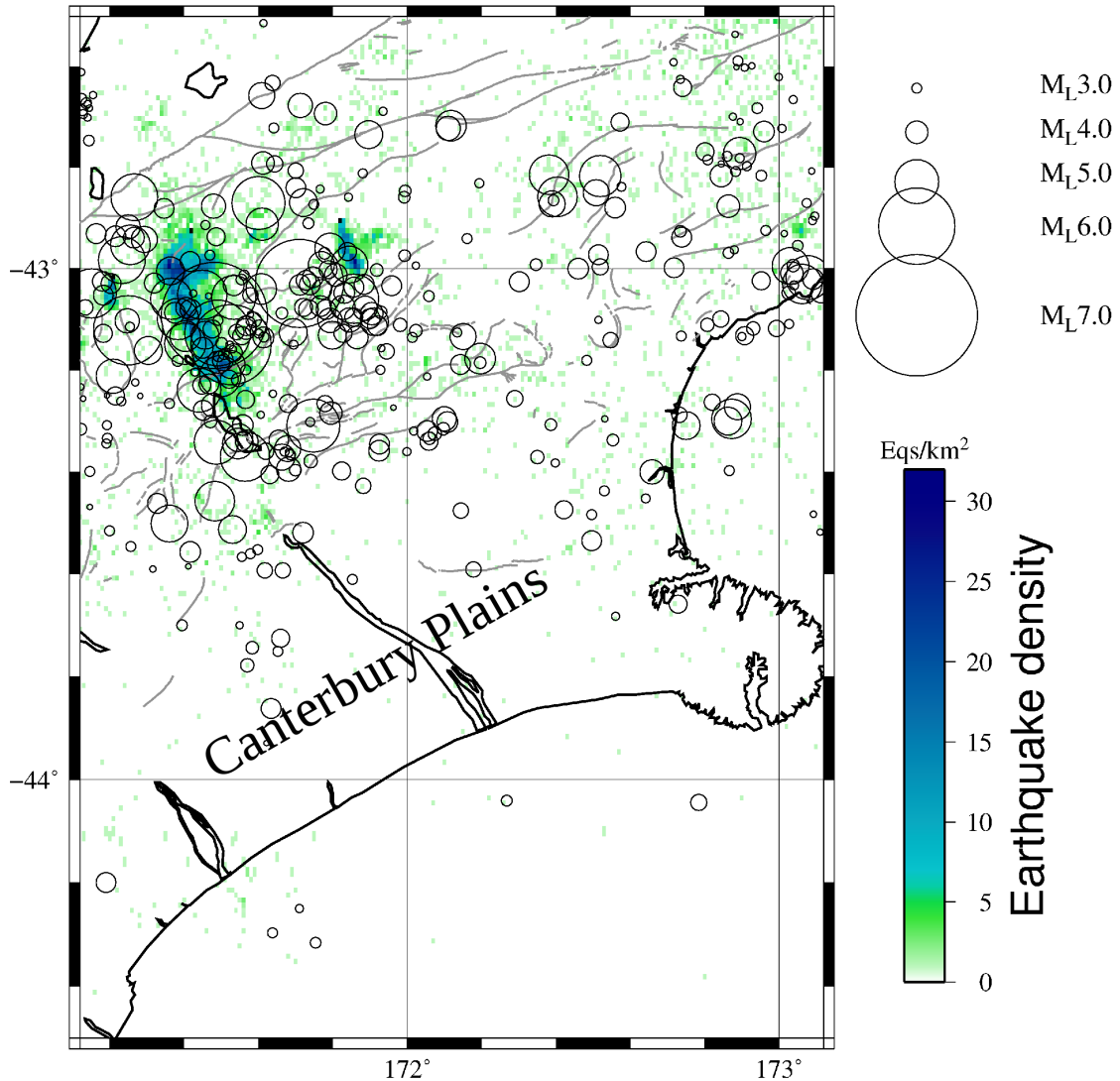
Figure 5.2: Seismic activity prior the Darfield earthquake (Jan. 1, 1964 to Sept. 2, 2010). The open circles show the reliably relocated earthquakes with size function of their magnitude (M_L). The background shows the density of earthquake (i.e. the number of earthquake per km^2). It is calculated from the non-relocated earthquakes using the location reported by the GeoNet catalogue. It aims to show the seismic activity. The fault traces are from the GeoNet project and are shown in grey.

for subduction zones. However, this distribution shows an interesting trend of the seismic activity.

Between 1940 and 1950, all earthquakes are located ∼50 km away from the epicentral area of the Darfield earthquake. After a period of low seismic activity between 1950 and 1970, we observe an re-increase of the activity around 1970. We also note that it has moved closer to the Darfield region (∼20 km away). From 1970,

Figure 5.3: Space-time diagram of the seismicity (2.5≤M_L) from 1940 to 2010 relative to the Darfield epicentre. Circles represent earthquakes reliably relocated, while crosses represent non-relocated earthquakes. Large symbols are for earthquakes with 4.0≤M_L, a threshold that corresponds to the magnitude of completeness in the time period from 1940 to 2010. The black arrow shows the time of occu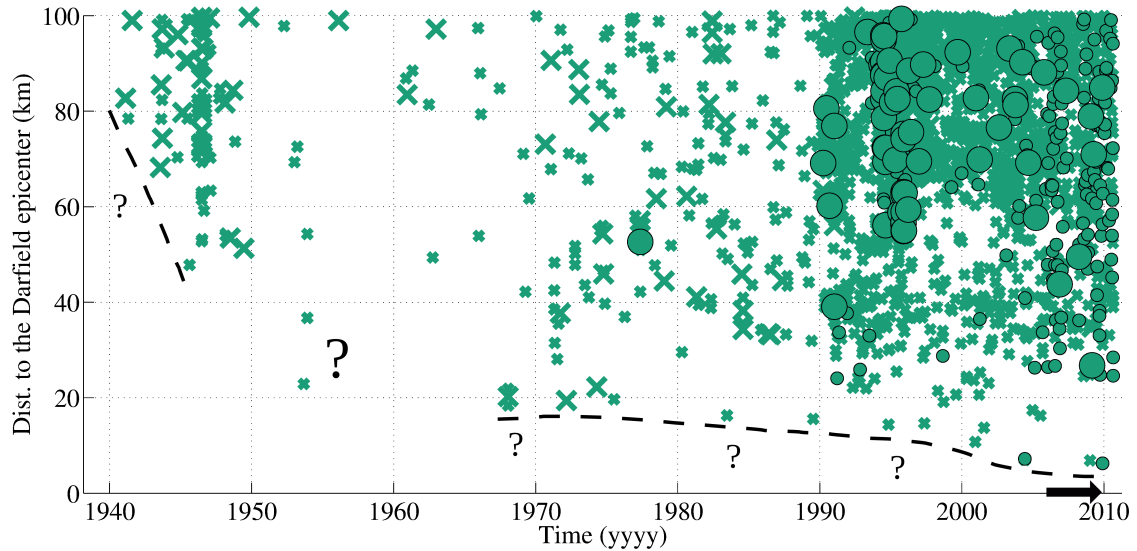rrence of the September 2010, Darfield earthquake. The dashed line illustrates the hint of migration toward the Darfield epicentral area that we observe in the seismic activity.

the seismic activity progresses toward the future epicentre of the Darfield earthquake (from about 20 km in 1970 to about 5 km away in 2010). This migration of the seismicity toward Darfield could be indicative of a progressive stress transfer from the plate boundary to the plate interior.

Because this behaviour is mostly observed with the non-relocated earthquakes, it is difficult to assess its reliability. However, the implication that this could have for seismic hazards motive further investigations in order to prove or disprove this hypothesis.

5.5 Seismicity Following the Darfield Earthquake

We have decided to look at the seismic activity of the whole 2010-2011 sequence in three distinct time periods. The first one (Period I) is from September 3rd, 2010 (day of the M_L7.1 Darfield earthquake) to February 20th, 2011. The second one

(Period II) is from February 21st, 2011 (day of the $M_L 6.3$ Christchurch earthquake) to December 22nd, 2011. The third one (Period III) starts on December 23rd, 2011 (day of the beginning of the off-shore Christchurch swarm) and finishes at the end of our catalogue (September 1st, 2013).

Period I:

Figure 5.4 shows the aftershock sequence of the Darfield earthquake. During this earthquake, the rupture propagated ∼20 km to the west and ∼20 km to the east of the epicentre, on generally east-west trending segmented faults. A line of aftershocks trends north of the epicentre, in agreement with earlier studies (Gledhill et al. 2011). A cluster of aftershocks is also seen near the eastern end of the rupture. Initial studies suggest that the rupture may have initiated on a blind SW-NE trending fault (Charing Cross thrust fault) and then jumped onto segments approximately oriented east-west (Beavan et al. 2010). Only some of these individual segments are seen in the surface rupture, so the aftershocks highlight the "blind faults" that were activated during this earthquake (Sibson et al. 2011).

When we look at monthly snapshots of the seismic activity during Period I (see Figure A4.1 in Appendix A4), we see that during the first month (Figure A4.1(a)) following the Darfield earthquake, the seismic activity spreads almost over the whole northern region of the Canterbury Plains. In the following month (Figure A4.1(b)), seismic activity dies down, except for one cluster of earthquakes at the eastern-most end of the surface rupture of the Darfield earthquake, which lasted until the beginning of February 2011 (Figure A4.1(b-c-d)). Interestingly, we also observe in January 2011 a short-lived burst of earthquakes very close to the location of the future February 21st, 2011, Christchurch earthquake (Figure A4.1(d-e)). It then disappeared and there was no seismic activity observed in this region for the 3 weeks prior to the Christchurch earthquake (Figure A4.1(f)). This is analogous to a "Mogi doughnut" of "Type A" (Mogi 1969, 1990) in which the seismic activity in the focal
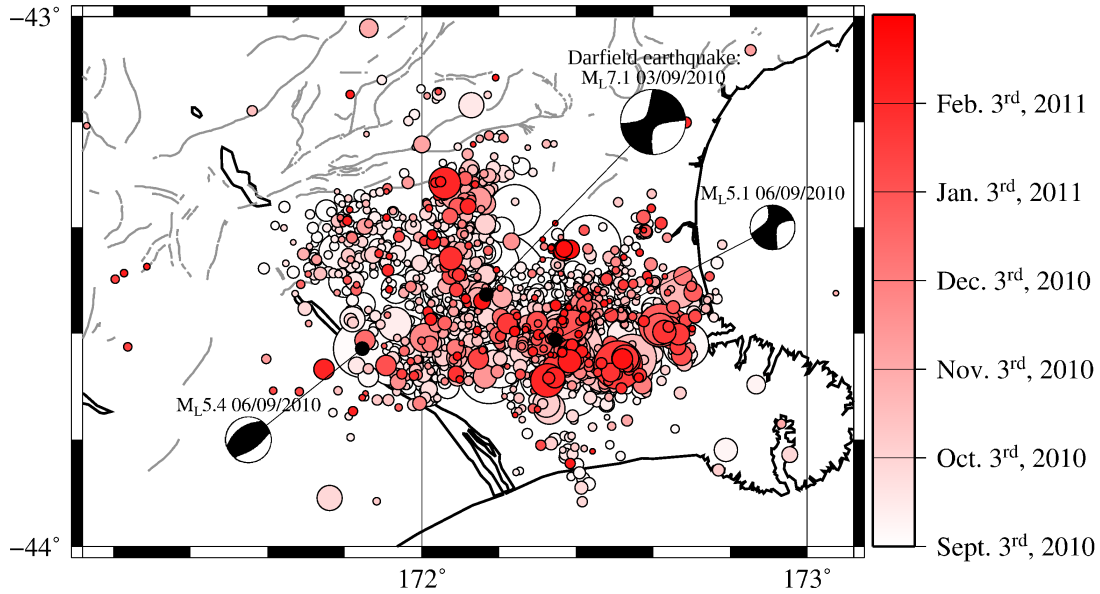
Figure 5.4: Reliably relocated earthquakes from September 3rd, 2010 (day of the Darfield earthquake) to February 21st (day before the Christchurch earthquake). The time of occurrence of the earthquakes are colour-coded, according to the key. The size of the symbols are scaled according to the local magnitude (see Figure 5.2 for key). The CMT mechanisms of earthquakes (only 3) in this period are shown.

region of the future earthquake is high but then becomes very quiet prior a large earthquake, creating a seismic gap.

The Centroid Moment Tensor (CMT) solutions of all earthquakes in this time period show that the Darfield earthquake had only two direct aftershocks large enough to have a CMT solution, one at each end of the surface expression of the fault. The one at the eastern end has the same strike-slip mechanism as the main shock but the one at the western end is a thrust earthquake.

Period II:

Figure 5.5 shows the seismic activity following the $M_L6.3$, Christchurch earthquake, which is the major aftershock of the Darfield earthquake (Stramondo et al. 2011). It occurred on February 21, 2011, at the eastern edge of the area delineated by the Darfield aftershocks. In June 13, 2011, a second earthquake of $M_L6.4$ occurred about 5-10 km north from the 1st Christchurch earthquake epicentre. The seismic activity

associated to Period II is mostly limited to the eastern of the surface rupture of the Darfield earthquake, but some seismic activity remains around the Darfield region.
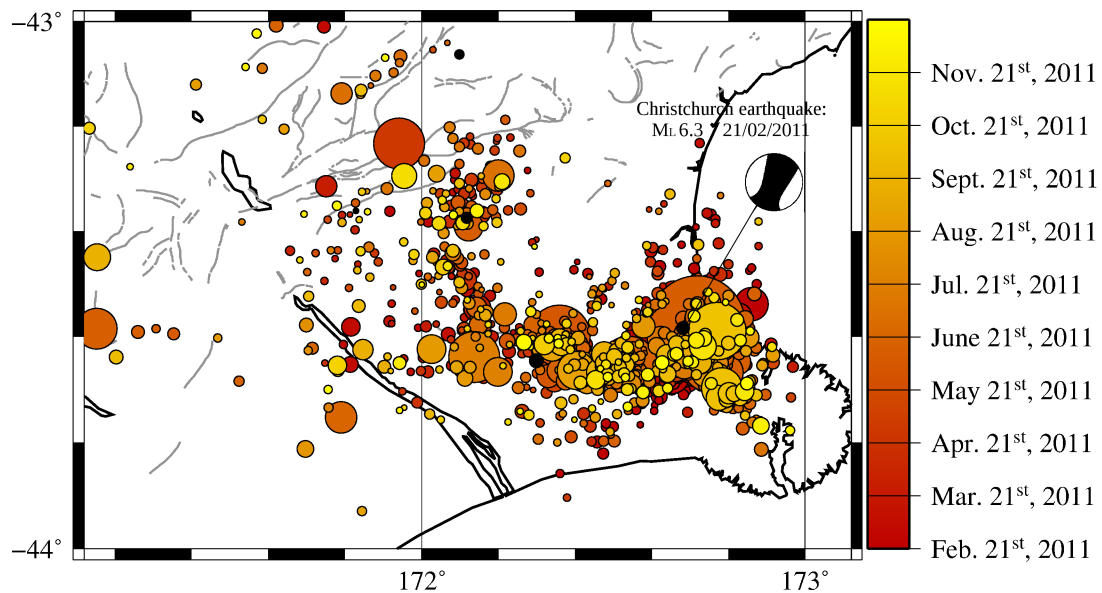

Figure 5.5: Reliably relocated earthquakes from February 21, 2011 (day of the Christchurch earthquake) to December 22nd (day before the beginning of the swarm off-shore Christchurch city). The time of occurrence of the earthquakes are colour-coded, according to the key. The size of the symbols are scaled according to the local magnitude (see Figure 5.2 for key).

The snapshots of the seismic activity (see Figure A4.2 in Appendix A4) show that during the first month following the Christchurch earthquake (Figure A4.2(a)), all earthquakes focus within a narrow region of about 20 km radius around the $M_L 6.3$ Christchurch epicentre. The following months (Figure A4.2(b)), we observe that the earthquakes align in a east-west trend and re-activate the cluster observed during Period I at the easternmost end of the surface rupture of the Darfield earthquake. This reactivation is reinforced by the occurrence of the June, 13, 2011 earthquake (Figure A4.2(c)). During that time, two strike-slip earthquakes large enough to have a CMT solution occurred. Li et al. 2012 suggest that the fault that ruptured during the Christchurch earthquake (Port Hills Fault) and the main strike-slip segment that ruptured during the Darfield earthquake (Greendale Fault) might be connected along "blind faults". By means of stress transfer along these faults, the cluster east of the Greendale Fault could have been re-activated after the occurrence of the

February 21, 2011 and the June 13, 2011, earthquakes. After July 2011 (Figure A4.2(d-e-f)), the seismic activity of the whole region progressively shuts down and almost no earthquakes are observed at the beginning of December 2011.

We see that the occurrence of the Christchurch earthquake has produced a large number of earthquake with a CMT solutions compared to Period I. All of those earthquakes are strike-slip and have a similar mechanism when compared to the Darfield earthquake. It suggests that the whole sequence is the results of the same stress regime.

Finally, we notice that in contrast to Period I, there is no high seismic activity during Period II within the region where the December, 2011 off-shore Christchurch swarm will occur.

Period III:

A swarm of earthquakes, commencing in December 2011 and finishing in January 2012, is located further north-east of the Christchurch earthquake epicentre area (Figure 5.6). It contains three almost simultaneous earthquake of $M_L \geq 5.5$, and also trigger one $M_L 5.1$ earthquake near the Christchurch epicentre. The locations of the earthquake swarm is at the edge of the area delineated by the Christchurch earthquakes aftershocks. Note how the Christchurch region remains seismically quiet after the occurrence of the December 2011 seismic swarm. The high seismic activity carries on for about 1-2 months before progressively reducing in frequency.

This short sequence has produced a significantly large number of earthquakes with CMT solutions. The mechanisms show a change in the type of faulting with thrust faulting instead of strike-slip faulting.
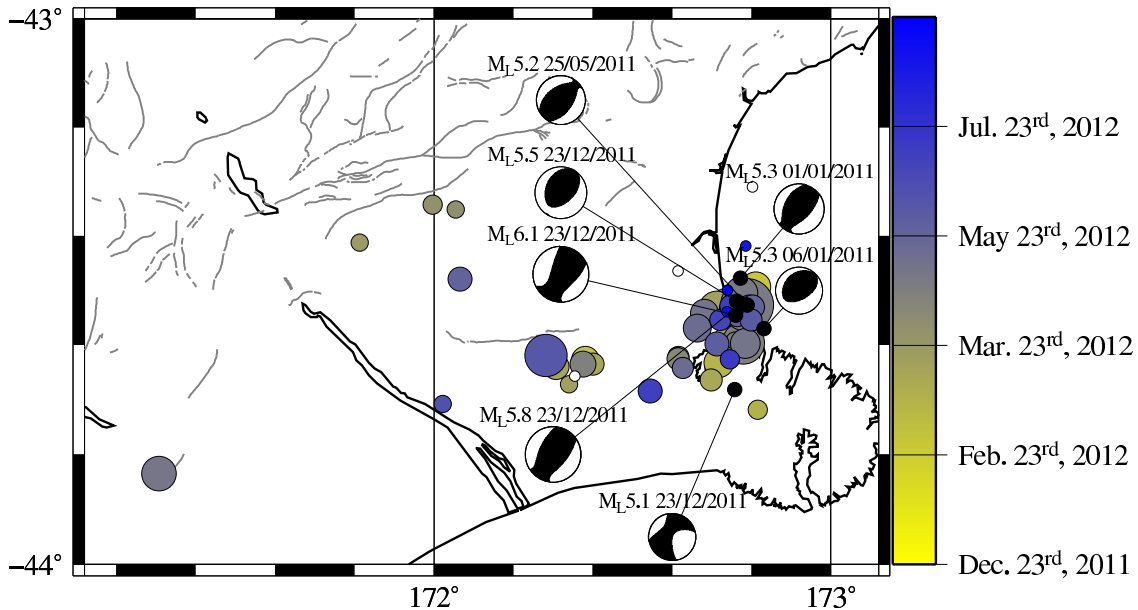
Figure 5.6: Reliably relocated earthquakes from December 23rd, 2011 (beginning of the December off-shore Christchurch swarm) to September 1st, 2013 (end of our catalogue). The time of occurrence of the earthquakes are colour-coded, according to the key. The size of the symbols are scaled according to the local magnitude (see Figure 5.2 for key).

5.6   State of the Stress Before and After the Darfield Earthquake

The pressure (P) and the tension (T) axes from the CMT solutions of all the 28 earthquakes in the region from 1976 till present are shown in Figure 5.7. The figure shows that the whole 2010-2011 New-Zealand earthquake sequence exhibits the same direction for the P- and T-axis, which shows that it results from the same stress regime. The same directions are also observed for earthquakes older than 2010 and closer to the Alpine Fault. It implies that the 2010-2011 earthquakes sequence resulted from the ambient stress of the region. Two earthquakes (one mentioned above, occurring at the western end of the Darfield surface rupture) and another on March 30th, 1992 are the only exceptions, both being thrust earthquakes.

We have calculated the Coulomb Static Stress Changes caused by the occurrence of the Darfield earthquake and the February Christchurch earthquake. The calcula-
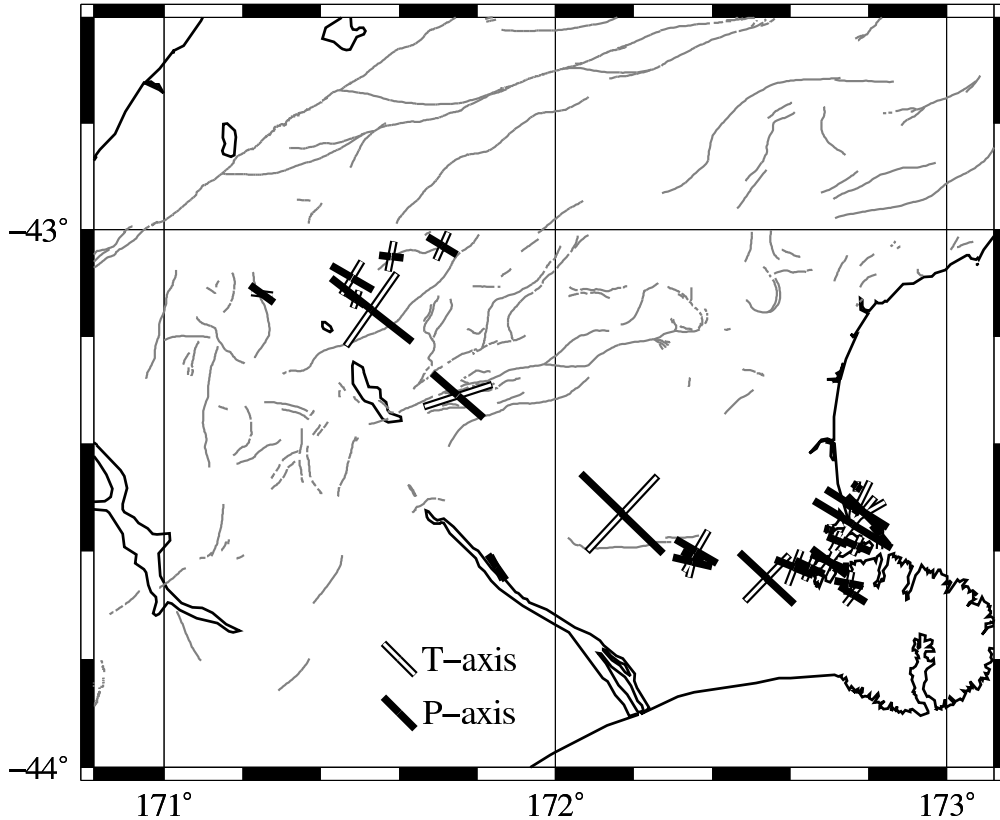
Figure 5.7: P- and T-axis (see key for symbols) of all earthquakes from 01/01/1976 till 01/09/2013 (last access to the catalogue). A list of all the earthquakes can be found in Table A4.1 in Appendix A4.

tions have been made by S. Steacy (2012; personal communication). The Coulomb stress tensor was computed by a six fault slip model for the Darfield earthquake (Beavan et al. 2010) and a single fault model for the Christchurch earthquake (Beavan et al. 2011). The perturbation was resolved onto 3D optimally oriented planes assuming an effective coefficient of friction of 0.4. We used regional horizontal stress orientations of $\sigma_1 = 115°$; $\sigma_3 = 25°$ with σ_2 vertical (Sibson et al. 2011) and assumed compressive stress values of $\sigma_1 = 10\text{MPa}$, $\sigma_2 = 0.5\text{MPa}$, and $\sigma_3 = 0.1\text{MPa}$; the near equal values of the latter are consistent with observations of both strike-slip and reverse faulting in the region. A separate calculation of the static stress changes has been also made for the Alpine fault.

Figure 5.8a shows the static stress changes caused by the Darfield earthquake along with its aftershocks. We see that all the earthquakes occur primarily in areas

of stress increase (77% of the reliably relocated earthquakes). We also see that the location of the Christchurch earthquake (yellow star) lies within a region of stress increase. As mentioned before, this suggests that it was triggered by the Darfield earthquake due to the stress increase. It is important to note that the stress calculation in this study were made using the slip model of Beavan et al. (2010). However, there are a range of other model for the Darfield earthquake (e.g. Stramondo et al. 2011; Elliott et al. 2012), highlighting the complexity of the rupture. Therefore small changes in the static stress change field are expected whether we use one slip model instead of the other. However, despite this diversity, there is an common agreement that the Christchurch epicentral area was brought closer to failure by the Darfield earthquake.
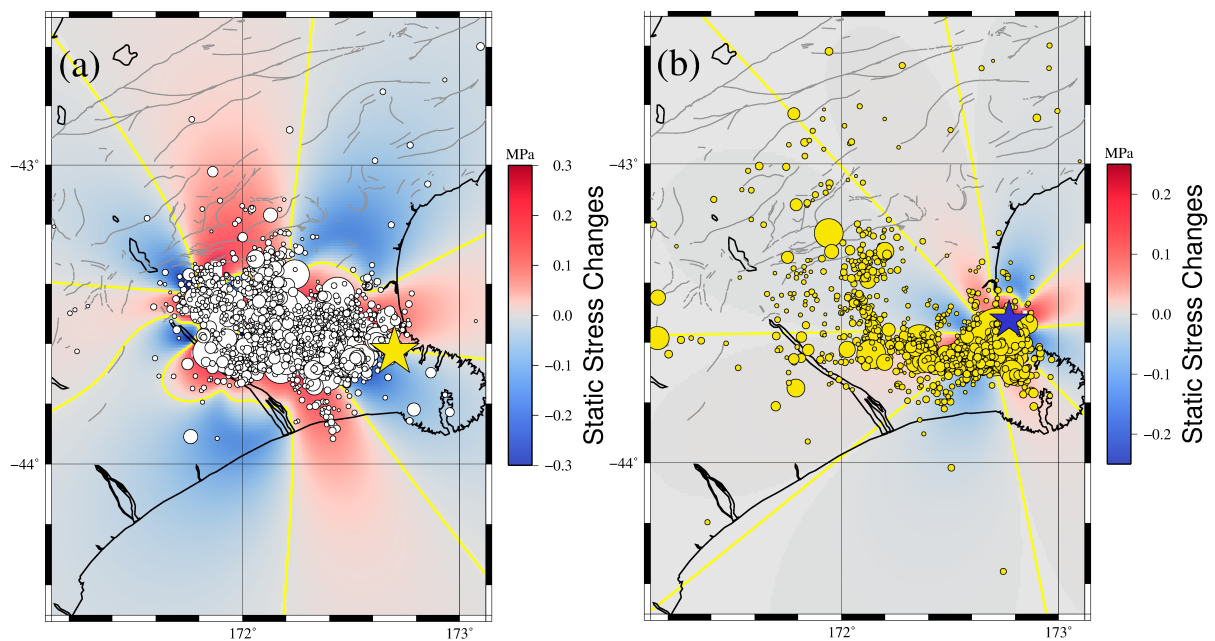
Figure 5.8: (a) Static stress changes caused by the $M_L7.0$ September 3rd, 2010 Darfield earthquake. The white dots show the seismic activity from September 3rd, 2010 till February 20th, 2011 (day before the Christchurch earthquake). The yellow star shows the location of the epicentre of the Christchurch earthquake. (b) Static stress changes caused by the $M_L6.3$, February 21st, 2011 Christchurch earthquake. Yellow dots show the seismic activity from February 21st, 2011 till December 22nd, 2011 (day before the beginning of the off-shore Christchurch swarm). The blue star shows the zone where the largest earthquakes of the December 2011 earthquakes swarm occurred. In both figures, the yellow line is the zero contour of the static stress changes field.

Figure 5.8b shows the static stress changes caused by the Christchurch earthquake along with its aftershocks. Again, we observe that the aftershocks occur primarily in areas of stress increase (76% of the reliably relocated earthquakes) as well as the December 2011 off-shore Christchurch swarm (blue star), which also occurs in a region of stress increase (84 % of the reliably relocated earthquakes after December 22nd, 2011). Interestingly, all earthquakes from the swarm are located south of the northern edge of the bump of stress increase induced by the Christchurch earthquake (see Figure A4.3 in Appendix A4), which marks a transition from stress increase to stress shadow. However, that region was previously under a stress increase caused by the Darfield earthquake. The lack of seismic activity above that limit shows that the occurrence of the Christchurch earthquake modified the regional stress field, affecting the location of the December 2011 swarm. We also observe that the reactivated cluster east of the Darfield earthquake surface rupture coincides with an region of stress increase caused by the occurrence of the Christchurch earthquake.

5.7   Discussion

The Canterbury Plains was widely considered to be a seismically quiet region. However, the occurrence of the 2010-2011 earthquakes sequence has indicated that this region has significant potential to release stresses accumulated from the action of the regional stress field at low strain rate (between 0.0 and 0.25 ppm/year; Beavan & Haines 2001). Before these earthquakes, the seismic hazards were highly under estimated because few active faults had been identified in this region prior the main shock. It is well established that in numerous regions, faults do not show any or little surface expression, explaining why structural studies are precluded (Sieh 1981). As argued by England & Jackson (2011), regions of "uncharted seismic risk" should be examined, and both from a geological and geophysical perspective, in order to assess the potential of a region to experience a large earthquake, especially when it

is located near a major plate boundary.

When we have attempted to look for precursors of the 2010-2011 earthquakes sequence in the seismic activity, we did not observed any direct precursors. Nevertheless, there is a hint of migration in the seismic activity toward the epicentral area of the Darfield earthquake. It suggests that the stress is progressively transferred from the plate boundary toward the plate interior over a long time-scale (maybe hundreds of years). However, further investigations are necessary to assess the validity of this observation and, once again, this is only relevant for seismic hazards if there are faults identified as capable of producing large earthquakes.

The 2010-2011 New-Zealand earthquake sequence provide another well documented example of how the spatial pattern of static stress changes influences the location of the seismic activity (e.g. King et al. 1994 for the Landers earthquake). Indeed, the occurrence of the Darfield earthquake has induced a clear eastward migration of the earthquakes. This migration correlates with the eastern lobe of stress increase caused by the main shock, triggering the Christchurch earthquake. Interestingly, we observe that the occurrence of the latter modifies the pattern of stress changes, sufficiently to affect the location of the seismic activity. The pattern confines the earthquakes in a narrow region around Christchurch. We observe a reactivation of the "blind faults" in the western lobe of stress increase and we observe that the December 2011 earthquake swarm terminated at the limit between stress increase and stress shadow. We therefore show clearly in this study how well the static stress changes impact on the seismic activity following the Darfield earthquake.

We have also calculated how this earthquake sequence has changed the stress on the Alpine fault. This fault is believed to have accumulated about 480 km of slip since the late Jurassic (Wellman 1955). The larger earthquakes (M_w >5.0) in New Zealand since 1976, show a clear seismic gap on the fault segment closest to Darfield-Christchurch (see Figure 5.9). Since 1901 there has been a seismic station

in Christchurch and the occurrence of any significant earthquake since then would have been recorded. Paleoseismic studies carried out in this gap suggests that the last earthquake occurred here nearly 600 years ago (Adams 1980). The stress on the Alpine fault, which coincides with the north-western lobe in Figure 5.8a, is now enhanced by about 0.01-0.02 MPa, a level sufficient to trigger earthquakes (Harris 1998; Stein 1999). In fact, a stress change of about 0.01 MPa is believed to have triggered the M_w 8.7 2005 Nias, Sumatra earthquake (Nalbant et al. 2005). Recent example from the Sumatra subduction zone (Delescluse et al. 2012) show that the influence of stress changes can be seen several years after the occurrence of the main shock. It is therefore important to provide a greater emphasis on this seismic gap that is on a major plate boundary.

5.8 Conclusions

Using P-wave arrival times reported by ISC between 01 January 1964 and September 2013, we have relocated earthquakes in a 1° radius region centred about the epicentre of the Darfield earthquake. We first observe that even after relocation, the seismic activity is still very low within the Canterbury Plains so that there is a very large quiet region close to a major plate boundary. From 1970, we observe a progressive migration of the seismic activity toward the epicentral area of the Darfield earthquake, suggesting that the region experiences a long-term west to east stress transfer. Once the Darfield earthquake triggers the whole 2010-2011 earthquake sequence, we observe a eastward progression of the seismic activity that correlates very well with region of stress increase caused by the Darfield earthquake, which also triggered the February 2011, Christchurch earthquake. The latter modified in turn the migration of the seismic activity notably by re-activating "blind faults" between the Port Hills Fault and the Greendale Fault and by stopping the December 2011 earthquake swarm at the limit between a region of stress increase and stress
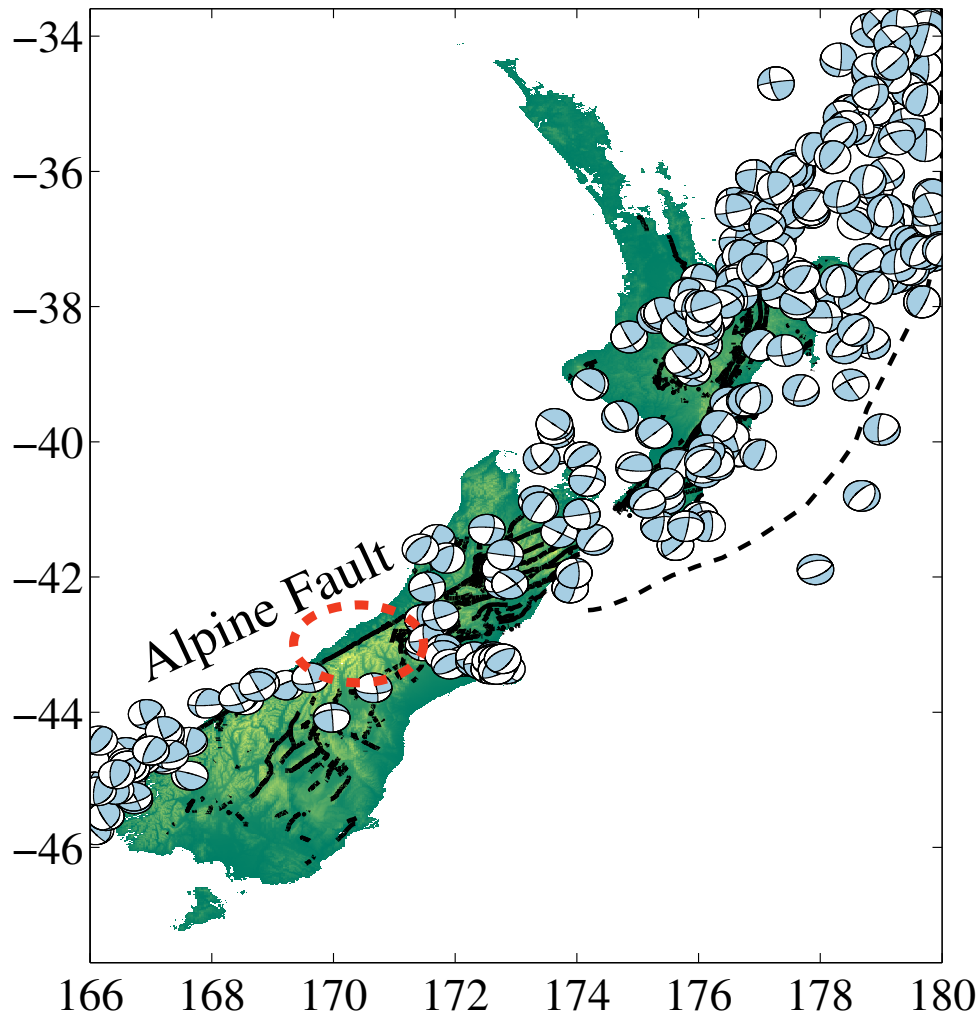
Figure 5.9: Plot of the 262 CMT mechanisms available from 01/01/1976 till 01/07/2013 for the whole New-Zealand region. The red ellipse shows a seismic gap near the region of Darfield and which was brought closer to failure by the 2010-2011 New-Zealand earthquakes sequence.

shadow. We also observe that the whole sequence has increased the stress in the southern region of the Canterbury Plains even though no known faults have been mapped. Specific calculations on the Alpine Fault have shown that the effect of the Canterbury Plains sequence is to increase the stress by 0.01 MPa on the seismic gap observed on the Alpine Fault for more than 600 years.

This study have illustrated the two important aspects on seismic risk debated

between England & Jackson (2011) and McCloskey (2011). Consequently, the fact that the stress has increased in the southern part of the Canterbury Plains, where no faults have yet been recognised, might not be irrelevant. The case of the Darfield earthquake has demonstrated that this should not be neglected because the seismic risk in that region might be uncharted. In addition, the 2010-2011 earthquake sequence brought a well known active fault closer to failure, where large destructive earthquakes could take place and that requires careful monitoring since we know its potential risk. Therefore, these two aspects of seismic risks are significant and neither should be overlooked because the two types can be together present, as it is the case in New-Zealand.

Chapter 6

Conclusion and Perspectives

We have studied the rupture history of the September 28, 2004, M_w6.0, Parkfield earthquake from two different perspectives, first by using kinematic inversions and second by using dynamic inversions. In both cases, the inversion were carried out using a recently developed method that uses elliptical patches to describe the slip history in the case of kinematic inversion or using the stress and frictional properties of the fault in the case of the dynamic inversion.

To obtain the source process of the Parkfield earthquake using a kinematic approach, we have carried out a set of 12 inversions, each of them including different *a-priori* conditions that one can have on the rupture history of this earthquake. By doing so, we have investigated the non-uniqueness associated with the kinematic inversion. Despite this non-uniqueness, we have been able to identify recurrent features, regardless of the *a-priori* conditions used for the different inversions. Because of the recurrence of those features, they define the robust characteristics of the source process of the Parkfield earthquake. Although the 12 obtained rupture models are equally plausible for explaining the rupture process of the Parkfield earthquake, we have chosen a preferred one based on external criteria such as the presence of robust features, a final seismic moment that does not exceed $\pm15\%$ of the CMT value and the fit to a set of analog stations that have recorded the earthquake but were not used during the inversions. The preferred model has a slip history distributed over two distinct ellipses, both rupturing at sub-shear speed. The final slip distribution of the preferred model is in good agreement with the large earthquakes ($M_w > 3$)

from 1984 to 2004. They are mainly located at the edges of the slip patches suggesting that those regions were locked and were accumulating stress. We have also compared the final slip distribution with the aftershocks of the Parkfield earthquake. We observe that the inversion has put the two slip patches below 5 km depth, a level delineated by small aftershocks and that is believed to delimit a creeping layer above it and a locked zone below it. The distribution of large aftershocks ($M_w > 3$) shows that they are located at the edges of the slip patches, where we observe a transition from large-slip to no slip, a behaviour that has been observed for other earthquakes. This evidence suggests that we have been able to retrieve the robust features of the rupture process of the Parkfield earthquake.

To assess the capability of our inversion method in retrieving the rupture process of an earthquake, we subjected it to synthetic tests with the aim of obtaining the rupture source process from synthetic data generated by artificially created earthquakes. As argued for the inversions of the Parkfield earthquake, the tests show that our method is suited to infer the robust features of an earthquake. In the case of a complex artificial earthquake, the inversions obtain low-frequency filtered versions of the input rupture models. We have also analysed the behaviour of the Neighbourhood Algorithm (NA) in its search for the optimal solution. We see that the convergence of the NA is mostly controlled by the space-time location of the rupture front, telling us that the fit of the phase is what it is primarily sought by the inversion algorithm. Only later in the inversion, the NA shows a sensitivity to the fit in amplitude. To further investigate the non-uniqueness of kinematic inversions, we have investigated how the data processing done prior to the inversions can affect the results. In particular, we show that our kinematic inversion method is not very sensitive to high-frequencies (above 0.5 Hz) contained in the signal, which why the inversion scheme is better suited to obtain the large scale robust features of an earthquake rupture history. We have also looked at the influence of the time-window for the waveforms that is used during the inversion. We show that the

104

results are affected by the progressive arrival of P, S and Rayleigh waves emitted during the rupture process and that the rupture model retrieved by the inversion is consequently highly sensitive to the content of information provided to the inversion algorithm.

We have then looked at the rupture process of the 2004 Parkfield earthquake from a dynamic approach. First, we have implemented a more realistic modelling of the stress and frictional properties on the fault plane by incorporating an elliptical-shaped distribution of the parameter S inside each elliptical patch, with S controlling the ratio of strength over stress drop. The maximum rupture resistance is located at the centre of the ellipse and the edges are therefore relatively weaker compared to it. We have then carried out two synthetic tests to investigate the performances of the dynamic inversion method. We show that, in both cases, it is capable of retrieving a slip history in agreement with the input model. However, the solution is highly non-unique. There exists a range of combinations of dynamic parameters that are significantly different to the one used to create the input model but that can produce a rupture process similar to the original one. We argue that a detailed investigation of the parameter-space is therefore required if one wants to obtain a reliable estimate of the stress and frictional properties of the fault plane. The full dynamic inversion for the rupture process of the 2004 Parkfield earthquake has led to a rupture process similar to those obtained by kinematic inversions. The rupture occurs on a single 4 km wide ellipse, elongated along strike with a relatively constant rupture speed of 3 km/s. The value for κ (ratio of the available strain and the energy release rate) is 1.40, in agreement with other studies and compatible with a rupture at sub-shear speed. We have also determined the value of R_c/R_a (ratio of the critical size of the initial asperity and the actual size used in the inversion) to be 1.25. Along with a value of S of 0.7, it would suggest, by interpolating the results from Das & Aki (1977a), that the rupture speed is between $\frac{3}{4}c_r$ and c_r, which is in good agreement with the the rupture speed obtained by the dynamic inversion. Fixing

the geometry of the rupture area using that obtained from the dynamic inversion, we have investigated the distribution of rupture models inside the parameter-space using a Monte-Carlo method. To obtain a simple visualisation of the entire space, we have reduced it into a 3-D space defined by the three non-dimensional parameters *kappa*, S and R_c/R_a. We show that rupture models inside this space are distributed according to the average rupture speed and the seismic moment. Consequently, we observe a specific region into that 3-D space inside which the average rupture speed and the final seismic moment are in agreement with what is observed for the rupture process of the Parkfield earthquake.

Using the Fixed-Geometry Dynamic Inversion (FGDI) method, we have investigated the transition from a kinematic rupture model to a dynamic rupture model. The aim was to see if we could obtain a set of dynamic parameters that can reproduce our preferred kinematic rupture model, which would therefore ensure its reliability. We first show, using a Monte-Carlo exploration, that we cannot reproduce a dynamic rupture model similar to the kinematic rupture model while fitting the strong-motion data at the same time. But, because we have shown that our kinematic inversion method is more suited to retrieve the robust features of a rupture process, we have then performed a FGDI in which the two distinct ellipses are connected together. The connection is built using a new approach that uses a b-spline curve to define the rupture area on the fault plane, thus smoothly connecting the two ellipses while keeping their geometry almost unchanged. In this case, we are able to find a set of dynamic parameters agreeing with that obtained from the dynamic inversion and that produces a rupture history similar to the kinematic rupture model. The low slip amplitude inside the bridge in between the two ellipses could explained why the kinematic inversion using elliptical patch did not show this region.

This work on kinematic and dynamic inversions has opened perspectives for further improvements, especially on the methodology. All the inversions were carried

out using a 1-D velocity structure. However, it is well established that there is a strong contrast of velocity structure from the north-east and south-west side of the San Andreas Fault at the region of Parkfield (Thurber et al. 2003). An obvious improvement of our inversion method will be to enable handling of a more complex velocity structure. It could simply use a different 1-D velocity structure for each side of the fault but it could also use a different 1-D velocity structure for each station, which would account for site effects. We have also argued that part of the misfit observed during the kinematic and dynamic inversions were caused by fault-zone trapped waves. It would therefore be interesting to develop a forward model that can account for those waves and thus produce more realistic strong ground motion. In this study, we have used the NA to search for the optimal solution but it would be interesting to investigate the performance of other inversion algorithms. For instance, the recent development of an algorithm using a neural network to invert for focal mechanism (Käufl et al. 2014) is one of the possibilities that we could investigate. During the dynamic inversions, we have also started to develop a new approach to model the stress and frictional properties of the fault plane that uses b-spline curve. This is an interesting approach because it keeps the number of parameters low whilst being more flexible than the elliptical sub-fault approximation. It could even be developed further with the implementation of bi-harmonic spline interpolation that can create an interpolated surface, which could be for instance the strength field on the fault plane, from a set of unevenly distributed points. It would allow for including higher variability of the field that we are trying to model (strength, stress) while keeping the number of parameter low and being intrinsically smooth. Also the fact that it uses unevenly spaced points could be used to force the inversion to focus on region of the fault where the resolution is believed to be better.

Some aspects of seismic hazard were also studied, with the investigation of the 2010-2011 earthquake sequence following the occurrence of the 2010, $M_w 7.1$,

Darfield, New-Zealand earthquake. First earthquakes in the vicinity of the epicentral area of the Darfield earthquake from January 1964 till September 2013 were relocated. Looking at the seismic activity from 1964 to 2010, it shows that the Canterbury Plains remain seismically quiet even after the relocation of earthquakes. Although there was no clear precursors of the Darfield earthquake, we however observe a hint of migration of the seismic activity toward the future epicentre of the Darfield earthquake that could relate to a progressive stress transfer from the plate boundary to the plate interior. Because this migration is very weak, it would require further investigation to assess its plausibility. Following the occurrence of the Darfield earthquake, the seismic activity shows a clear migration to the east, enhanced by the occurrence of the February 2011 $M_w6.3$ Christchurch earthquake, and by the earthquake swarm off shore of Christchurch in December 2011. Using calculation of the static stress changes caused by the Darfield earthquake and then the Christchurch earthquake, we show that this migration occurs in regions of positive static stress changes (i.e. region brought closer to failure). We also show that the occurrence of the Christchurch earthquake has modified the static stress changes pattern in the region significantly enough to slightly change the direction of the migration of the seismic activity. Those calculations also show that some portions of the southern part of the Canterbury Plains, where the seismic risk is likely to be uncharted, have been brought closer to failure by the occurrence of the Darfield and Christchurch earthquake. We also show that a portion of the Alpine Fault, which is a major plate boundary, exhibits a large seismic gap that is also brought closer to failure by the 2010-2011 earthquake sequence.
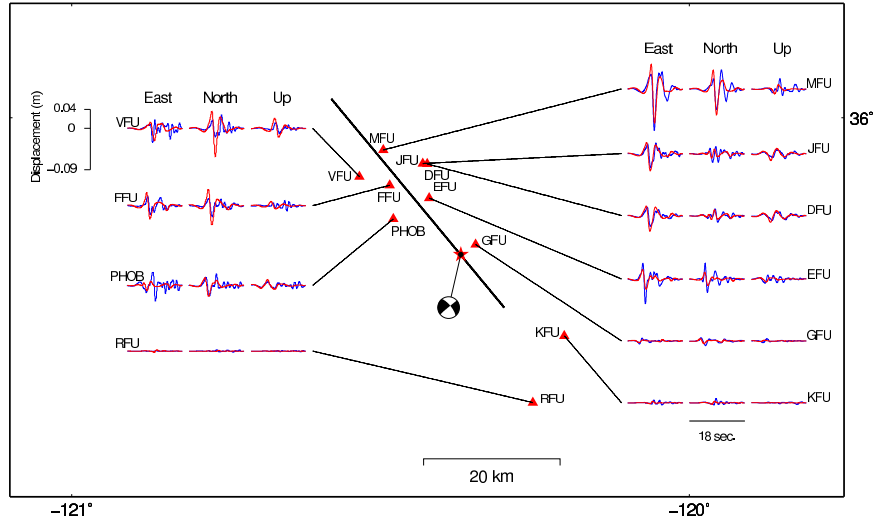
The entire earthquake sequence demonstrates the high degree of interaction between earthquakes. One explanation for the interaction mechanism is poroelastic triggering. It would therefore be interesting to see if this mechanism could explain the triggering of the Christchurch earthquake by the Darfield earthquake, in a similar fashion to what has been observed for the 9-22 January 2008 Nima-Gaize earth-

quakes in Tiber (He & Peltzer 2010). Because liquefaction effects in the Canterbury Plains, New-Zealand, were observed subsequent to the Darfield and Christchurch earthquake (e.g. Orense et al. 2011), this suggests an abundant presence of fluids. A long-term poroelastic triggering of the Christchurch earthquake caused by the Darfield earthquake could be a possibility.
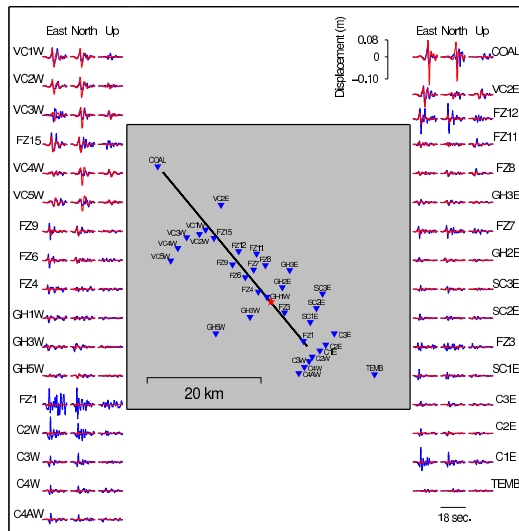
Appendices

A1   Appendices of Chapter 2

Inversion 1

(**a**): Comparison of the solution seismograms from Inversion 1 with the observed data at the digital stations. The thick black line shows the modelled fault trace. For each station, the observed seismograms are in blue and the solution seismograms are in red.

(**b**): Comparison of the solution seismograms from Inversion 1 with the observed data at analog stations locations. the thick black line shows the modelled fault trace. For each station, the observed seismograms are in blue and the solution seismograms are in red.
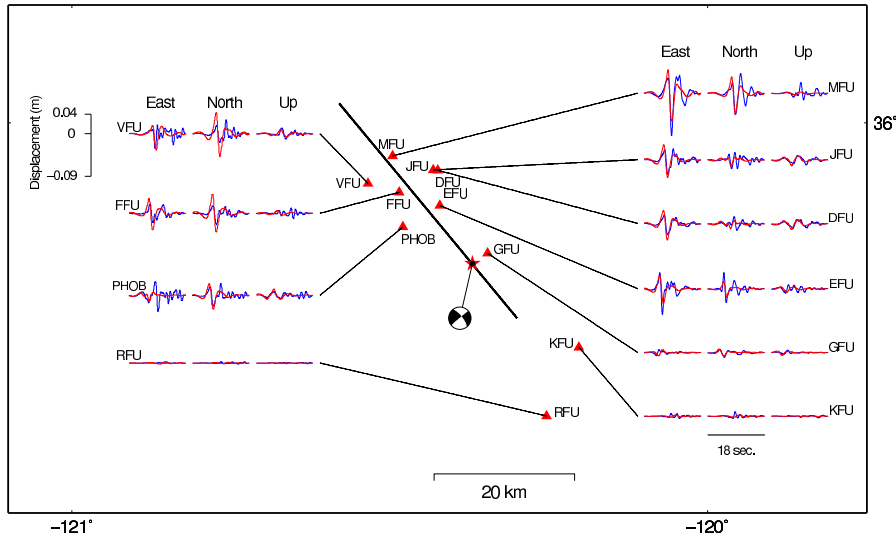
(**c**): Summary of all parameters describing Inversion 1, associated with the range of values for each parameter used during the inversion.

Parameter	Min. Value	Max. Value	Final Value
Ellipse1			
h_r	0.00	1.00	0.93
α_r	0.00	1.00	0.42
x_a (km)	2.00	20.0	17.35
x_b (km)	2.00	7.00	2.00
α (∘)	0.00	1.00	0.82
s1 (m)	0.00	1.00	0.76
v1 (km/s)	2.00	3.80	3.00
Ellipse2			
h_r	5.00	35.0	0.99
α_r	4.00	15.0	0.54
x_a (km)	2.00	20.0	4.91
x_b (km)	2.00	10.0	2.02
α (∘)	0.00	1.00	0.77
s2 (m)	0.00	1.00	0.43
v2 (km/s)	2.00	3.80	3.30

Inversion 2

(a): Comparison of the solution seismograms from Inversion 2 with the observed data at the digital stations. The thick black line shows the modelled fault trace. For each station, the observed seismograms are in blue and the solution seismograms are in red.
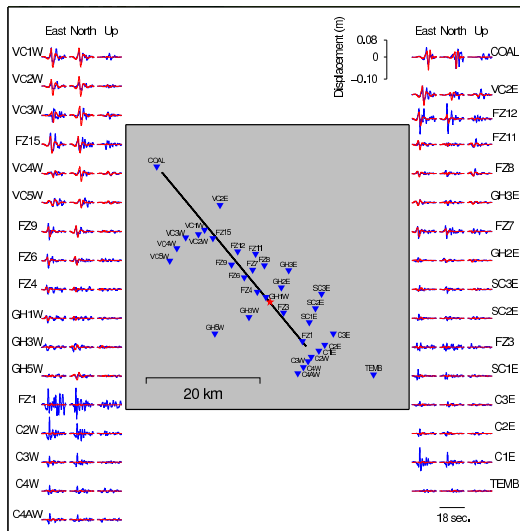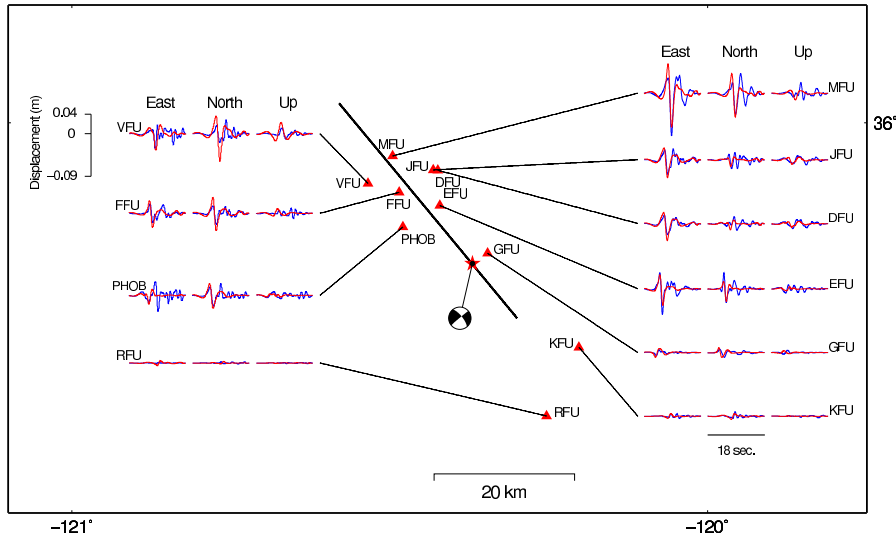

(b): Comparison of the solution seismograms from Inversion 2 with the observed data at analog stations locations. the thick black line shows the modelled fault trace. For each station, the observed seismograms are in blue and the solution seismograms are in red.

(c): Summary of all parameters describing Inversion 2, associated with the range of values for each parameter used during the inversion.

Parameter	Min. Value	Max. Value	Final Value
Ellipse1			
h_r	0.00	1.00	0.81
α_r	0.00	1.00	0.87
x_a	2.00	20.0	2.24
x_b	2.00	7.00	3.11
α	0.00	180.0	142.02
s1	0.00	1.00	0.56
v1	2.00	5.00	4.96
τ	0.20	2.00	1.18
rake	120.0	180.0	126.73
Ellipse2			
h_r	0.00	1.00	1.00
α_r	0.00	1.00	0.68
x_a	2.00	20.0	2.12
x_b	2.00	10.0	7.51
α	0.00	180.0	103.17
s2	0.00	1.00	0.98
v2	2.00	5.00	3.36
τ	0.20	2.00	0.54
rake	120.0	180.0	101.56

Inversion 3

(a): Comparison of the solution seismograms from Inversion 3 with the observed data at the digital stations. The thick black line shows the modelled fault trace. For each station, the observed seismograms are in blue and the solution seismograms are in red.
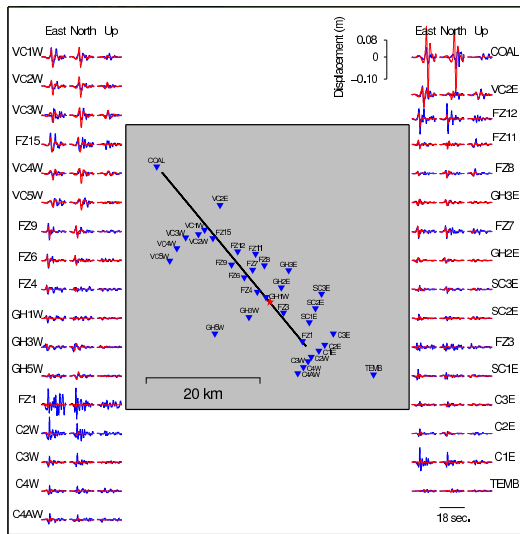

(b): Comparison of the solution seismograms from Inversion 3 with the observed data at analog stations locations. the thick black line shows the modelled fault trace. For each station, the observed seismograms are in blue and the solution seismograms are in red.
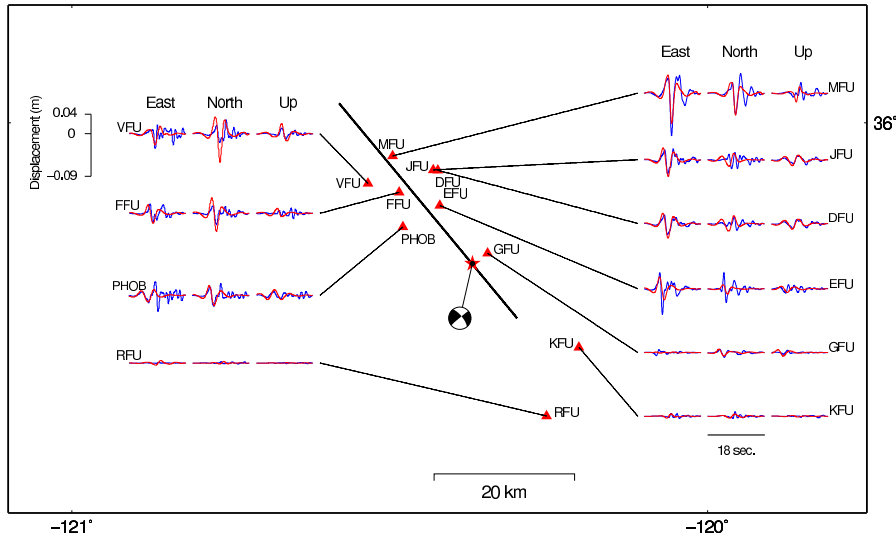
(c): Summary of all parameters describing Inversion 3, associated with the range of values for each parameter used during the inversion.

Parameter	Min. Value	Max. Value	Final Value
Ellipse1			
h_r	0.00	1.00	0.26
α_r	0.00	1.00	0.60
x_a	2.00	20.0	2.39
x_b	2.00	7.00	4.56
α	0.00	180.0	60.32
s1	0.00	1.00	0.50
v1	2.00	5.00	2.15
τ	0.20	2.00	0.36
rake	120.0	180.0	179.13
Ellipse2			
x_0	5.00	35.0	5.05
y_0	4.00	15.0	7.33
x_a	2.00	20.0	16.00
x_b	2.00	10.0	2.82
α	0.00	180.0	174.9
s2	0.00	1.00	0.58
v2	2.00	5.00	3.51
τ	0.20	2.00	0.87
rake	120.0	180.0	146.48

Inversion 4

(a): Comparison of the solution seismograms from Inversion 4 with the observed data at the digital stations. The thick black line shows the modelled fault trace. For each station, the observed seismograms are in blue and the solution seismograms are in red.
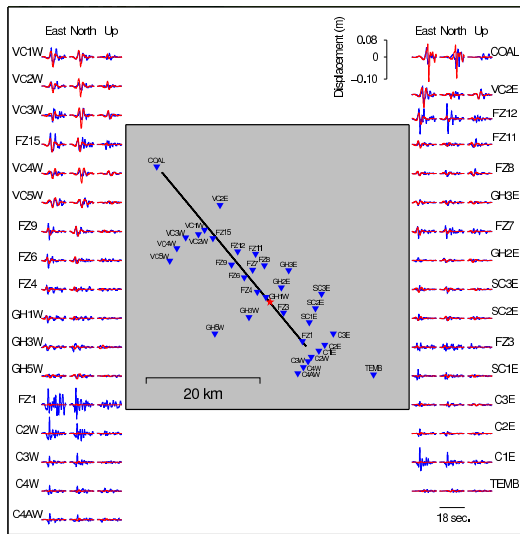

(b): Comparison of the solution seismograms from Inversion 4 with the observed data at analog stations locations. the thick black line shows the modelled fault trace. For each station, the observed seismograms are in blue and the solution seismograms are in red.
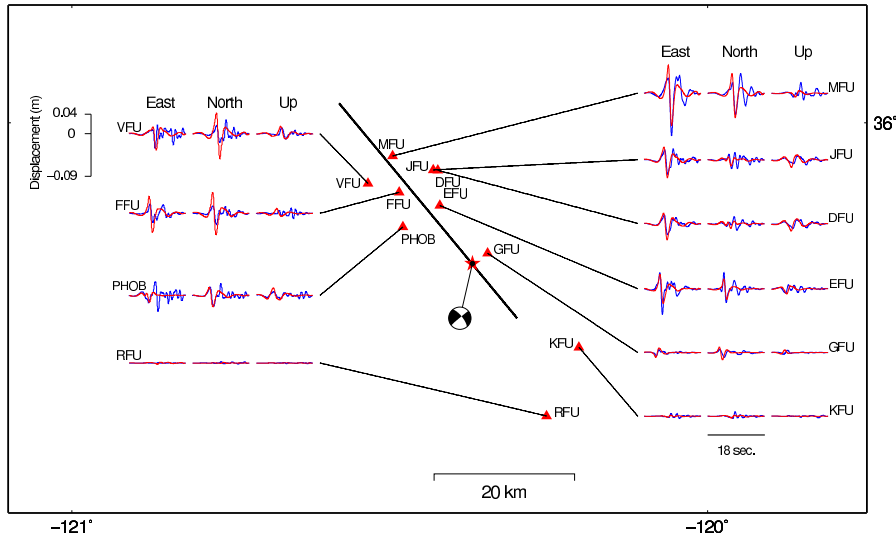
Parameter	Min. Value	Max. Value	Final Value
Ellipse1			
h_r	0.00	1.00	0.37
α_r	0.00	1.00	0.44
x_a	2.00	20.0	18.09
x_b	2.00	7.00	3.56
α	0.00	1.00	0.89
s1	0.00	1.00	0.31
v1	2.00	3.80	3.76
τ	0.20	2.00	1.25
rake	120.0	180.0	136.28
Ellipse2			
h_r	0.00	1.00	0.41
α_r	0.00	1.00	0.61
x_a	2.00	20.0	8.08
x_b	2.00	10.0	2.67
α	0.00	1.00	0.87
s2	0.00	1.00	0.45
v2	2.00	3.80	2.98
τ	0.20	2.00	0.48
rake	120.0	180.0	173.14

(c): Summary of all parameters describing Inversion 4, associated with the range of values for each parameter used during the inversion.

Inversion 5

(a): Comparison of the solution seismograms from Inversion 5 with the observed data at the digital stations. The thick black line shows the modelled fault trace. For each station, the observed seismograms are in blue and the solution seismograms are in red.
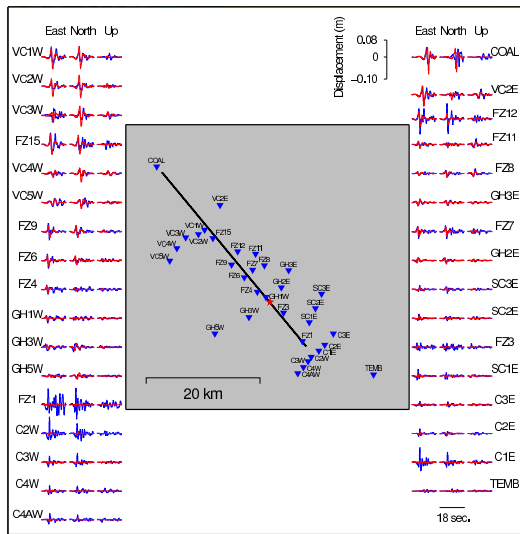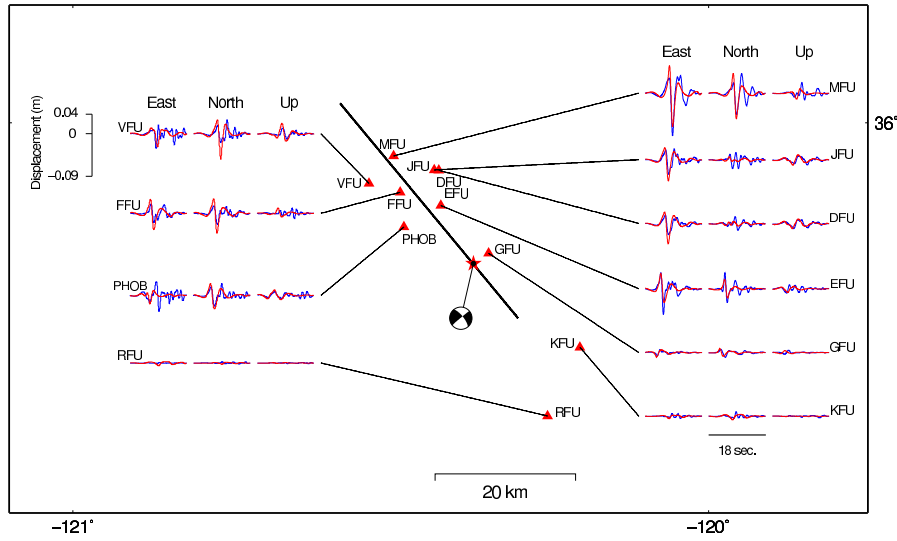

(b): Comparison of the solution seismograms from Inversion 5 with the observed data at analog stations locations. the thick black line shows the modelled fault trace. For each station, the observed seismograms are in blue and the solution seismograms are in red.

(c): Summary of all parameters describing Inversion 5, associated with the range of values for each parameter used during the inversion.

Parameter	Min. Value	Max. Value	Final Value
Ellipse1			
h_r	0.00	1.00	0.27
α_r	0.00	1.00	0.56
x_a	2.00	20.0	4.72
x_b	2.00	7.00	5.07
α	0.00	1.00	0.61
s1	0.00	1.00	0.19
v1	2.00	3.80	2.46
Ellipse2			
x_0	5.00	35.0	17.99
y_0	4.00	15.0	8.82
x_a	2.00	20.0	9.36
x_b	2.00	10.0	3.02
α	0.00	1.00	0.00
s2	0.00	1.00	0.57
v2	2.00	3.80	3.01

117

Inversion 6

(a): Comparison of the solution seismograms from Inversion 6 with the observed data at the digital stations. The thick black line shows the modelled fault trace. For each station, the observed seismograms are in blue and the solution seismograms are in red.
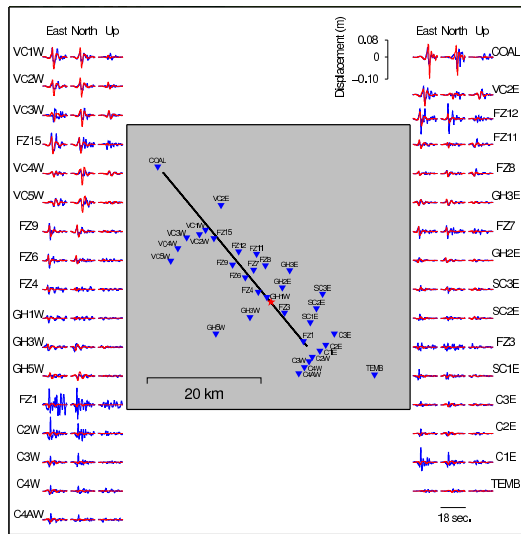
(b): Comparison of the solution seismograms from Inversion 6 with the observed data at analog stations locations. the thick black line shows the modelled fault trace. For each station, the observed seismograms are in blue and the solution seismograms are in red.
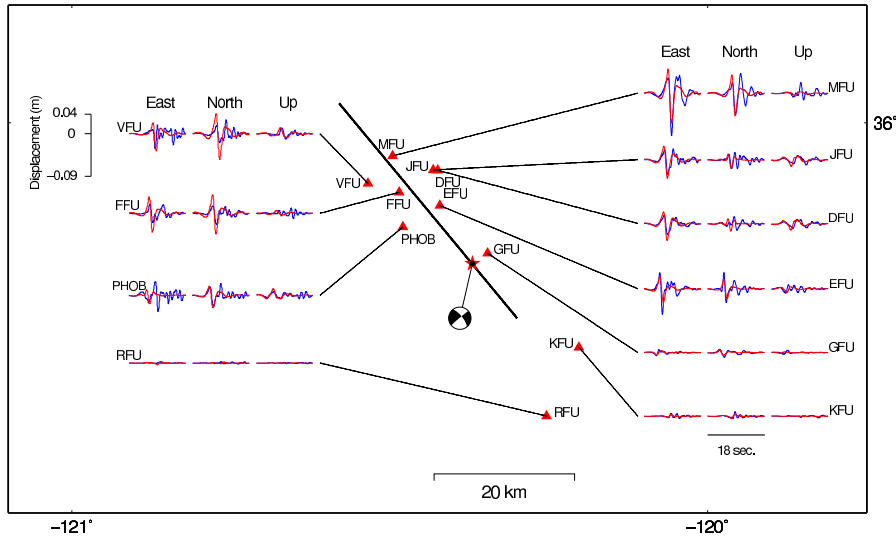
Parameter	Min. Value	Max. Value	Final Value
Ellipse1			
h_r	0.00	1.00	0.63
α_r	0.00	1.00	0.52
x_a	2.00	20.0	3.18
x_b	2.00	7.00	3.34
α	0.00	180.0	54.34
s1	0.00	1.00	0.88
v1	2.00	5.00	2.22
Ellipse2			
x_0	5.00	35.0	17.06
y0	4.00	15.0	13.02
x_a	2.00	20.0	6.01
x_b	2.00	10.0	2.29
α	0.00	180.0	17.06
s2	0.00	1.00	0.92
v2	2.00	5.00	3.08

(c): Summary of all parameters describing Inversion 6, associated with the range of values for each parameter used during the inversion.

Inversion 7

(a): Comparison of the solution seismograms from Inversion 7 with the observed data at the digital stations. The thick black line shows the modelled fault trace. For each station, the observed seismograms are in blue and the solution seismograms are in red.

(b): Comparison of the solution seismograms from Inversion 7 with the observed data at analog stations locations. the thick black line shows the modelled fault trace. For each station, the observed seismograms are in blue and the solution seismograms are in red.
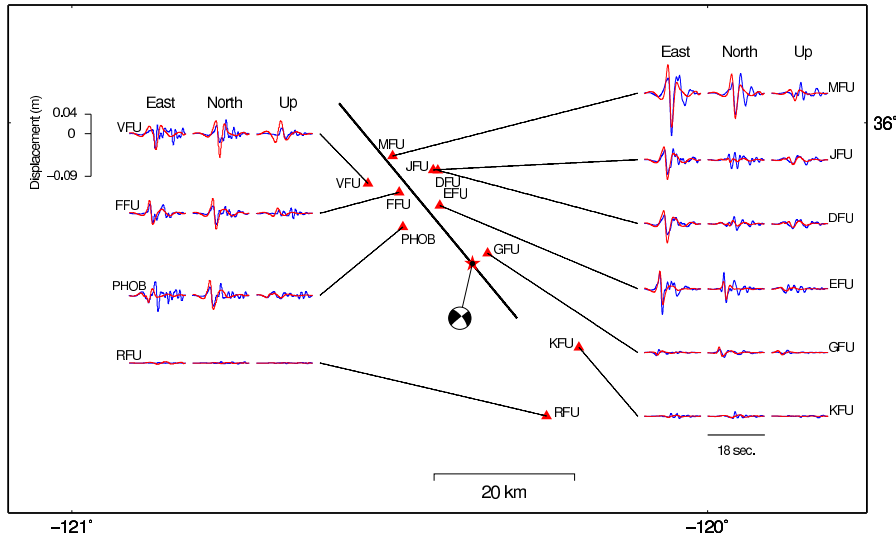
(c): Summary of all parameters describing Inversion 7, associated with the range of values for each parameter used during the inversion.
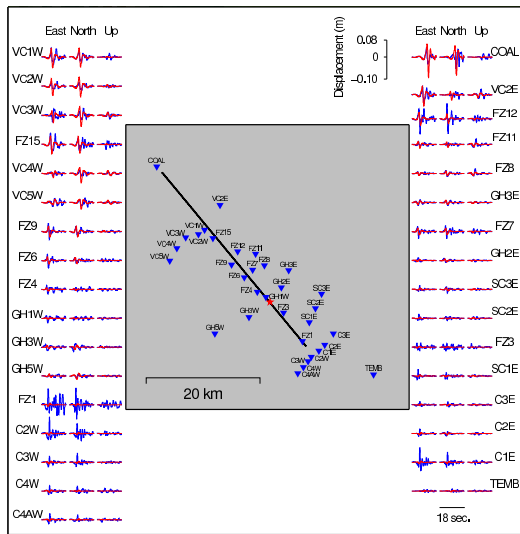
Parameter	Min. Value	Max. Value	Final Value
Ellipse1			
h_r	0.00	1.00	0.58
α_r	0.00	1.00	0.56
x_a	2.00	20.0	2.04
x_b	2.00	7.00	5.59
α	0.00	180.0	82.87
s1	0.00	1.00	0.27
v1	2.00	5.00	2.46
Ellipse2			
h_r	0.00	1.00	1.00
α_r	0.00	1.00	0.42
x_a	2.00	20.0	16.07
x_b	2.00	10.0	2.04
α	0.00	180.0	5.93
s2	0.00	1.00	1.00
v2	2.00	5.00	3.38

Inversion 8

(a): Comparison of the solution seismograms from Inversion 8 with the observed data at the digital stations. The thick black line shows the modelled fault trace. For each station, the observed seismograms are in blue and the solution seismograms are in red.
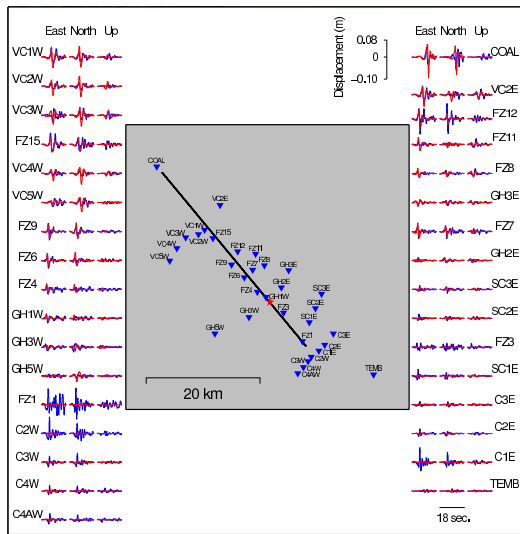

(b): Comparison of the solution seismograms from Inversion 8 with the observed data at analog stations locations. the thick black line shows the modelled fault trace. For each station, the observed seismograms are in blue and the solution seismograms are in red.
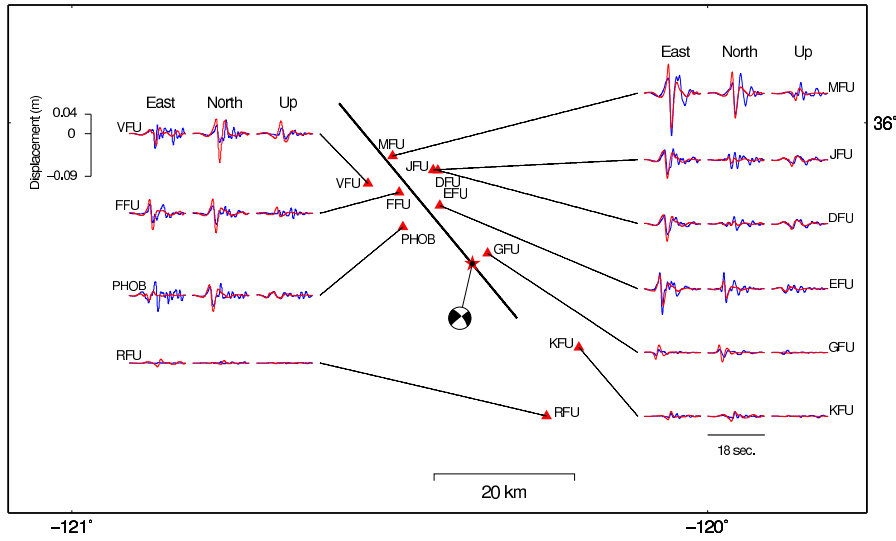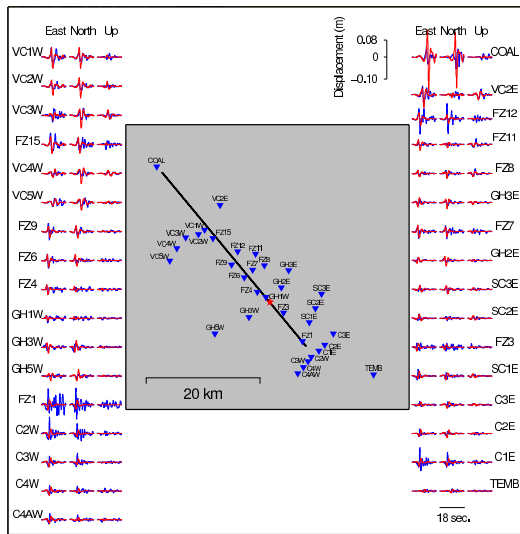
(c): Summary of all parameters describing Inversion 8, associated with the range of values for each parameter used during the inversion.

Parameter	Min. Value	Max. Value	Final Value
Ellipse1			
h_r	0.00	1.00	0.60
α_r	0.00	1.00	0.43
x_a	2.00	20.0	2.50
x_b	2.00	7.00	3.44
α	0.00	1.00	0.28
s1	0.00	1.00	0.69
v1	2.00	3.80	2.01
τ	0.20	2.00	0.32
rake	120.0	180.0	145.96
Ellipse2			
x_0	5.00	35.0	12.37
y_0	4.00	15.0	8.21
x_a	2.00	20.0	6.68
x_b	2.00	10.0	3.01
α	0.00	1.00	0.86
s2	0.00	1.00	0.99
v2	2.00	3.80	3.57
τ	0.20	2.00	1.00
rake	120.0	180.0	151.13

Inversion 9

(a): Comparison of the solution seismograms from Inversion 9 with the observed data at the digital stations. The thick black line shows the modelled fault trace. For each station, the observed seismograms are in blue and the solution seismograms are in red.

(b): Comparison of the solution seismograms from Inversion 9 with the observed data at analog stations locations. the thick black line shows the modelled fault trace. For each station, the observed seismograms are in blue and the solution seismograms are in red.
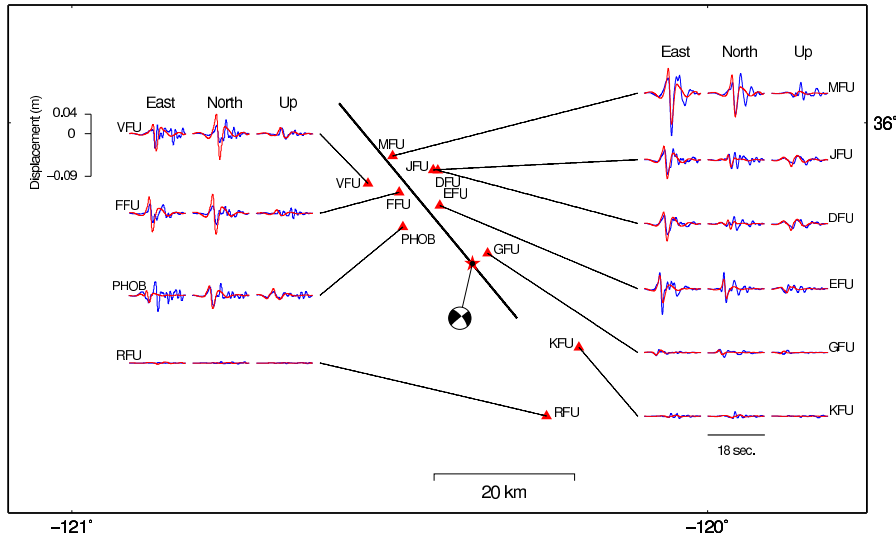
Parameter	Min. Value	Max. Value	Final Value
Ellipse1			
h_r	0.00	0.00	0.00
α_r	0.00	0.00	0.00
x_a	2.50	3.00	2.99
x_b	2.50	3.00	2.81
α	0.00	0.00	54.34
s1	0.40	1.00	0.74
v1	2.00	3.80	2.00
Ellipse2			
x_0	0.00	40.0	7.82
y_0	0.00	10.0	7.36
x_a	2.00	20.0	13.79
x_b	2.00	10.0	2.65
α	0.00	1.00	0.89
s2	0.00	1.00	0.92
v2	2.00	3.80	3.08

(c): Summary of all parameters describing Inversion 9, associated with the range of values for each parameter used during the inversion.

121

Inversion 10

(a): Comparison of the solution seismograms from Inversion 10 with the observed data at the digital stations. The thick black line shows the modelled fault trace. For each station, the observed seismograms are in blue and the solution seismograms are in red.
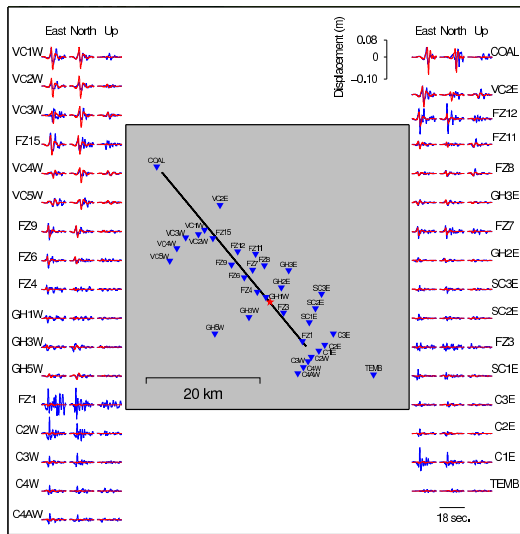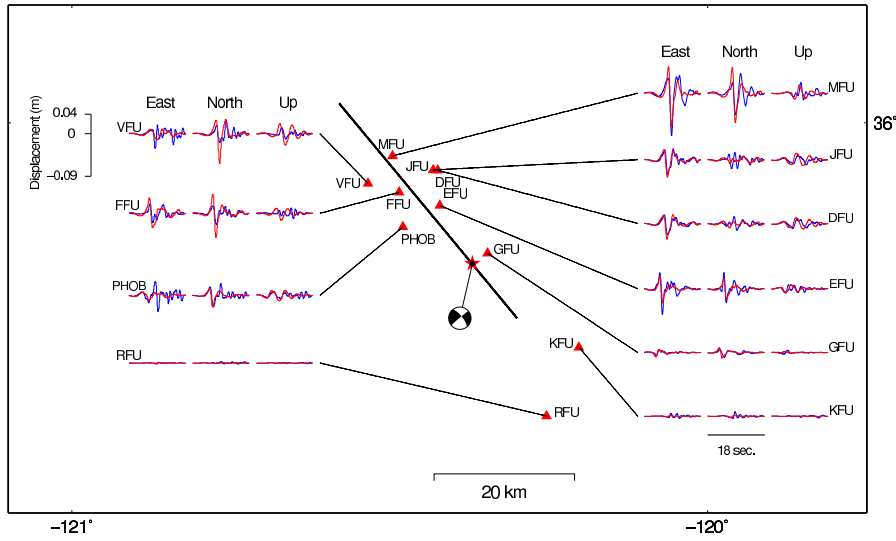

(b): Comparison of the solution seismograms from Inversion 10 with the observed data at analog stations locations. the thick black line shows the modelled fault trace. For each station, the observed seismograms are in blue and the solution seismograms are in red.

(c): Summary of all parameters describing Inversion 10, associated with the range of values for each parameter used during the inversion.

Parameter	Min. Value	Max. Value	Final Value
Ellipse1			
h_r	0.00	1.00	0.63
α_r	0.00	1.00	0.41
x_a	2.00	20.0	3.13
x_b	2.00	7.00	3.48
α	0.00	1.00	025
s1	0.00	1.00	0.42
v1	2.00	3.80	2.33
Ellipse2			
h_r	0.00	1.00	1.00
α_r	0.00	1.00	0.49
x_a	2.00	20.0	10.09
x_b	2.00	10.0	2.01
α	0.00	1.00	0.88
s2	0.00	1.00	0.82
v2	2.00	3.80	3.10

Inversion 11

(a): Comparison of the solution seismograms from Inversion 11 with the observed data at the digital stations. The thick black line shows the modelled fault trace. For each station, the observed seismograms are in blue and the solution seismograms are in red.
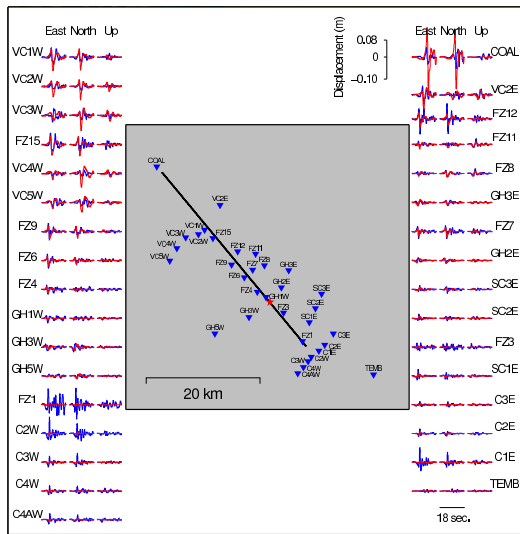

(b): Comparison of the solution seismograms from Inversion 11 with the observed data at analog stations locations. the thick black line shows the modelled fault trace. For each station, the observed seismograms are in blue and the solution seismograms are in red.
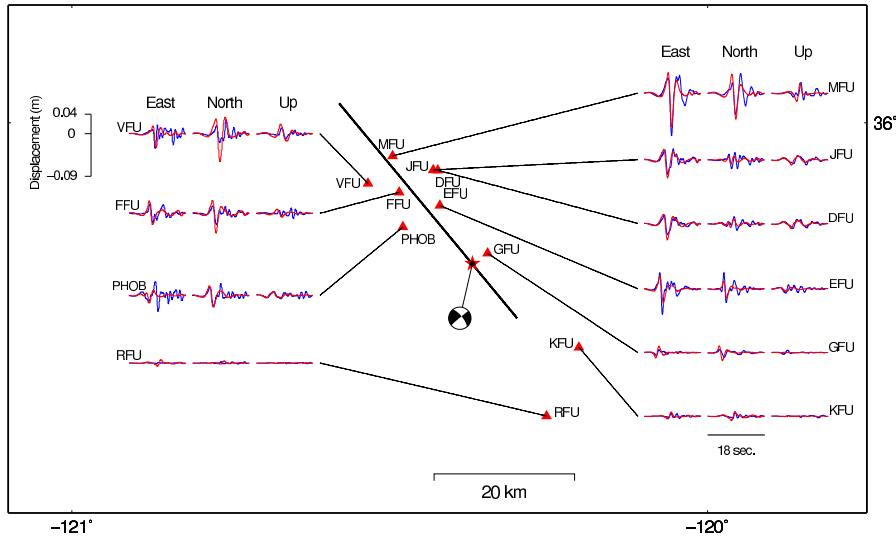
(c): Summary of all parameters describing Inversion 11, associated with the range of values for each parameter used during the inversion.

Parameter	Min. Value	Max. Value	Final Value
Ellipse1			
h_r	0.00	1.00	0.97
α_r	0.00	1.00	0.61
x_a	2.00	20.0	19.92
x_b	2.00	7.00	2.47
α	0.00	1.00	0.51
s1	0.00	1.00	0.30
v1	2.00	3.80	3.06
Ellipse2			
h_r	0.00	1.00	1.00
α_r	0.00	1.00	0.50
x_a	2.00	20.0	11.76
x_b	2.00	10.0	5.28
α	0.00	1.00	0.99
s2	0.00	1.00	0.30
v2	2.00	3.80	3.29

123

Inversion 12

(a): Comparison of the solution seismograms from Inversion 12 with the observed data at the digital stations. The thick black line shows the modelled fault trace. For each station, the observed seismograms are in blue and the solution seismograms are in red.
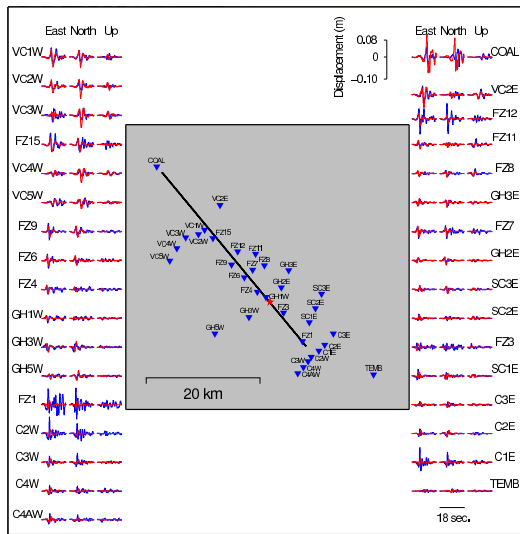

(b): Comparison of the solution seismograms from Inversion 12 with the observed data at analog stations locations. the thick black line shows the modelled fault trace. For each station, the observed seismograms are in blue and the solution seismograms are in red.

(c): Summary of all parameters describing Inversion 12, associated with the range of values for each parameter used during the inversion.

Parameter	Min. Value	Max. Value	Final Value
Ellipse1			
h_r	0.00	0.00	0.00
α_r	0.00	0.00	0.00
x_a	2.50	3.00	2.99
x_b	2.50	3.00	2.85
α	0.00	0.00	0.00
s1	0.40	1.00	0.61
v1	2.00	3.80	2.02
Ellipse2			
x_0	0.00	40.0	5.88
y_0	0.00	10.0	8.31
x_a	2.00	20.0	12.43
x_b	2.00	10.0	8.01
α	0.00	1.00	0.18
s2	0.00	1.00	0.30
v2	2.00	3.80	2.80
Ellipse3			
x_0	0.00	40.0	7.46
y_0	0.00	10.0	9.58
x_a	2.00	20.0	18.47
x_b	2.00	10.0	2.85
α	0.00	1.00	0.53
s3	0.00	1.00	0.47
v3	2.00	3.80	3.38

Table S1

Inversion	Set-up of the inversion	Summary of the rupture process
Inversion 1	Inversion using two connected ellipses; use of *a-priori* conditions; The rise-time and rake were not inverted	Misfit for the digital stations: 0.27; Misfit for the analog stations: 0.52; Moment: 1.78×10^{18} N.m; The rupture front propagates mostly in the forward direction at a speed of 3.00 km/s. A propagation of the rupture front in the backward direction is also observed for the first 1.7 sec. About 4.5 sec. after the start of the process, the high slip amplitude patch starts to break at a slightly higher rupture speed (3.30 km/s). The whole process is finished after 10.6 sec. of rupture.
Inversion 2	Inversion using two connected ellipses; No use of *a-priori* conditions; The rise-time and rake were inverted	Misfit for the digital stations: 0.30; Misfit for the analog stations: 0.54; Moment: 1.13×10^{18} N.m; No backward propagation is observed for this inversion. The rupture front reaches the peak of slip amplitude almost instantaneously (0.8 sec. after the start of the earthquake) at a really high rupture speed (4.96 km/s). This hypocentral patch finishes rupturing about 1.3 sec. later. The rupture front then propagates across the second ellipse at a slower speed (3.36 km/s). 5.8 sec. are needed by the rupture front to break all asperities.
Inversion 3	Inversion using two disconnected ellipses; No use of *a-priori* conditions; The rise-time and rake were inverted	Misfit for the digital stations: 0.28; Misfit for the analog stations: 0.50; Moment: 2.03×10^{18} N.m; We observed a bilateral propagation of the rupture front for about 2.5 sec., which is about the time taken to rupture the all hypocentral asperity (2.9 sec.). In this first part, the rupture starts at a low rupture speed of 2.15 km/s. Almost straight after that, the second ellipse start to rupture at higher speed (3.51 km/s). The whole process takes about 9.3 sec., when the rupture front reaches the end of the fault plane.
Inversion 4	Inversion using two connected ellipses; use of *a-priori* conditions; The rise-time and rake were inverted	Misfit for the digital stations: 0.30; Misfit for the analog stations: 0.59; Moment: 1.56×10^{18} N.m; For this inversion, we observed a bilateral propagation of the rupture front at a speed of 3.8 km/s. In the backward direction, the rupture front reaches the end of the fault about 3.6 sec. after the initiation of the earthquake. In the forward direction, the high amplitude slip patch starts to break after 5.0 sec and ruptures at a speed of 2.98 km/s. It takes 10.7 sec. for the whole process to be achieved.
Inversion 5	Inversion using two connected ellipses; use of *a-priori* conditions; The rise-time and rake were not inverted	Misfit for the digital stations: 0.28; Misfit for the analog stations: 0.53; Moment: 1.14×10^{18} N.m; The rupture front starts to propagate bilaterally for about 2.4 sec. Then it only propagates in the forward direction at a speed of about 2.5-3.0 km/s. The peak of amplitude of the second ellipse is reached by the rupture front about 3.3 sec. after the start of the earthquake. After 7.9 sec., the process is terminated.

Summary of the rupture process for the 12 inversions.

Inversion 6 PREFERRED MODEL	Inversion using two disconnected ellipses; No use of *a-priori* conditions; The rise-time and rake were not inverted	Misfit for the digital stations: 0.26; Misfit for the analog stations: 0.56; Moment: 1.21×10^{18} N.m; For this inversion, the rupture is only propagating in the forward direction. It takes 3.2 sec. for the first ellipse to be break at a slow rupture speed of 2.2 km/s. After 3.8 sec. the rupture front reaches the second ellipse. The rupture front slightly accelerates to a speed of 3.1 km/s. After 8.2 sec., the second ellipse is entirely broken. For this inversion, we also calculated the stress drop associated with each ellipse using the method described in Kostrov & Das (1984). The stress drop is about 15 MPa for the hypocentral ellipse, and 17 MPa for the second ellipse.
Inversion 7	Inversion using two connected ellipses; No use of *a-priori* conditions; The rise-time and rake were not inverted	Misfit for the digital stations: 0.30; Misfit for the analog stations: 0.55; Moment: 2.08×10^{18} N.m; A backward propagation of the rupture front is observed at the very beginning (first 1.5 sec.), but mostly propagates in the forward direction. As the first ellipse is almost non-existent in term of amplitude, we can consider that the rupture front only propagates at the speed of the second ellipse (3.4 km/s). The peak of slip amplitude of the second ellipse is reached by the rupture front about about 3.2 sec. after the earthquakes initiated. The process then stops after 9.5 sec.
Inversion 8	Inversion using two disconnected ellipses; use of *a-priori* conditions; The rise-time and rake were inverted	Misfit for the digital stations: 0.26; Misfit for the analog stations: 0.57; Moment: 1.20×10^{18} N.m; In this inversion, the rupture front propagates only the forward direction. It breaks the first asperity at a rupture speed of 2 km/s and takes about 3.2 sec. to get across the ellipse. Then, the second asperity starts rupturing after 3.6 sec. It takes 4.2 sec to finish breaking the second asperity at a speed of 3.6 km/s.
Inversion 9	Inversion using two disconnected ellipses; use of *a-priori* conditions; The rise-time and rake were not inverted; We forced each model to have some slip the the hypocenter	Misfit for the digital stations: 0.28; Misfit for the analog stations: 0.67; Moment: 1.90×10^{18} N.m; In this inversion, the rupture front propagates in the forward direction, breaking the first asperity after 2.3 sec at a speed of 2.00 km/s. Then, the second asperity starts rupturing after 3.4 sec. The rupture front then propagates at higher speed (3.1 km/s) It takes 7 sec to finish breaking the second asperity and terminate the process, when the rupture front reaches the end of the fault plane.
Inversion 10	Inversion using two connected ellipses; use of *a-priori* conditions; The rise-time and rake were not inverted; We constrain the moment to be within $+/-15\%$ of the CMT value	Misfit for the digital stations: 0.29; Misfit for the analog stations: 0.53; Moment: 1.22×10^{18} N.m; We observed only a forward propagating of the rupture front for this inversion. The hypocentral high amplitude slip patch starts to break after 0.9 sec, at a speed of 2.3 km/s. The rupture front gets across it 0.6 sec. later. Then it breaks the second ellipse at a speed of 3.1 km/s,reaching its peak of slip amplitude about 3.5 sec. after the earthquake initiation. 7.8 sec. of rupture, are needed before the process stops.

Inversion 11	Inversion using two connected ellipses; use of *a-priori* conditions; The rise-time and rake were not inverted; The 1D velocity model of the south-western side were used	Misfit for the digital stations: 0.34; Misfit for the analog stations: 0.63; Moment: 1.92 $\times$ 10^{18} N.m; During the first 2.5 sec., the rupture front propagates bilaterally and then propagates only in the forward direction. After 5 sec., the rupture front reaches the high slip amplitude patch and breaks it until it reaches the end of the fault plane after 9.8 sec. of process. The rupture speed is nearly constant in the whole process (3.1-3.3 km/s)
Inversion 12	Inversion using three connected ellipses; use of *a-priori* conditions; The rise-time and rake were not inverted;	Misfit for the digital stations: 0.26; Misfit for the analog stations: 0.60; Moment: 2.71 $\times$ 10^{18} N.m; The rupture front propagates bilaterally in the first ellipse at a speed of 2 km/s. After 2.0 sec., the first ellipse is entirely broken. The rupture front continues to propagate through the second ellipse at a speed of 3.4 km/s. 4 sec. after the earthquake initiation, the rupture front reaches the high slip amplitude patch. It then takes about 5 sec. before the rupture front breaks the high slip patch and reaches the end of the fault plane. The small slip amplitude patch, surrounding the high slip patch breaks at a slightly lower rupture speed (2.8 km/s). The process is finished 11 sec. after the start of the earthquake.

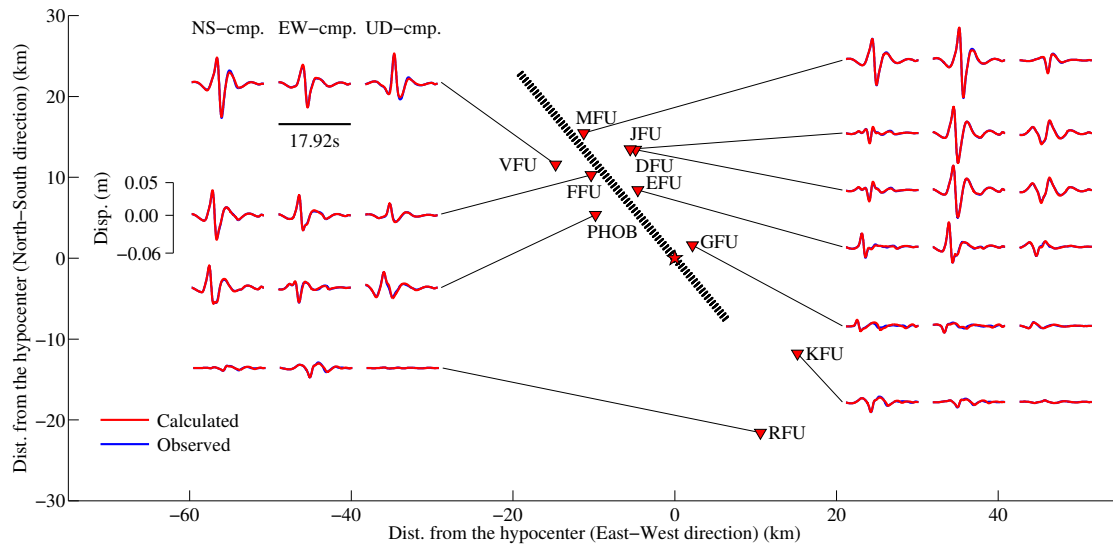# A2   Appendices of Chapter 3

Additional Figures

Figure A2.1: *Test 1*: Comparison between the calculated displacement waveforms obtained by the inversion (ORP1) and the artificial displacement waveforms generated by the Input Rupture Process 1 (IRP1) for the 10 digital stations.
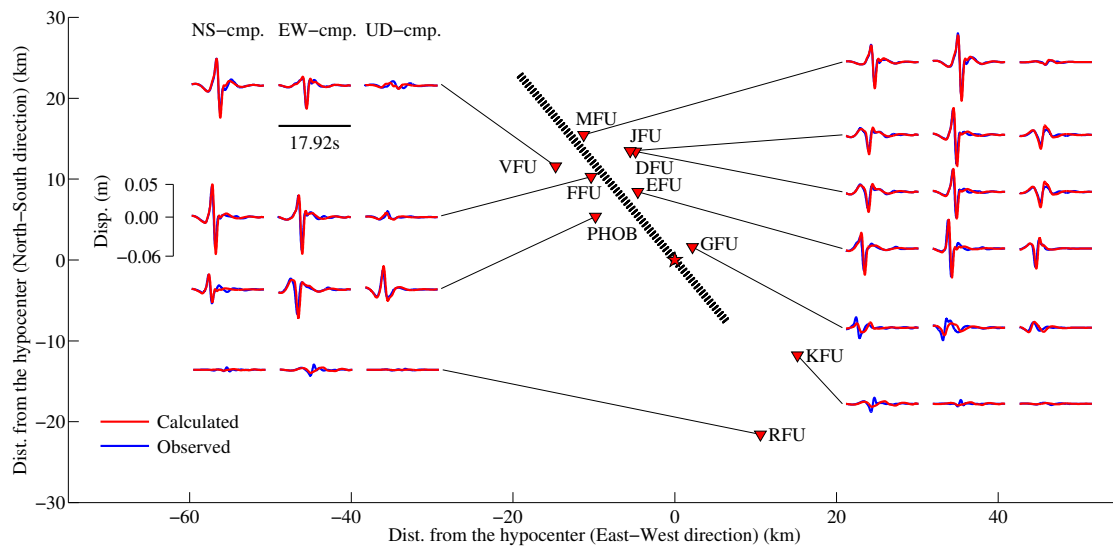

Figure A2.2: *Test 2*: Comparison between the calculated displacement waveforms obtained by the inversion (ORP2) and the artificial displacement waveforms generated by the Input Rupture Process 2 (IRP2) for the 10 digital stations.
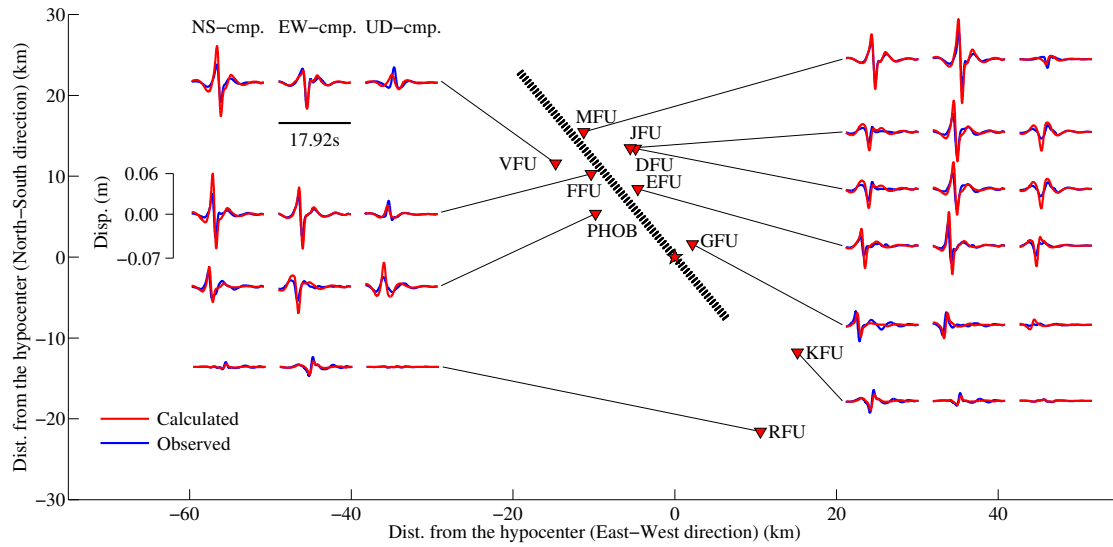
Figure A2.3: *Test 3* - 1 ellipse: Comparison between the calculated displacement waveforms obtained by the inversion using only one ellipse (ORP3a) and the artificial displacement waveforms generated by the Input Rupture Process 2 (IRP3) for the 10 digital stations.
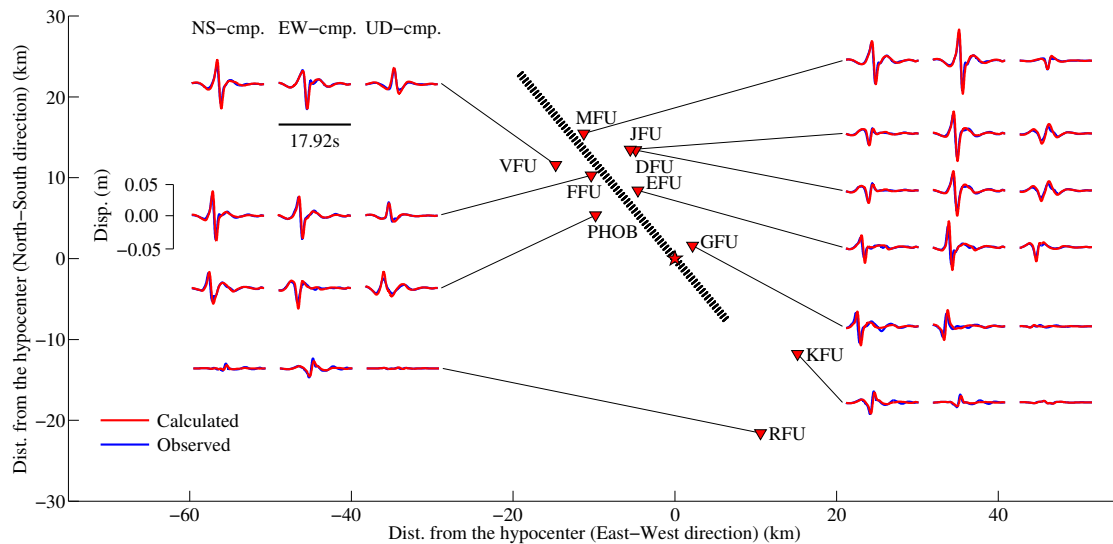

Figure A2.4: *Test 3* - 2 ellipses: Comparison between the calculated displacement waveforms obtained by the inversion using two ellipses (ORP3b) and the artificial displacement waveforms generated by the Input Rupture Process 2 (IRP3) for the 10 digital stations.
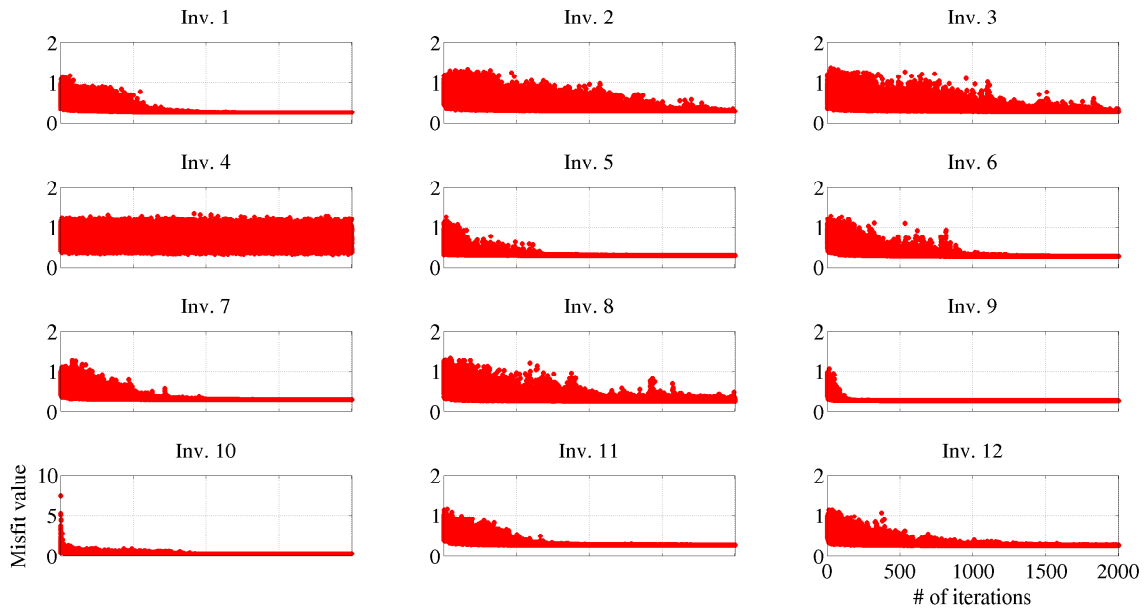
Figure A2.5: Convergence curve for each inversion carried out in Twardzik et al. (2012).
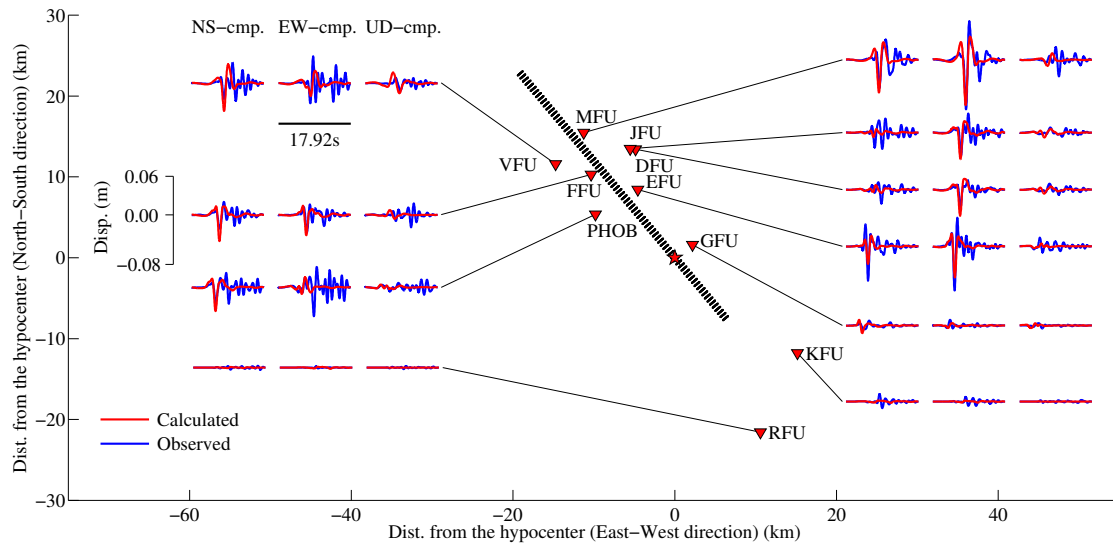

Figure A2.6: Comparison between the calculated velocity waveforms (red line) and the observed velocity waveforms (blue line) at the 10 digital stations, from the slip history obtained by Inversion 8 in Twardzik et al. (2012).
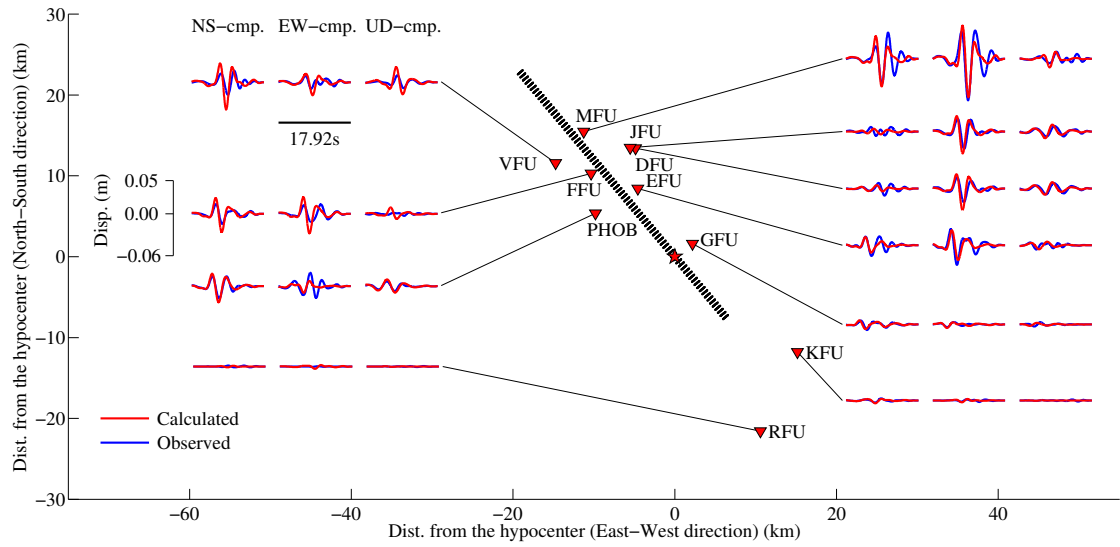
Figure A2.7: Comparison for the inversion at low-frequency (0.16-0.50 Hz) between the calculated waveforms (red line) and the observed waveforms (blue line) at the 10 digital stations.
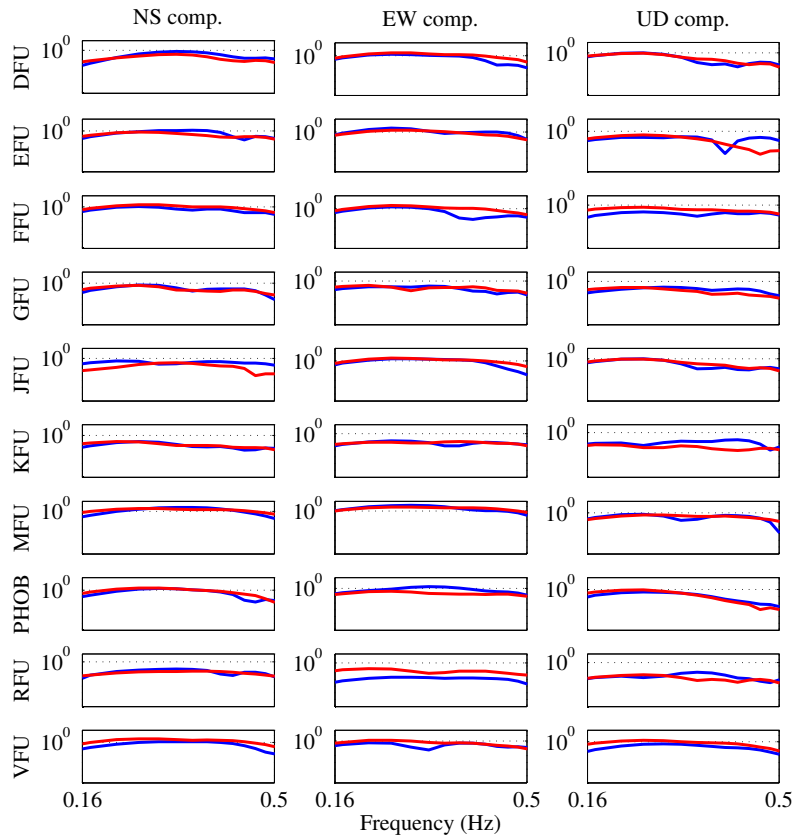

Figure A2.8: Comparison between the spectral amplitude of the calculated waveforms (red line) and of the observed waveforms (blue line) for the 10 digital stations in the frequency range (0.16-0.50 Hz)

A3   Appendices of Chapter 4

Synthetic Tests

To test the performance of our inversion scheme, we carry out two synthetic tests in which we attempt to invert the rupture history from two artificially created "noise-free" dataset. Each one is generated from a different dynamic rupture process and the artificial data are processed the same way as the real dataset that we will use to infer the rupture process of the 2004 Parkfield earthquake.

Test 1:

In the first test (T1), the input rupture process (IM1) ruptures essentially one patch, propagates at about 3 km/s on average and reaches a final seismic moment of 1.38 $\times$ 10^{18} Nm (Figure A3.1). The inversion is carried out using two ellipses in order to investigate how the algorithm behaves when only one ellipse is necessary to describe IM1. We use a common value of T_u for the two ellipses to create the input rupture model as well as during the inversion.

The lowest misfit model from the inversion shows that the two ellipses have merged so that the geometry of its rupture area is very similar to IM1 (Figure A3.1). The final seismic moment for the model obtained by inversion is 25% higher than IM1 (1.72 $\times$ 10^{18} Nm). This is caused by the fact that the rupture area is more spread than in the other rupture model. Also, the use of two ellipses introduces an additional region of moment release compared to IM1. However, it does not significantly affect the fact that the main features of IM1 are retrieved by the inversion. We also observe that the average rupture speed is slower in the rupture model of the inversion (2.8 km/s instead of 3.0 km/s).

The marginal probability density functions (M-PDF) for the 5 dynamic parameters (see Figure A3.2) show that the algorithm has converged towards different values than the one we used to create IM1. This clearly demonstrates the non-uniqueness

Input rupture process (IM1):
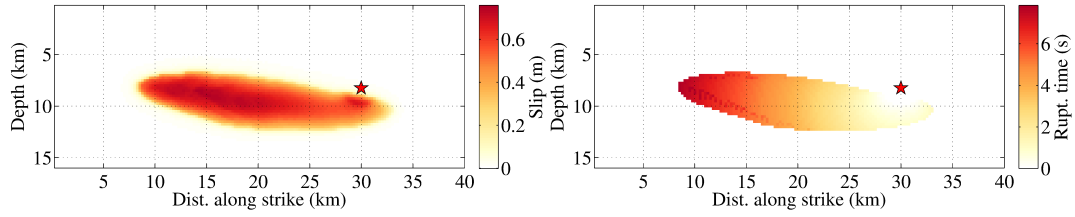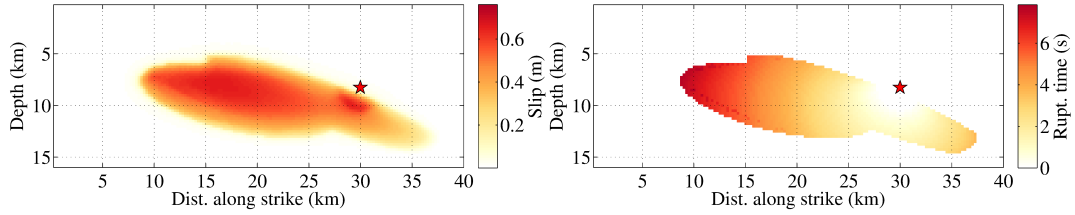

Rupture process obtained from inversion:

Figure A3.1: (top-left): Slip distribution of the input rupture model (IM1) that is used to generate the synthetic dataset. (top-right): Distribution of the rupture isochrones (time of rupture of a point on the fault) for IM1. (bottom-left): Final slip distribution of the rupture model obtained from the inversion. (bottom-right): Distribution of the rupture isochrones for rupture model obtained by inversion. In all sub-figures, the red star shows the location of the hypocenter.

inherent to inverse problems. However, it is interesting to note that despite this non-uniqueness, we are still able to retrieve the main features of the rupture process of IM1.
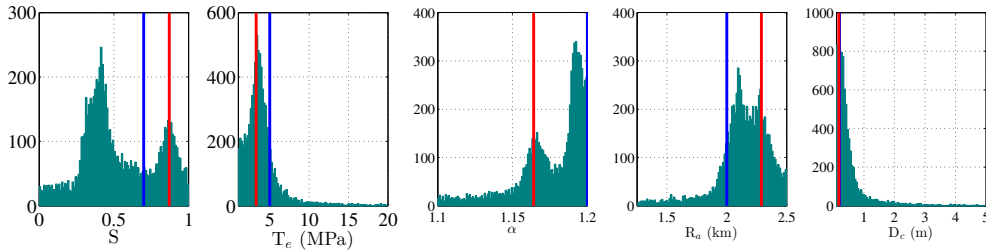

Figure A3.2: Marginal probability density functions (M-PDF) represented for the 5 dynamic parameters from the inversion. The red line shows the value that is used to create IM1 and the blue line shows the value towards which the NA-algorithm converged.

The inversion reaches a very low value of misfit ($\varepsilon = 0.03$) and there are almost no visible differences between the calculated waveforms and the artificial waveforms, except for displacement records with low amplitude (Figure A3.3). This means that different source models produce the same or very similar seismograms.
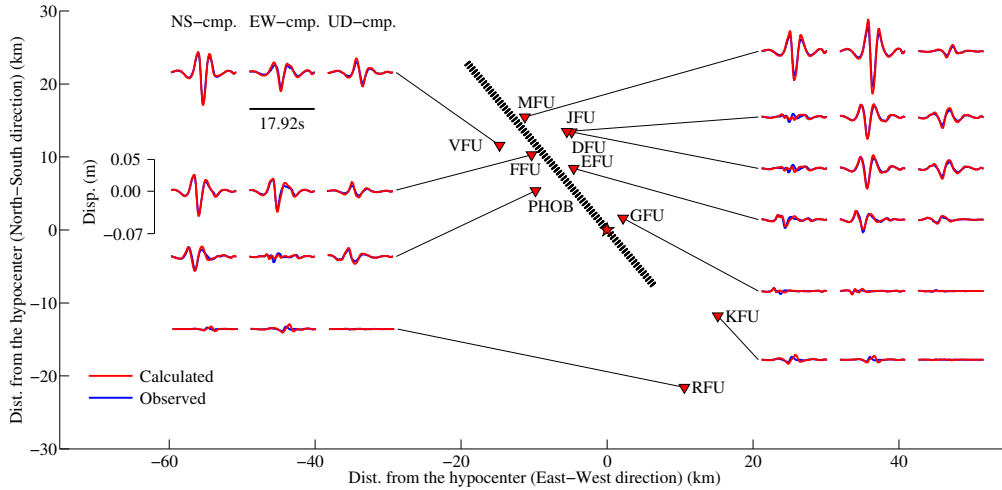
Figure A3.3: Comparison between the artificially waveforms generated by IM1 (blue traces) and the waveforms calculated for the inverted model (red traces).

Test 2:

In our second test (T2), we use a more complicated rupture process to generate the artificial data (Figure A3.4). It induces a jump of the rupture between the first ellipse located at the hypocenter and a second ellipse located about 15 km away from it. The rupture process is also faster compared to the rupture model we created for T1. It has an average rupture speed above the shear wave speed of the medium (4 km/s on average for T2 instead of 3 km/s for T1). Again, we use a common value of T_u for the two ellipses in order to create the input rupture process (IM2) as well as during the inversion.

In this case the geometry of the rupture area is less well retrieved than in the previous case (Figure A3.4). However, the regions of large moment release are still located in the same area as those for IM2. The final seismic moment of the rupture model obtained by inversion is almost identical to IM2, however its rupture occurs at a much faster speed than for IM2 (5.2 km/s instead of 4.0 km/s, i.e. +30%).

In T2, the comparison between the value of the dynamic parameters used to create IM2 and the value retrieved by inversion, shows that they are relatively close to each other (see Figure A3.5). We think that this is because only a limited set of

Input rupture process (IM2):
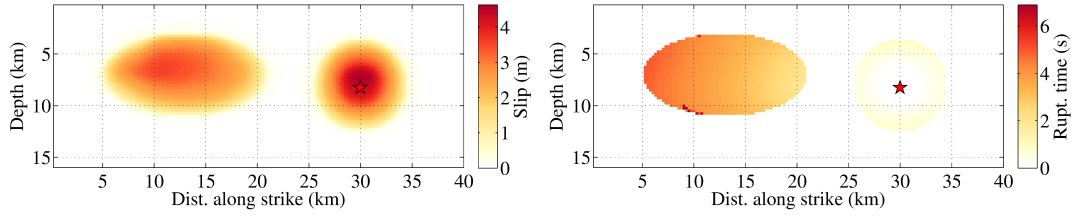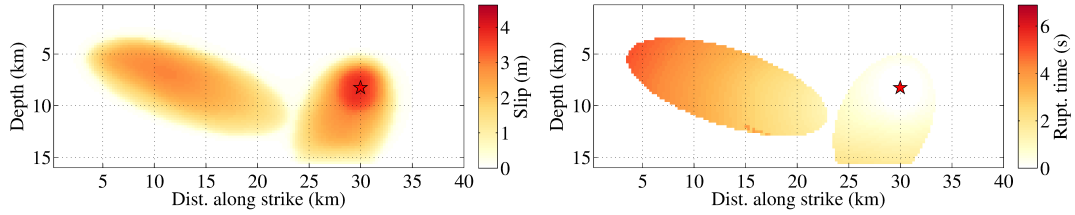

Rupture process obtained from inversion:

Figure A3.4: (left): Slip distribution of the second synthetic model (IM2) that is used to generate the artificial dataset. (right): Distribution of the rupture isochrones of IM2. (bottom-left): Final slip distribution of the rupture model obtained from the inversion. (bottom-right): Distribution of the rupture isochrones for the model obtained by inversion. In all sub-figures, the red star shows the location of the hypocenter.

dynamic parameters can create a rupture process that jumps from one asperity to another. As a consequence the jump reduces the non-uniqueness associated to the dynamic inversion. It is however interesting to note that despite the fact that the dynamic parameters obtained by inversion fall in the vicinity of the ones used to create IM2, we have two rupture models with noticeable differences on the rupture speed.
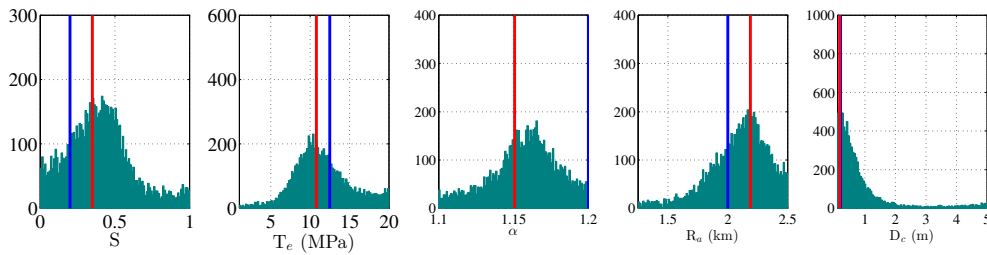

Figure A3.5: Marginal probability density functions (M-PDF) of the 5 dynamic parameters used during the inversion. The red line shows the value that was used to create IM2 and the blue line shows the value towards which the NA-algorithm converged.

Despite the discrepancy between the rupture speed between IM2 and the rupture

speed of the lowest misfit model obtained by inversion, the inversion reaches again a very low misfit ($\varepsilon = 0.08$), showing an excellent agreement between the waveforms calculated from IM2 and the calculated waveforms from the lowest misfit model (see Figure A3.6).
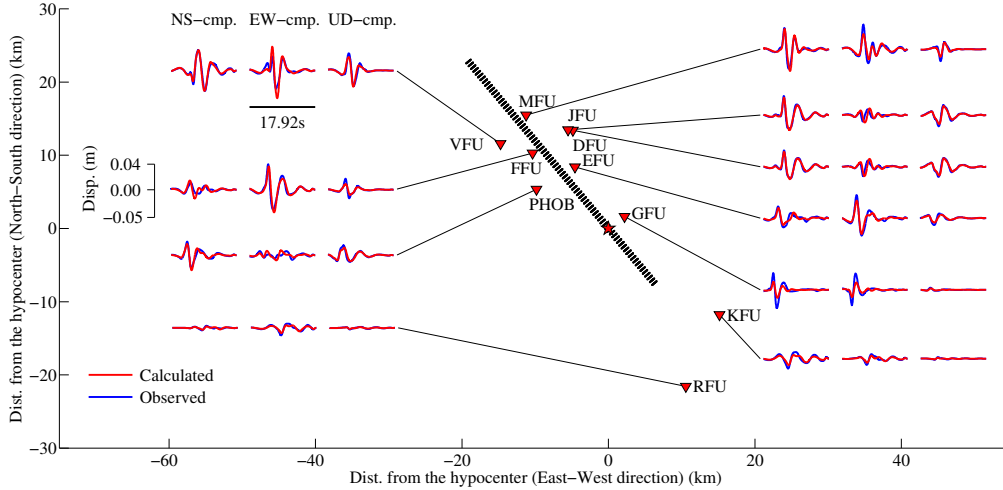

Figure A3.6: Comparison between the artificial waveforms generated by IM2 (blue traces) and the waveforms calculated from the inversion of Test 2 (red traces).

Those two synthetic tests, although they are "noise-free" and assume a perfect knowledge of the velocity structure and geometry of the fault plane, show that it is possible to retrieve the rupture process from seismic records. However, the values of the dynamic parameters obtained by the inversion are less reliable. It shows therefore the non-uniqueness associated with dynamic inversion. It is non-unique at first order because an earthquake can be equally explained by an asperity or a barrier model. But, it is also non-unique at the second order because a significant variation of the dynamic parameters can produce two similar rupture processes, which is caused by the trade-off between the parameters of the friction law. This suggests that detailed investigation of the parameter space is necessary to assess the uncertainty associated with it. Because the results indicate that solutions are non-unique, it will motivate later in the study our use of a Monte-Carlo exploration (Metropolis & Ulam 1949) of the parameter space. However, the two tests show that we can perform a full dynamic inversion to obtain a reliable rupture process

for the 2004 Parkfield earthquake.

Additional Figures
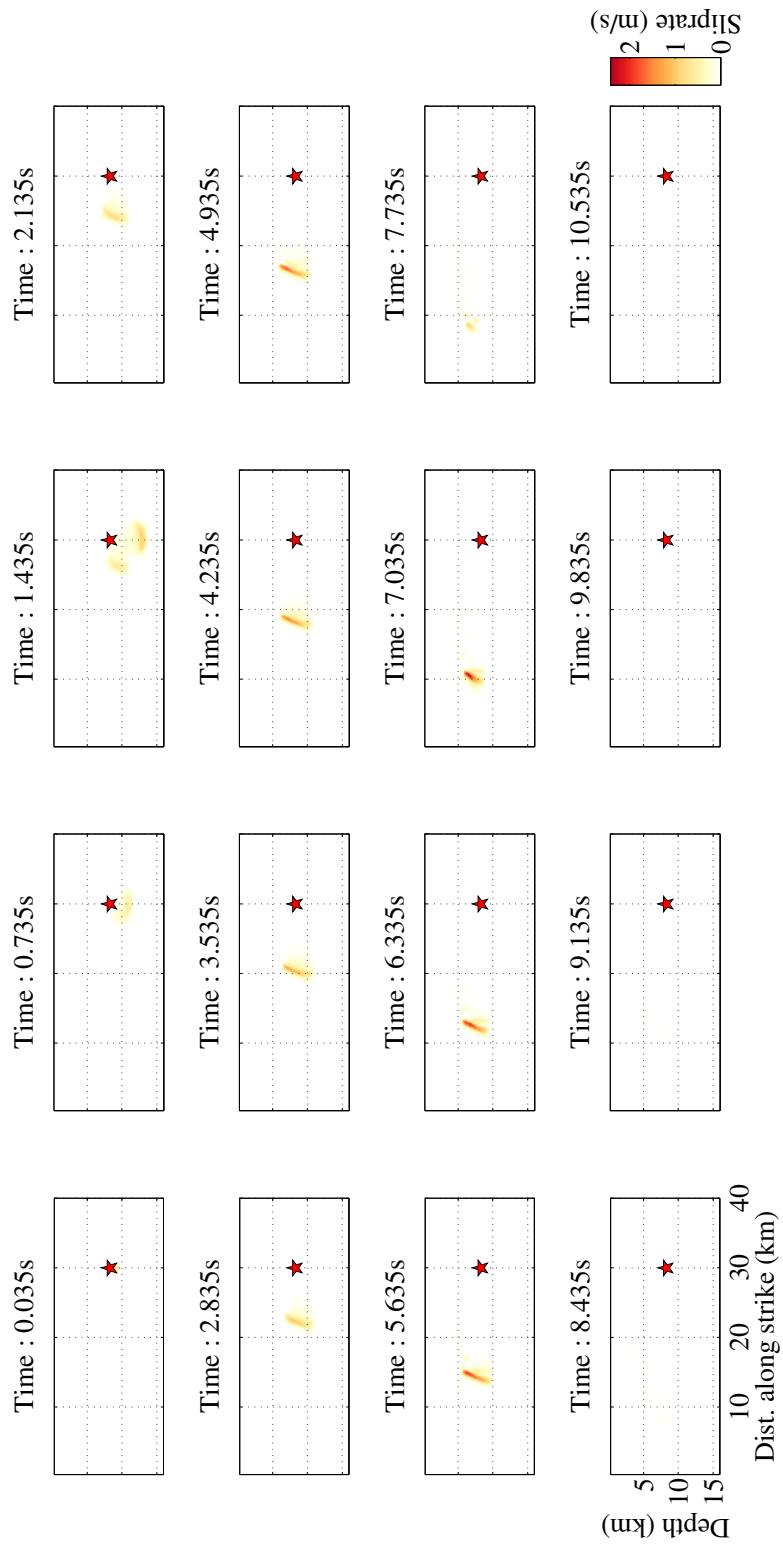
Figure A3.7: Snapshots of the slip-rate of the lowest misfit rupture model obtained by the dynamic inversion. The time-step between each frame is 0.7 s. The red star shows the location of the hypocenter.
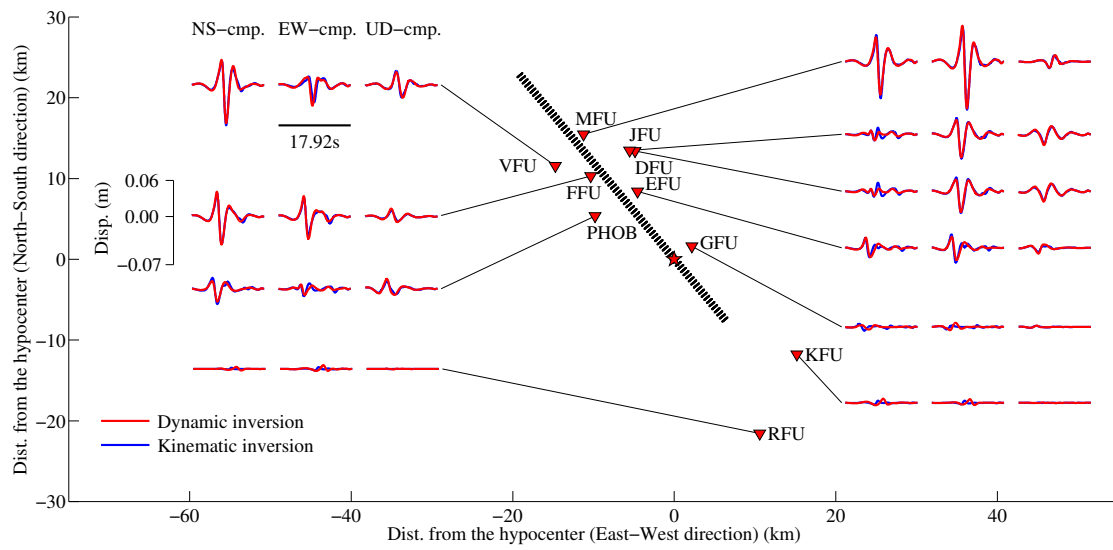
Figure A3.8: Comparison between the calculated displacements from Kinematic Inversion 1 of Twardzik et al. (2012) (blue traces) and the calculated displacements from the Dynamic Inversion of this study (red traces).
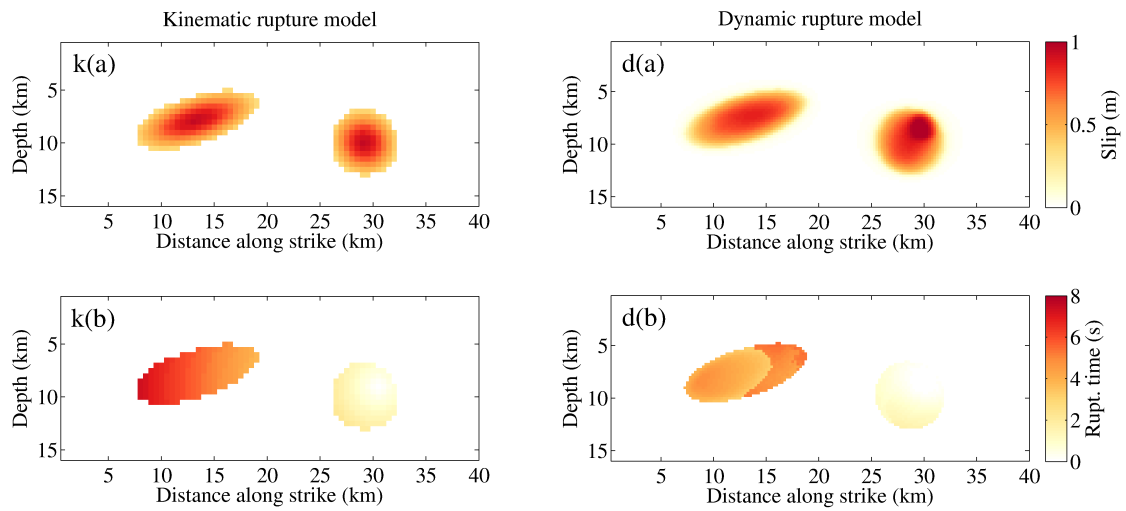
Figure A3.9: Comparison between the kinematic rupture model from Inversion 6 in Twardzik et al. (2012) (k(a) and k(b)) and the best dynamic rupture model found the Monte-Carlo exploration (d(a) and d(b))
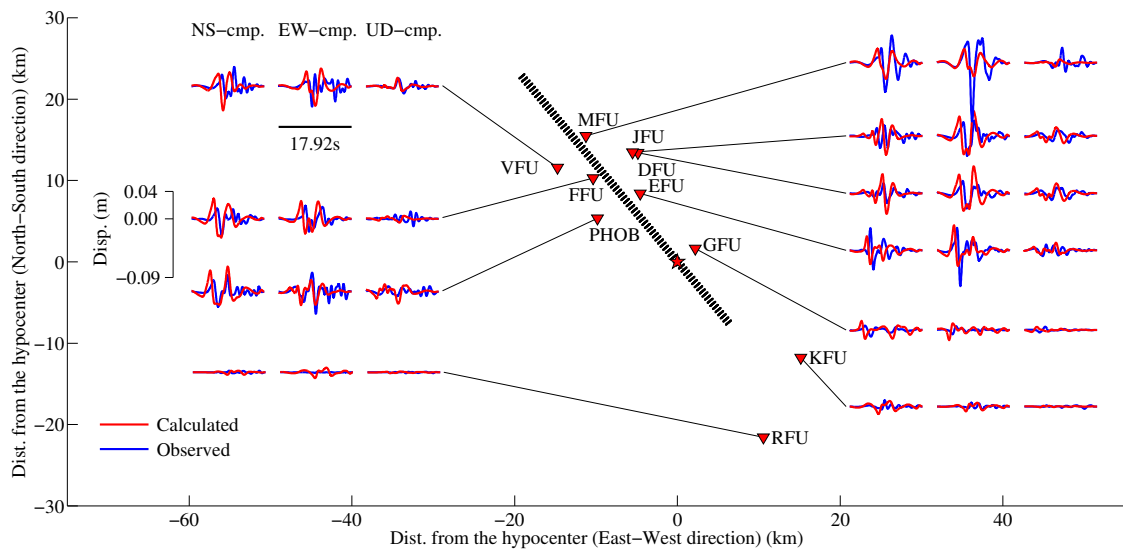
Figure A3.10: Comparison between the observed displacements (blue traces) and the calculated displacements obtained for the best model identified by the Monte-Carlo exploration (red traces). In this case, the geometry of the rupture area is taken from the kinematic Inversion 6 of Twardzik et al. (2012).

A4 Appendices of Chapter 5

Additional Figures and Table
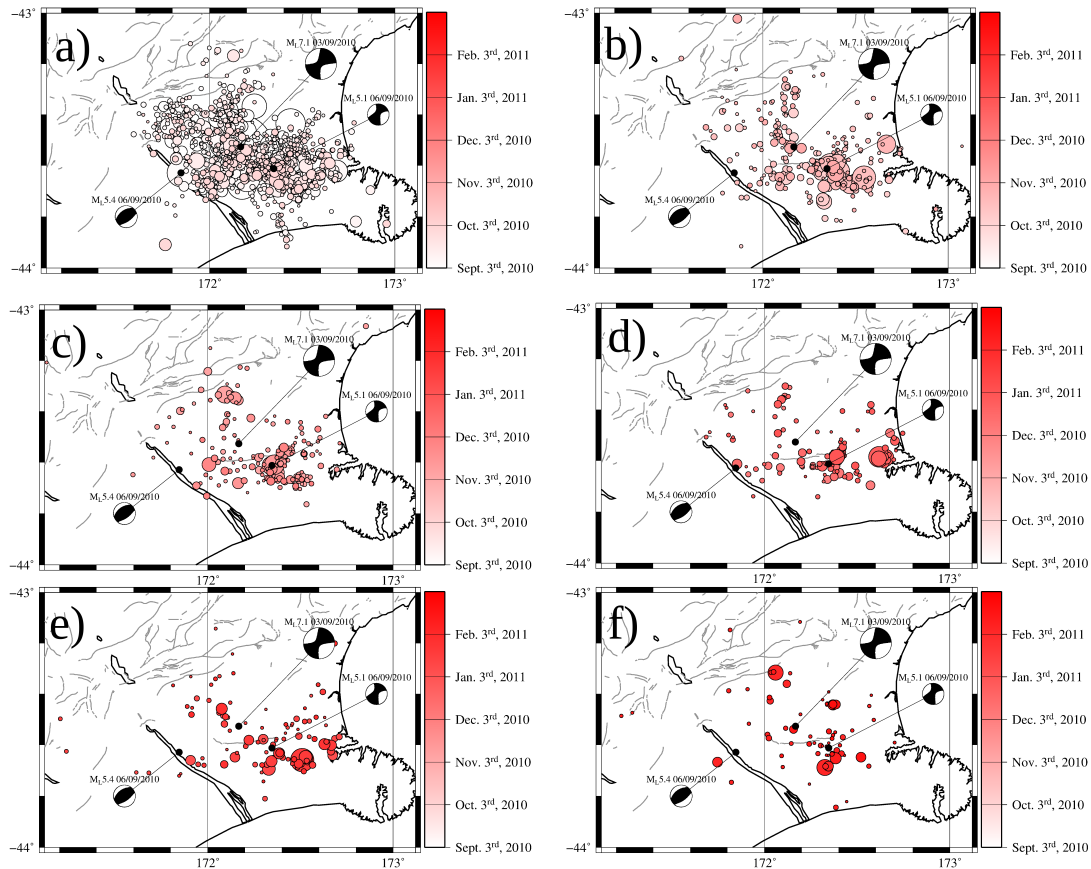
Figure A4.1: Reliably relocated earthquakes from September 3rd, 2010 (day of the Darfield earthquake) to February 21st (day before the Christchurch earthquake). The CMT mechanisms of earthquakes (only 3) in this period are shown. (a): from September 3rd, 2010 to October 2nd, 2010. (b): from October 3rd, 2010 to November 2nd, 2010. (c): from November 3rd, 2010 to December 2nd, 2010. (d): from December 3rd, 2010 to January 2nd, 2011. (e): from January 3rd, 2011 to February 2nd, 2011. (f): from February 3rd, 2011 to February 20th, 2011.
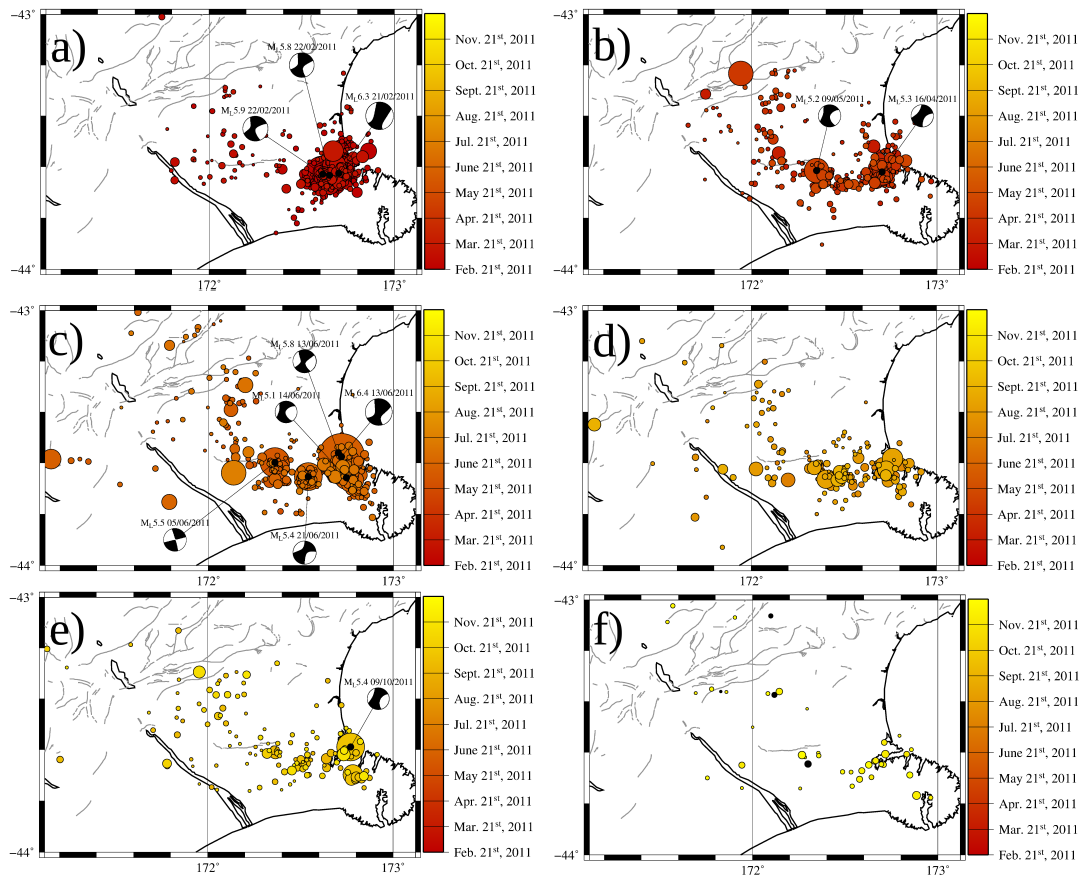
Figure A4.2: Reliably relocated earthquakes from February 21st, 2011 (day of the Christchurch earthquake) to December 22nd (day before the off-shore Christchurch earthquake swarm). The CMT mechanisms of earthquakes in this period are shown. (a): from February 21st, 2011 to March 20th, 2011. (b): from March 21st, 2011 to May 20th, 2011. (c): from May 21st, 2011 to July 20th, 2011. (d): from July 21st, 2011 to September 20th, 2011. (e): from September 21st, 2011 to November 20th, 2011. (f): from November 21st, 2011 to December 22nd, 2011.

Figure A4.3: Static stress changes caused by the M_L6.3, February 21st, 2011 Christchurch earthquake. Blue dots show the seismic activity from December 23rd, 2011 (day of the beginning of the December, 2011 earthquake swarm) till the end of our catalogue. (September 2013). In both figures, the yellow line is the zero contour of the static stress changes field.

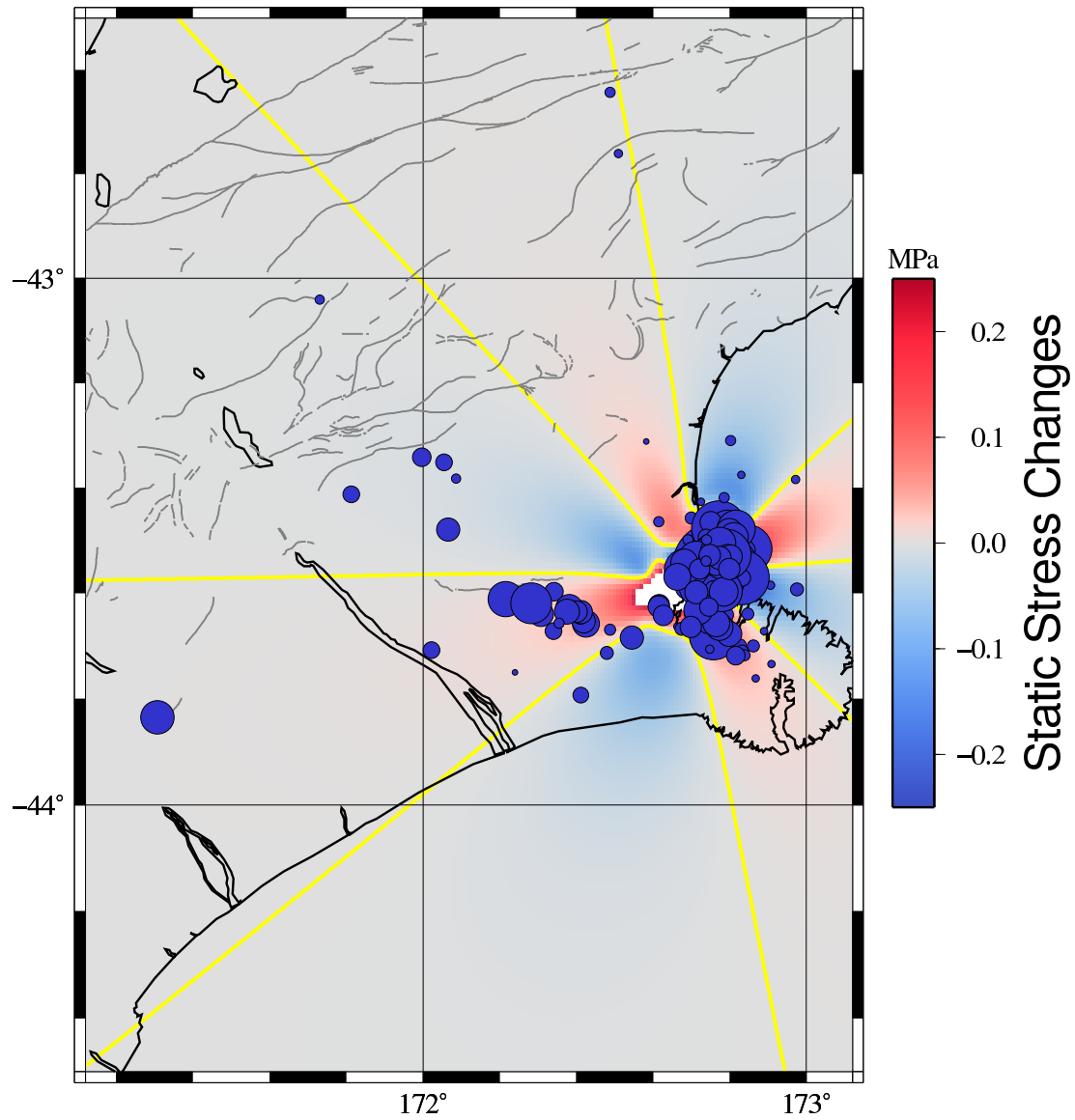| Date	M_L	(Lon,Lat)	P-axis azimuth (∘)	T-axis azimuth (∘)
11/05/1977	5.3	(171.748,-43.309)	311	72
30/03/1992	5.8	(171.250,-43.121)	306	97
18/06/1994	6.7	(171.482,-43.092)	300	31
19/06/1994	6.1	(171.527,-43.150)	128	35
21/06/1994	5.7	(171.490,-43.127)	124	19
29/05/1995	5.9	(171.579,-43.052)	277	11
24/11/1995	6.3	(171.710,-43.029)	121	24
03/09/2010	7.1	(171.168,-43.527)	134	43
06/09/2010	5.1	(171.347,-43.612)	119	210
06/09/2010	5.4	(171.846,-43.629)	145	332
21/02/2011	6.3	(171.700,-43.625)	293	25
22/02/2011	5.8	(171.650,-43.633)	115	24
22/02/2011	5.9	(171.614,-43.629)	112	21
16/04/2011	5.3	(171.703,-43.620)	127	218
09/05/2011	5.2	(171.350,-43.615)	103	194
05/06/2011	5.5	(171.360,-43.598)	300	210
13/06/2011	5.8	(171.702,-43.560)	104	12
13/06/2011	6.4	(171.719,-43.575)	293	24
14/06/2011	5.1	(171.746,-43.658)	101	191
21/06/2011	5.4	(171.540,-43.653)	133	224
09/10/2011	5.4	(171.771,-43.589)	114	205
23/12/2011	5.8	(171.772,-43.525)	122	26
23/12/2011	5.5	(171.762,-43.520)	124	8
23/12/2011	6.1	(171.760,-43.545)	301	39
23/12/2011	5.1	(171.758,-43.681)	122	218
01/01/2012	5.3	(171.772,-43.477)	126	7
06/01/2012	5.3	(171.221,-43.746)	141	3
25/05/2012	5.2	(171.789,-43.527)	135	240

Table A4.1: Details of the P- and T-axis azimuths taken from the 28 earthquakes reported in the CMT catalogue between January 1976 and September 2013. The magnitude (M_L) is the one reported by the GeoNet catalogue.

Bibliography

Adams, J., 1980. Paleoseismicity of the Alpine fault seismic gap, New Zealand, *Geology*, **8**(2), 72–76.

Aki, K., 1968. Seismic displacements near a fault, *J. Geophys. Res.*, **73**(16), 5359–5376.

Aki, K., 1972. *The Upper Mantle*, Chap.: Earthquake mechanism, pp. 423–446, Tectonophysics 13(1-4), Elsevier Publishing Company, Amsterdam.

Alciatore, D. G. & Miranda, R., 1995. A winding number and point-in-polygon algorithm, Glaxo virtual anatomy project research report, Colorado State University.

Allmann, B. P. & Shearer, P. M., 2007. A High-Frequency secondary event during the 2004 Parkfield earthquake, *Science*, **318**(5854), 1279–1283.

Andrews, D. J., 1976. Rupture velocity of plane strain shear cracks, *J. Geophys. Res.*, **81**(32), 5679–5687.

Aochi, H. & Fukuyama, E., 2002. Three-dimensional nonplanar simulation of the 1992 Landers earthquake, *J. Geophys. Res.*, **107**(B2), ESE 4–1–ESE 4–12.

Archuleta, R. J., 1984. A faulting model for the 1979 Imperial Valley earthquake, *J. Geophys. Res.*, **89**(B6), 4559–4585.

Bakun, W. H. & Lindh, A. G., 1985. The Parkfield, California, earthquake prediction experiment, *Science*, **229**(4714), 619–624.

Bakun, W. H. & McEvilly, T. V., 1979. Earthquakes near Parkfield, California: Comparing the 1934 and 1966 sequences, *Science*, **205**(4413), 1375–1377.

Beavan, J. & Haines, J., 2001. Contemporary horizontal velocity and strain rate fields of the pacific-australian plate boundary zone through new zealand, *J. Geophys. Res.*, **106**(B1), 741–770.

Beavan, J., Samsonov, S., Motagh, M., Wallace, L., Ellis, S., & Palmer, N., 2010. The Darfield (Canterbury) earthquake: Geodetic observations and preliminary source model, *Bulletin of the New Zealand Society for Earthquake Engineering*, **43**(4), 228–235.

Beavan, J., Fielding, E., Motagh, M., Samsonov, S., & Donnelly, N., 2011. Fault location and slip distribution of the 22 February 2011 $M_w 6.2$ Christchurch, New-Zealand, earthquake from geodetic data, *Seismol. Res. Lett.*, **82**(6), 789–799.

Ben-Menahem, A., 1961. Radiation of seismic surface waves from finite moving sources, *Bull. Seism. Soc. Am.*, **51**(3), 401–435.

Ben-Menahem, A., 1962. Radiation of seismic body waves from finite moving source in the Earth, *J. Geophys. Res.*, **67**(1), 345–350.

Ben-Zion, Y., 1998. Properties of seismic fault zone waves and their utility for imaging low-velocity structures, *J. Geophys. Res.*, **103**(B3), 12567–12585.

Ben-Zion, Y. & Rice, J. R., 1993. Earthquake failure sequences along a cellular fault zone in a three-dimensional elastic solid containing asperity and nonasperity regions, *J. Geophys. Res.*, **98**(B8), 14109–14131.

Benioff, H., 1955. *Earthquake in Kern County California during 1952*, Chap.: 10. Mechanism and strain characteristics of the White Wolf Fault as indicated by the aftershock sequence, pp. 199–202, Bulletin 171, Division of Mines and Geology, California.

Beroza, G. C. & Spudich, P., 1988. Linearized inversion for fault rupture behaviour: Application to the 1984 Morgan Hill, California, earthquake, *J. Geophys. Res.*, **93**(B6), 6275–6296.

Bizarri, A. & Das, S., 2012. Mechanics of 3-D shear cracks between Rayleigh and shear wave rupture speeds, *Earth Planet. Sci. Lett.*, **357-358**, 397–404.

Borcherdt, R. D., Fletcher, J. B., Jensen, E. G., Maxwell, G. L., VanSchaak, J. R., Warrick, R. E., Cranswick, E., Johnston, M. J. S., & McClearn, R., 1985. A general earthquake observation system (GEOS), *Bull. Seism. Soc. Am.*, **75**(6), 1783–1825.

Borcherdt, R. D., Johnston, M. J. S., Glassmoyer, G., & Dietel, C., 2006. Recordings of the 2004 Parkfield earthquake on the General Earthquake Observation System Array: Implications for earthquake precursors, fault rupture, and coseismic strain change, *Bull. Seism. Soc. Am.*, **96**, 73–89.

Bouchon, M., 1981. A simple method to calculate Green's functions for elastic layered media, *Bull. Seism. Soc. Am.*, **71**(4), 959–971.

Bouchon, M., Durand, V., Marsan, D., Karabulut, H., & Schmittbuhl, J., 2013. The long precursory phase of most large interplate earthquakes, *Nat. Geosci.*, **6**, 299–302.

Bruhat, L., Barbot, S., & Avouac, J., 2011. Evidence for postseismic deformation of the lower crust following the 2004 mw6.0 parkfield earthquake, *J. Geophys. Res.*, **116**, B08401.

Burridge, R. & Knopoff, L., 1964. Body force equivalent for seismic dislocations, *Bull. Seism. Soc. Am.*, **54**(6A), 1875–1888.

Calais, E. & Stein, S., 2009. Time-variable deformation in the New Madrid zone, *Science*, **323**(5920), 1442.

Clayton, R. & Engquist, B., 1977. Absorbing boundary conditions for acoustic and elastic wave equations, *Bull. Seism. Soc. Am.*, **67**(6), 1529–1540.

Cotton, F. & Coutant, O., 1997. Dynamic stress variations due to shear faults in a plane-layered medium, *Geophys. J. Int.*, **128**(3), 676–688.

Custodio, S. & Archuleta, R. J., 2007. Parkfield earthquakes: Characteristic or complementary?, *J. Geophys. Res.*, **112**(B5), B05310.

Custodio, S., Page, M. T., & Archuleta, R. J., 2009. Constraining earthquake source inversion with GPS data: 2. A two-step approach to combine seismic and geodetic data sets, *J. Geophys. Res.*, **114**(B1), B01315.

Das, S. & Aki, K., 1977a. A numerical study of two-dimensional spontaneous rupture propagation, *Geophys. J. R. astr. Soc.*, **50**(3), 643–668.

Das, S. & Aki, K., 1977b. Fault plane with barrier: A versatile earthquake model, *J. Geophys. Res.*, **82**(36), 5658–5670.

Das, S. & Henry, C., 2003. Spatial relation between main earthquake slip and its aftershock distribution, *Rev. Geophys.*, **41**(3), 1013.

Das, S. & Kostrov, B. V., 1983. Breaking of a single asperity: Rupture process and seismic radiation, *J. Geophys. Res.*, **88**(B5), 4277–4288.

Das, S. & Kostrov, B. V., 1990. Inversion for seismic slip rate and distribution with stabilizing constraints: Application to the 1986 Andreanof Islands earthquake, *J. Geophys. Res.*, **95**(B5), 6899–6913.

Das, S. & Kostrov, B. V., 1994. Diversity of solutions of the problem of earthquake faulting inversions; application to SH waves for the great 1989 Macquarie Ridge earthquake, *Phys. Earth planet. Int.*, **85**(3-4), 293–318.

Das, S. & Scholz, C. H., 1981. Off-fault aftershock clusters caused by shear stress increase, *Bull. Seism. Soc. Am.*, **71**(5), 1669–1675.

Das, S. & Suhadolc, P., 1996. On the inverse problem for earthquake rupture: The Haskell-type source model, *J. Geophys. Res.*, **101**(B3), 5725–5738.

Day, S., 1982. Three-dimensional simulation of spontaneous rupture: The effect of nonuniform prestress, *Bull. Seism. Soc. Am.*, **72**(6A), 1881–1902.

Delescluse, M., Chamot-Rooke, N., Cattin, R., Fleitout, L., Trubienko, O., & Vigny, C., 2012. April 2012 intra-oceanic seismicity off Sumatra boosted by the Banda-Aceh megathrust, *Nature*, **490**, 240–244.

DeMets, C., Gordon, R. G., & Argus, D. F., 2010. Geologically current plate motions, *Geophys. J. Int.*, **181**(1), 1–80.

Dewey, J. W., 1971. *Seismicity Studies with the Method of Joint Hypocenter Determination*, Ph.D. Thesis, University of California, Berkeley.

Di Carli, S., Francois-Holden, C., Peyrat, S., & Madariaga, R., 2010. Dynamic inversion of the 2000 Tottori earthquake based on elliptical subfault approximations, *J. Geophys. Res.*, **115**(B12), B12238.

Dietriech, J. H., 1978. Time-dependent friction and mechanics of stick-slip, *Pageoph.*, **116**(4-5), 790–806.

Douglas, G., 1967. Joint epicentre determination, *Nature*, **215**, 47–48.

Elliott, J. R., Nissen, E. K., England, P. C., Jackson, J. A., Lamb, S., Li, Z., Oehlers, M., & Parsons, B., 2012. Slip in the 2010-2011 Canterbury earthquakes, New Zealand, *J. Geophys. Res.*, **117**(B3), B03401.

England, P. & Jackson, J., 2011. Uncharted seismic risk, *Nat. Geosci.*, **4**, 348–349.

Fedotov, S. A., 1965. Regularities of the distribution of strong earthquakes in Kamchatka, the Kuril Islands, and northeastern Japan, *Akad. Nauk SSSR Inst. Fisiki Zemli*, **36**(203), 66–93.

Fletcher, J. B., Spudich, P., & Baker, L. M., 2006. Rupture propagation of the 2004 Parkfield, California, earthquake from observation at the UPSAR, *Bull. Seism. Soc. Am.*, **96**(4B), 129–142.

Fukushima, K., Kanaori, Y., & Miura, F., 2010. Influence of fault process zone on ground shaking of inland earthquakes: Verification of M_j=7.3 Western Tottori Prefecture and M_j=7.0 West Off Fukuoka Prefecture earthquakes, southwest Japan, *Eng. Geo.*, **116**(1-2), 157–165.

Fukuyama, E. & Irikura, K., 1986. Rupture process of the 1983 Japan Sea (Akita-Oki) earthquake using a waveform inversion method, *Bull. Seism. Soc. Am.*, **76**(6), 1623–1640.

Fukuyama, E. & Mikumo, T., 1993. Dynamic rupture analysis: Inversion for the source process of the 1990 Izu-Oshima, Japan, earthquake (M=6.5), *J. Geophys. Res.*, **98**(B4), 6529–6542.

Gledhill, K., Ristau, J., Reyners, M., Fry, B., & Holden, C., 2011. The Darfield (Canterbury, New-Zealand) M_w7.1 earthquake of September 2010: preliminary seismological report, *Seismol. Res. Lett.*, **82**(3), 378–386.

Graves, R. W. & Wald, D. J., 2001. Resolution analysis of finite fault source inversion using one- and three-dimensional Green's functions 1. Strong motions, *J. Geophys. Res.*, **106**(B5), 8745–8766.

Griffith, A. A., 1921. The phenomena of rupture and flow in solids, *Phil. Trans. R. Soc. Lond. A*, **221**(582-593), 163–198.

Harris, R. A., 1998. Introduction to special section: Stress triggers, stress shadows and implications for seismic hazard, *J. Geophys. Res.*, **103**(B10), 24347–24358.

Harris, R. A. & Segall, P., 1987. Detection of a locked zone at depth on the Parkfield, California, segment of the San Andreas Fault, *J. Geophys. Res.*, **92**(B8), 7945–7962.

Hartzell, S., 1989. Comparison of seismic waveform inversion results for the rupture history of a finite fault: Application to the 1986 North Palm Springs, California, earthquake, *J. Geophys. Res.*, **95**(B6), 7515–7534.

Hartzell, S., Liu, P., Mendoza, C., Ji, C., & Larson, K. M., 2007. Stability and uncertainty of finite-fault slip inversions: Application to the 2004 Parkfield, California, earthquake, *Bull. Seism. Soc. Am.*, **97**(6), 1911–1934.

Hartzell, S. H. & Heaton, T. H., 1983. Inversion of strong ground motion and teleseismic waveform data for the fault rupture history of the 1979 Imperial Valley, California, earthquake, *Bull. Seism. Soc. Am.*, **73**(6), 1553–1583.

Haskell, N. A., 1964. Total energy and energy spectral density of elastic wave radiation for propagating faults, *Bull. Seism. Soc. Am.*, **59**(6A), 1811–1841.

He, J. & Peltzer, G., 2010. Poroelastic triggering in the 9-22 January 2008 Nima-Gaize (Tibet) earthquake sequence, *Geology*, **38**, 907–910.

Henry, C., Das, S., & Woodhouse, J. H., 2000. The great March 25, 1998, Antarctic Plate earthquake: Moment tensor and rupture history, *J. Geophys. Res.*, **105**(B7), 16097–16118.

Houlié, N., Dreger, D., & Kim, A., 2013. Gps source solution of the 2004 Parkfield earthquake, *Sci. Rep.*, **4**, 1–9.

Hsu, V., Helsley, C. E., Berg, E., & Novelo-Casanova, D. A., 1985. Correlation of foreshocks and aftershocks and asperities, *Pure Appl. Geophys.*, **122**(6), 878–893.

Hurukawa, N., Tun, P. P., & Shibazaki, B., 2012. Detailed geometry of the subducting Indian Plate beneath the Burma Plate and subcrustal seismicity in the Burma plate derived from Joint Hypocenter Relocation, *Earth Planets Space*, **64**(4), 333–343.

Ida, Y., 1972. Cohesive force across the tip of a longitudinal-shear crack and Griffith's specific surface energy, *J. Geophys. Res.*, **77**(20), 3796–3805.

Ide, S., 1999. Source process of the 1997 Yamaguchi, Japan, earthquake analyzed in different frequency bands, *Geophys. Res. Lett.*, **36**(13), 1973–1976.

Jackson, D. D. & Matsu'ura, M., 1985. A bayesian approach to nonlinear inversion, *J. Geophys. Res.*, **90**(B1), 581–591.

Johanson, I. A., Fielding, E. J., Rolandone, F., & Bürgmann, R., 2006. Coseismic and postseismic slip of the 2004 Parkfield earthquake from space-geodetic data, *Bull. Seism. Soc. Am.*, **96**(4B), S269–S282.

Johnson, K. M., Bürgmann, R., & Larson, K., 2006. Frictional properties on the San Andreas Fault near Parkfield, California, inferred from models on afterslip following the 2004 earthquake, *Bull. Seism. Soc. Am.*, **96**, S321–S338.

Kanamori, H., 181. *Earthquake Prediction: An International Review*, Chap.: The nature of seismicity patterns before large earthquakes, pp. 1–19, Maurice Ewing Series 4, American Geophysical Union, Washington, D. C.

Kanamori, H. & Stewart, G. S., 1978. Seismological aspects of the Guatemala earthquake of February 4, 1976, *J. Geophys. Res.*, **83**(B7), 3427–3434.

Käufl, P., Valentine, A. P., O'Toole, T. B., & Trampert, J., 2014. A framework for fast probabilistic centroid-moment-tensor determination inversion of regional static displacement measurements, *Geophys. J. Int.*, **196**(3), 1676–1693.

Kennett, B. L. N. & Kerry, N. J., 1979. Seismic waves in a stratified half space, *Geophys. J. R. astr. Soc.*, **57**(3), 557–583.

King, G. C. P., Stein, R. S., & Lin, J., 1994. Static stress changes and the triggering of earthquakes, *Bull. Seism. Soc. Am.*, **84**(3), 935–953.

Konca, A. O., Kaneko, Y., Lapusta, N., & Avouac, J. P., 2013. Kinematic inversion of physically plausible earthquake source models obtained from dynamic rupture simulations, *Bull. Seism. Soc. Am.*, **103**(5), 2621–2644.

Kostrov, B. V., 1964. Selfsimilar problems of propagation of shear cracks, *J. Appl. Math. Mech.-USSR*, **28**(5), 1077–1087.

Kostrov, B. V., 1966. Unsteady propagation of longitudinal shear cracks, *J. Appl. Math. Mech.-USSR*, **30**(6), 1241–1248.

Kostrov, B. V. & Das, S., 1984. Evaluation of stress and displacement fields due to an elliptical plane shear crack, *Geophys. J. R. astr. Soc.*, **78**(1), 19–33.

Li, Y., De Pascale, G. P., Quigley, M. C., & Gravley, D., 2012. Subsurface rock damage structure of the $M_w7.1$ Darfield and $M_w6.3$ Christchurch earthquake sequence viewed with Fault-Zone Trapped Waves (abstract), *AGU Fall Meeting Abstracts*, pp. id. S21B–2446.

Li, Y. G., Leary, P., Aki, K., & Malin, P., 1990. Seismic trapped modes in the Oroville and San Andreas Fault zones, *Science*, **249**(4970), 763–766.

Li, Y. G., Vidale, J. E., & Cochran, E. S., 2004. Low-velocity damaged structure of the San Andreas Fault at Parkfield from fault zone trapped waves, *Geophys. Res. Lett.*, **31**(12), L12S06.

Liu, P., Custodio, S., & Archuleta, R. J., 2006. Kinematic inversion of the 2004 $M_w6.0$ Parkfield earthquake including an approximation to site effects, *Bull. Seism. Soc. Am.*, **96**(4B), 143–158.

Liu, P., Custodio, S., & Archuleta, R. J., 2008. *Erratum to* kinematic inversion of the 2004 M$_w$6.0 Parkfield earthquake including an approximation to site effects, *Bull. Seism. Soc. Am.*, **98**(4), 2101.

Ma, S., Custodio, S., Archuleta, R. J., & Liu, P., 2008. Dynamic modeling of the 2004 M$_w$6.0 Parkfield, California earthquake, *J. Geophys. Res.*, **113**(B2), B02301.

Madariaga, R., 1976. Dynamics of an expanding circular fault, *Bull. Seism. Soc. Am.*, **66**(3), 639–666.

Madariaga, R., 1979. On the relation between seismic moment and stress drop in the presence of stress and strength heterogeneity, *J. Geophys. Res.*, **84**(B5), 2243–2250.

Madariaga, R. & Olsen, K. B., 2000. Criticality of rupture dynamics in 3D, *Pure Appl. Geophys.*, **157**(11-12), 1981–2001.

Madariaga, R., Olsen, K., & Archuleta, R., 1998. Modeling dynamic rupture in a 3D earthquake fault model, *Bull. Seism. Soc. Am.*, **88**(5), 1182–1197.

Malin, P. E., Blakeslee, S. N., Alvarez, M. G., & Martin, A. J., 1989. Microearthquake imaging of the Parkfield asperity, *Science*, **244**(4904), 557–559.

Mallet, R., 1848. On the dynamics of earthquakes; being an attempt to reduce their observed phenomena to the known laws of wave motion in solids and fluids, *The Transactions of the Royal Irish Academy*, **21**, 51–105.

Mallet, R. & Mallet, J. W., 1858. *The Earthquake Catalogue of the British Association with the discussion, curves, and maps etc.*, Taylor and Francis, London.

McCloskey, J., 2011. Focus on known active faults, *Nat. Geosci.*, **4**, 494.

Mendoza, C. & Hartzell, S., 1988. Inversion for slip distribution using teleseismic p waveforms: North palm springs, borah peak, and michoacan earthquakes, *Bull. Seism. Soc. Am.*, **78**(3), 1092–1111.

Menke, W., 1985. Imaging fault slip using teleseismic waveforms: Analysis of a typical incomplete tomography problem, *Geophys. J. R. astr. Soc.*, **81**(1), 197–204.

Metropolis, N. & Ulam, S., 1949. The Monte Carlo method, *J. A. Stat. Assoc.*, **44**(247), 335–341.

Michell, J., 1759. Conjectures concerning the cause, and observations upon the phaenomena of earthquakes; particularly of that great earthquake of the first of November, 1755, which proved so fatal to the city of Lisbon, and whose effects were felt as far as Africa, and more or less throughout almost all Europe, *Phil. Trans.*, **51**, 566–634.

Mogi, K., 1969. 16. some features of recent seismic activity in and near Japan (2) Activity before and after great earthquake, *Bull. Earthq. Res. Inst.*, **47**, 395–417.

Mogi, K., 1990. Seismicity before and after large shallow earthquakes around the Japanase islands, *Tectonophysics*, **175**(1-3), 1–33.

Murray, J. & Langbein, J., 2006. Slip on the San Andreas fault at Parkfield, California, over two earthquake cycles and the implications for seismic hazard, *Bull. Seism. Soc. Am.*, **96**(4B), 283–303.

Nakano, H., 1923. Notes on the nature of the forces which gives rise to the earthquake motions, *Seismol. Bull. Central Meteorol. Obs. Japan*, **1**, 92–120.

Nalbant, S. S., Steacy, S., Sieh, K., Natawidjaja, D., & McCloskey, J., 2005. Seismology: Earthquake risk on the Sunda trench, *Nature*, **435**, 756–757.

Nielsen, S., Spagnuolo, E., Violay, V., Smith, S., Scarlato, P., Romeo, G., Di Felice, F., & Di Toro, G., 2013. Measuring fracture energy under coseismic conditions (abstract), *EGU General Assembly Conference Abstracts*, **15**, id. EGU2013–11045.

Oglesby, D. D., Dreger, D. S., Harris, R. A., Ratchkovski, N., & Hansen, R., 2004. Inverse kinematic and forward dynamic models of the 2002 Denali fault earthquake, Alaska, *Bull. Seism. Soc. Am.*, **94**(6B), 214–232.

Olsen, K. B., Madariaga, R., & Archuleta, R. J., 1997. Three-dimensional dynamic simulation of the 1992 Landers earthquake, *Science*, **278**(5339), 834–838.

Olson, A. H. & Anderson, J. G., 1988. Implications of frequency-domain inversion of earthquake ground motions for resolving the space-time dependence of slip on an extended fault, *Geophys. J. Int.*, **94**(3), 443–455.

Olson, A. H. & Aspel, R. J., 1982. Finite faults and inverse theory with applications to the 1979 Imperial Valley earthquake, *Bull. Seism. Soc. Am.*, **72**(6A), 1969–2001.

Orense, R. P., Kiyota, T., Yamada, S., Cubrinovski, M., Hosono, Y., Okamura, M., & Yasuda, S., 2011. Comparison of liquefaction features observed during the 2010 and 2011 Canterbury earthquakes, *Seismol. Res. Lett.*, **82**(6), 905–918.

Peyrat, S. & Olsen, K. B., 2004. Nonlinear dynamic rupture inversion of the 2000 Western Tottori, Japan, earthquake, *Geophys. Res. Lett.*, **31**(5), L05604.

Peyrat, S., Olsen, K., & Madariaga, R., 2001. Dynamic modeling of the 1992 Landers earthquake, *J. Geophys. Res.*, **106**(B11), 26467–26482.

Peyrat, S., Madariaga, R., Buforn, E., Campos, J., Asch, G., & Vilotte, J. P., 2010. Kinematic rupture process of the 2007 Tocopila earthquake and its main aftershocks from teleseismic and strong-motion data, *Geophys. J. Int.*, **182**(3), 1411–1430.

Quin, H., 1990. Dynamic stress drop and rupture dynamics of the october 15, 1979 imperial valley, california, earthquake, *Tectonophysics*, **175**(1-3), 93–117.

Reid, H. F., 1910. *Volume II of The California earthquake of April 18, 1906: Report of the State Earthquake Investigation Commission*, Chap.: The mechanics of earthquake, pp. 181–207, Carnegie Institution of Washington publication: no. 87, Carnegie Institution of Washington, Washigton D. C.

Ruiz, J. A., Baumont, D., Bernard, P., & Berge-Thierry, C., 2007. New approach in the kinematic k^{-2} source model for generating physical slip velocity functions, *Geophys. J. Int.*, **171**(2), 739–754.

Ruiz, S. & Madariaga, R., 2011. Determination of the friction law parameters of the M_w 6.7 Michilla earthquake in northern Chile by dynamic inversion, *Geophys. Res. Lett.*, **38**(9), L09317.

Ruiz, S. & Madariaga, R., 2013. Kinematic and dynamic inversion of the 2008 northern Iwate earthquake, *Bull. Seism. Soc. Am.*, **103**(2A), 694–708.

Rundle, J. B., Holliday, J. R., Yoder, M., Sachs, M. K., Donnellan, A., Turcotte, D. L., adn W. Klein, K. F. T., & Kellogg, L. H., 2011. Earthquake precursors: activation or quiescence?, *Geophys. J. Int.*, **187**(1), 225–236.

Sambridge, M., 1999a. Geophysical inversion with a neighbourhood algorithm - I. Searching a parameter space, *Geophys. J. Int.*, **138**(2), 479–494.

Sambridge, M., 1999b. Geophysical inversion with a neighbourhood algorithm - II. Appraising the ensemble, *Geophys. J. Int.*, **138**(2), 727–746.

Saraò, A., Das, S., & Suhadolc, P., 1998. Effect of non-uniform station coverage in the inversion for earthquake rupture history for a Haskell-type source model, *Journal of Seismology*, **2**(1), 1–25.

Schöffel, H. J. & Das, S., 1999. Fine details of the Wadati-Benioff zone under Indonesia and its geodynamic implications, *J. Geophys. Res.*, **104**(B6), 13101–13114.

Shakal, A., Haddadi, H., Graizer, V., Lin, K., & Huang, M., 2006. Some key features of the strong-motion data from the M6.0 Parkfield, California, earthquake of 28 September 2004, *Bull. Seism. Soc. Am.*, **96**(4B), S90–S118.

Shelly, D. R., 2009. Possible deep fault slip preceding the 2004 parkfield earthquake, inferred from detailed observations of tectonic tremor, *Geophys. Res. Lett.*, **36**(36), L17318.

Shiba, Y. & Irikura, K., 2005. Rupture process by waveform inversion using simulated annealing and simulation of broadband ground motions, *Earth Planets Space*, **57**(7), 571–590.

Sibson, R., Ghisetti, F., & Ritsau, J., 2011. Stress control of an evolving strike-slip fault system during the 2010-2011 Canterbury, New Zealand, earthquake sequence, *Seismol. Res. Lett.*, **82**(6), 824–832.

Sieh, K. E., 1981. *Earthquake Prediction: An International Review*, Chap.: A review of geological evidence for recurence times of large earthquakes, pp. 181–207, Maurice Ewing series 4, American Geophysical Union, Washington, D. C.

Smith, B. R. & Sandwell, D. T., 2006. A model of the earthquake cycle along the San Andreas fault system for the past 1000 years, *J. Geophys. Res.*, **111**(B1), B01405.

Smith, S. W. & Van De Lindt, W., 1969. Strain adjustments associated with earthquakes in southern California, *Bull. Seism. Soc. Am.*, **59**(4), 1569–1589.

Spudich, P. & Miller, D. P., 1990. Seismic site effects and the spatial interpolation of earthquake seismograms: Results using aftershocks of the 1986 North Palm Springs, California, earthquake, *Bull. Seism. Soc. Am.*, **80**(6A), 1504–1532.

Stein, R. S., 1999. The role of stress transfer in earthquake occurence, *Nature*, **402**, 605–609.

Stramondo, S., Kyriakopoulos, C., Bignami, C., Chini, M., Melini, D., Moro, M., Picchiani, M., Saroli, M., & Boschi, E., 2011. Did the September 2010 (Darfield) earthquake trigger the February 2011 (Christchurch) event?, *Sci. Rep.*, **1**, 1–7.

Sykes, L. R., 1971. Aftershock zones of great earthquakes, seismicity gaps, and earthquake prediction for Alaska and the Aleutians, *J. Geophys. Res.*, **76**(32), 8021–8041.

Thurber, C., Roecker, S., Roberts, K., Gold, M., Powell, L., & Rittger, K., 2003. Earthquake locations and three-dimensional fault zone structure along the creeping section of the San Andreas Fault near Parkfield, CA: Preparing for SAFOD, *Geophys. Res. Lett.*, **30**(3), 1112.

Thurber, C., Zhang, H., Waldhauser, F., Hardebeck, J., Michael, A., & Eberhart-Phillips, D., 2006. Three-dimensional compressional wavespeed model, earthquake relocations, and focal mechnisms for the Parkfield, California, region, *Bull. Seism. Soc. Am.*, **96**(4B), S38–S49.

Toda, S., Stein, R. S., Beroza, G. C., & Marsan, D., 2012. Aftershocks halted by static stress shadows, *Nat. Geosci.*, **5**, 410–413.

Toké, N. A. & Arrowsmith, J. R., 2006. Reassessment of a slip budget along the Parkfield segment of the San Andreas Fault, *Bull. Seism. Soc. Am.*, **96**(4B), S339–S348.

Toppozada, T. R., Branum, D. M., Reichle, M. S., & Hallstrom, C. L., 2002. San Andreas fault zone, California: M≥5.5 earthquake history, *Bull. Seism. Soc. Am.*, **92**(7), 2555–2601.

Trifunac, M. D., 1974. A three-dimensional dislocation model for the San Fernando, California, Earthquake of February 9, 1971, *Bull. Seism. Soc. Am.*, **64**(1), 149–172.

Twardzik, C., Madariaga, R., Das, S., & Custodio, S., 2012. Robust features of the source process for the 2004 Parkfield, California, earthquake from strong-motion seismograms., *Geophys. J. Int.*, **191**(3), 1245–1254.

Vallée, M. & Bouchon, M., 2004. Imaging coseismic rupture in far field by slip patches, *Geophys. J. Int.*, **156**(3), 615–630.

Voronoi, M. G., 1908. Nouvelles applications des paramètres continus à la thèorie des formes quadratiques, *J. reine Angew. Math.*, **134**, 198–287.

Waldhauser, F., Ellsworth, W. L., Shaff, D. P., & Cole, A., 2004. Streaks, multiplets, and holes: High-resolution spatio-temporal behavior of Parkfield seismicity, *Geophys. Res. Lett.*, **31**(18), L18608.

Wellman, H. W., 1955. New Zealand Quaternary Tectonics, *Geol. Rundsch.*, **43**(1), 248–257.

Wyss, M., Shimazaki, K., & Urabe, T., 1996. Quantitative mapping of a precursory seismic quiescence to the Izu-Oshima 1990 (M6.5) earthquake, Japan, *Geophys. J. Int.*, **127**(3), 735–743.

Yamashina, K., 1978. Induced earthquakes in the Izu peninsula by the Izu-Hanto-Oki earthquake of 1974, Japan, *Tectonophysics*, **51**(3-4), 139–154.

Yoshida, S., 1986. A method of waveform inversion for earthquake rupture process, *J. Phys. Earth*, **34**(3), 235–255.

Zhou, S., Irikura, K., & Chen, X., 2004. Analysis of the reliability and resolution of the earthquake source history inferred from the waveforms, taking the Chi-Chi earthquake as an example, *Geophys. J. Int.*, **157**(3), 1217–1232.